

STUDY OF PARABOLIC QUANTUM WELL MICROCAVITIES
AND TERAHERTZ TIME DOMAIN SPECTROSCOPY
IN THE BOSONIC CASCADE REGIME

ALEXANDROS TZIMIS

UNIVERSITY OF CRETE
FACULTY OF SCIENCES AND ENGINEERING
DEPARTMENT OF MATERIALS SCIENCE AND TECHNOLOGY

A DISSERTATION SUBMITTED IN PARTIAL FULFILLMENT OF THE
REQUIREMENTS FOR THE DEGREE OF DOCTOR OF PHILOSOPHY

AUTHOR
ALEXANDROS TZIMIS

ADVISOR
PAVLOS SAVVIDIS

COMMITTEE
PROF. PAVLOS SAVVIDIS, UNIVERSITY OF CRETE
PROF. GEORGE KIOSEOGLU, UNIVERSITY OF CRETE
DR. GEORGE DELIGEORGIS, IESL-FORTH
PROF. NIKOS PELEKANOS, UNIVERSITY OF CRETE
PROF. ZAHARIAS HATZOPOULOS, UNIVERSITY OF CRETE
PROF. DIMITRIS PAPAZOGLU, UNIVERSITY OF CRETE
PROF. VASILIS APOSTOLOPOULOS, UNIVERSITY OF SOUTHAMPTON

dedicated to my parents,
Mariza and Leonidas

"The saddest aspect of life right now is that science gathers knowledge
faster than society gathers wisdom."
- Isaac Asimov

CONTENTS

ACKNOWLEDGEMENTS	1
ABSTRACT	3
ABSTRACT GREEK	5
PUBLICATIONS	7
ACRONYMS	9
INTRODUCTION	11
1 FUNDAMENTALS	13
1.1 Semiconductors and the bandgap	13
1.2 Excitons and quantum confinement	15
1.3 Microcavities and light confinement	18
1.4 Light-Matter interaction and polaritons	21
1.5 Polariton condensation and lasing	25
1.6 Terahertz radiation and bosonic cascade	30
2 A PARABOLIC QUANTUM WELL STUDY	37
2.1 Introduction	37
2.2 Samples	38
2.3 Excitonic levels and terahertz oscillations	40
2.4 Strong coupling and non-linear emission	42
2.5 Conclusion	44
3 ENERGY RELAXATION DYNAMICS	45
3.1 Introduction	45
3.2 Samples	45
3.3 Excitonic levels and indication of a cascade mechanism . .	46
3.4 A comparative study of exciton relaxation	47
3.5 Theoretical modeling	51
3.6 Conclusion	55

4	TOWARDS TERAHERTZ EMISSION AND DETECTION	57
4.1	The basics	57
4.2	Results	64
4.3	Conclusion	75
5	OVERVIEW AND FINAL THOUGHTS	77
A	EXPERIMENTAL TECHNIQUES	81
A.1	Vacuum and cooling system	81
A.2	Continuous-wave and pulsed laser system	82
A.3	Reflectivity	82
A.3.1	Fiber / Free-space reflectivity	83
A.3.2	Brewster angle reflectivity	84
A.4	Luminescence	85
A.4.1	Photoluminescence	85
A.4.2	Photoluminescence, k-space / real-space imaging	86
A.5	Terahertz spectroscopy	87
A.6	Pump-probe spectroscopy for THz oscillations	92
A.7	λ -modulated reflectivity	92
A.8	Double-pump technique for relaxation dynamics	93
B	CODES AND CALCULATIONS	95
B.1	The parabolic potential well	95
B.2	Igor Pro code: Sample structure design	96
B.3	Igor Pro code: Four oscillator model	97
B.4	THz-TDS control program: Step calculation	100
B.5	Igor Pro code: Procedure for FFT function and THz menu	102
B.6	Mathematica code: Loop scans	104
B.7	Mathematica code: 2D plot	105
	BIBLIOGRAPHY	107

ACKNOWLEDGEMENTS

The work for the present thesis was performed in the Nanoscale Optoelectronics Lab, in the Microelectronics Research Group of Institute of Electronic Structure and Laser - Foundation for Research and Technology Hellas, in Heraklion, Crete.

I would like to thank my advisor, Prof. Pavlos Savvidis, for his guidance and support. I appreciate all his contributions of time, ideas, and funding. In addition, I would like to thank Prof. Zaharias Hatzopoulos for the epitaxial growth of the semiconductor samples, Prof. Vasilis Apostolopoulos and Dr. George Deligeorgis for the discussions about the THz setup, and the rest of my thesis committee, Prof. Nikos Pelekanos, Prof. George Kioseoglou, and Prof. Dimitris Papazoglou, for evaluating my research work.

Many people contributed to the present study; I would like to thank: Dr. Gabriel Christmann for his help with the experiments and the writing of a research paper, I greatly appreciate his assistance and his clear way of explaining scientific terms; Dr. Artur Trifonov for the collaboration and cooperation; Dr. Panos Tsotsis for his suggestions; Pramod Kumar Sharma for the endless discussions; Maria Androulidaki for her help in the optics lab; Katerina Tsagkaraki for the SEM images of the samples; Nikos Papadakis and Michalis Sfendourakis for the technical support; all the technicians from the machine workshop who crafted everything we needed for the experiments; our group secretary Marina Tzanakaki for the cooperation and for the discussions about the management issues.

I thank my office mate for more than 5 years, Dr. Simos Tsintzos, for showing me the lab when I joined the group, helping me understand(?) complicated quantum physics, cooking and sharing food with me, and most importantly, for creating an enjoyable work environment. My other office mate, Giannis Paschos, for the countless hours we spent trying to understand the experiments and solve all these problems we had with our data analysis.

I would like to thank all my friends for sharing their time with me all these years. Special thanks to my friend Thanasis Margiolakis, we spent a lot of time together during the last years of the PhD, trying to finish our research work and write the manuscript.

Lastly, I owe my deepest gratitude and love to my parents, Mariza and Leonidas, for their constant love and support throughout my life.

Alexandros Tzimis, Heraklion, December 2018

ABSTRACT

The present dissertation is focused on the study of semiconductor microcavities with embedded quantum wells. The devices are based on the strong coupling between light (photons in a cavity) and matter (excitons in quantum wells), forming new quasiparticles called polaritons. Such structures aim to provide an alternative way of generating THz photons utilizing a bosonic cascade phenomenon. The cascade is based on a series of sequential transitions of bosons from equidistant energy levels and in the process THz photons are emitted. The work presented here is divided into two parts. The first part deals with a study of semiconductor structures based on a single parabolic quantum well. The second part describes the development and evaluation of a THz time domain spectrometer aimed to study bosonic cascade.

In the first part we show that the parabolic quantum well exhibits the expected equally spaced excitonic transitions. We observe quantum beating at THz frequencies between the discrete energy levels of quantum well excitons. When a single parabolic quantum well is placed in a microcavity, the full structure shows a clear anticrossing between heavy hole / light hole excitons and the cavity mode, revealing the strong coupling regime. Furthermore, under non-resonant optical excitation, the microcavity exhibits non-linear stimulated emission. In addition, a relaxation dynamics study shows that excitons relax much faster in the parabolic potential compared to a structure with conventional rectangular quantum wells. The theoretical modeling of relaxation dynamics qualitatively agrees with the experimental results and predicts the time evolution of exciton densities at each level of the parabolic quantum well, along with the photoluminescence contribution of each transition.

The second part deals with the development and evaluation of a THz time domain spectrometer which allows measurements of THz emission as well as optically induced modulation of THz transmission, gain, and absorption. The setup provides the ability of performing such experiments in cryogenic environment at a temperature range of 14-300 K. Preliminary results on absorption/gain measurements on parabolic quantum well microcavities are also presented.

Περίληψη

Η παρούσα εργασία εστιάζεται στη μελέτη ημιαγωγικών μικροκοιλοτήτων με κβαντικά πηγάδια. Οι δομές αυτές στηρίζονται στην ισχυρή σύζευξη μεταξύ φωτός (φωτόνια στη μικροκοιλότητα) και ύλης (εξιτόνια στα κβαντικά πηγάδια), δημιουργώντας νέα ψευδοσωματίδια που ονομάζονται πολαριτόνια. Τέτοιες δομές μπορούν να προσφέρουν έναν εναλλακτικό τρόπο εκπομπής THz ακτινοβολίας, χρησιμοποιώντας το φαινόμενο των μποζονικών αλυσιδωτών μεταβάσεων από ισαπέχουσες ενεργειακές καταστάσεις. Η εργασία χωρίζεται σε δύο μέρη. Το πρώτο μέρος ασχολείται με τη μελέτη ημιαγωγικών δομών βασισμένων σε κβαντικά πηγάδια με παραβολικό δυναμικό. Το δεύτερο μέρος περιγράφει την ανάπτυξη και τη δοκιμή ενός THz φασματομέτρου για τη μελέτη των μποζονικών αλυσιδωτών μεταβάσεων.

Στο πρώτο μέρος δείχνουμε ότι το παραβολικό κβαντικό πηγάδι εμφανίζει τα αναμενόμενα ισαπέχοντα ενεργειακά επίπεδα. Παρατηρούμε κβαντικές ταλαντώσεις (*quantum beating*) σε συχνότητες THz μεταξύ των ενεργειακών επιπέδων των εξιτονίων του κβαντικού πηγადιού. Όταν το παραβολικό κβαντικό πηγάδι εμπεριέχεται σε μικροκοιλότητα, η δομή δείχνει τη χαρακτηριστική συμπεριφορά απουσίας τομής (*anticrossing*) μεταξύ εξιτονίων βαριών/ελαφριών οπών και του φωτονικού ρυθμού, αποδεικνύοντας έτσι το καθιεστώσ ισχυρής σύζευξης. Επιπλέον, υπό μη συντονισμένη οπτική διέγερση, η μικροκοιλότητα εμφανίζει μη-γραμμική εξαναγκασμένη εκπομπή. Στη συνέχεια, η μελέτη δυναμικής έδειξε ότι τα εξιτόνια αποδιεγείρονται πιο γρήγορα στο παραβολικό δυναμικό συγκριτικά με μία δομή με κβαντικά πηγάδια τετραγωνικού δυναμικού. Η θεωρητική ανάλυση της δυναμικής αποδιεγέρσεων συμφωνεί ποιοτικά με τα πειραματικά αποτελέσματα και περιγράφει τη χρονική εξέλιξη των εξιτονικών πληθυσμών σε κάθε επίπεδο του παραβολικού κβαντικού πηγადιού μαζί με τη συνεισφορά κάθε μετάβασης στη συνολική φωτοφωταύγεια.

Στο δεύτερο μέρος περιγράφουμε την ανάπτυξη και τη δοκιμή ενός THz φασματομέτρου το οποίο επιτρέπει τη μέτρηση THz εκπομπής καθώς και την αλλαγή που προκαλεί εξωτερική οπτική διέγερση, στη διαδιδόμενη στο δείγμα THz ακτινοβολία. Η διάταξη προσφέρει τη δυνατότητα μετρήσεων σε θερμοκρασίες από 14 έως 300 K. Παρουσιάζονται επίσης τα πρώτα αποτελέσματα απορρόφησης/ενίσχυσης σε ημιαγωγική δομή μικροκοιλότητας με παραβολικά κβαντικά πηγάδια.

PUBLICATIONS

The following articles were published during the period of the present thesis and contain parts of the manuscript.

Strong coupling and stimulated emission in single parabolic quantum well microcavity for terahertz cascade

A. Tzimis, A. V. Trifonov, G. Christmann, S. I. Tsintzos, Z. Hatzopoulos, I. V. Ignatiev, A. V. Kavokin, and P. G. Savvidis
Applied Physics Letters 107, 101101 (2015)

Dynamics of the energy relaxation in a parabolic quantum well laser

A. V. Trifonov, E. D. Cherotchenko, J. L. Carthy, I. V. Ignatiev, A. Tzimis, S. Tsintzos, Z. Hatzopoulos, P. G. Savvidis, and A. V. Kavokin
Physical Review B 93, 125304 (2016)

Inverse-phase Rabi oscillations in semiconductor microcavities

A. V. Trifonov, N. E. Kopteva, M. V. Durnev, I. Ya. Gerlovin, R. V. Cherbunin, A. Tzimis, S. I. Tsintzos, Z. Hatzopoulos, P. G. Savvidis, and A. V. Kavokin
Physical Review B 95, 155304 (2017)

Electrical Tuning of non-linearities in Exciton-Polariton Condensates

S. I. Tsintzos, A. Tzimis, G. Stavriniadis, A. Trifonov, Z. Hatzopoulos, J. J. Baumberg, H. Ohadi, and P. G. Savvidis
Physical Review Letters 121, 037401 (2018)

Hidden polarization of unpolarized light

G. G. Kozlov, I. I. Ryzhov, A. Tzimis, Z. Hatzopoulos, P. G. Savvidis, A. V. Kavokin, M. Bayer, and V. S. Zapasskii
Physical Review A 98, 043810 (2018)

ACRONYMS

QCL	quantum cascade laser
BCL	bosonic cascade laser
SEM	scanning electron microscope
GaAs	Gallium Arsenide
LT-GaAs	low temperature grown Gallium Arsenide
AlAs	Aluminum Arsenide
AlGaAs	Aluminum Gallium Arsenide
InGaAs	Indium Gallium Arsenide
GaN	Gallium Nitride
Si HR	high resistivity Silicon
SI GaAs	semi-insulating Gallium Arsenide
CW	continuous-wave
MC	microcavity
QW	quantum well
PQW	parabolic quantum well
DBR	distributed Bragg reflector
LP	lower polariton
MP	middle polariton
UP	upper polariton
SCR	strong coupling regime
THz-TDS	terahertz time domain spectroscopy
OPTP	optical pump THz probe
PL	photoluminescence
IR	infrared
hh	heavy hole
lh	light hole
BEC	Bose-Einstein condensation
LED	light emitting diode
CCD	charged coupled device

INTRODUCTION

We explore a recently proposed alternative way of emitting or amplifying THz photons, using a system based on a microcavity structure with an embedded quantum well with parabolic potential. The parabolic quantum well is responsible for the creation of equally spaced energy levels and of almost-equally spaced excitonic levels¹, which act as a ladder for cascade relaxation. In such structures, a macroscopically occupied ground state enhances the transitions to the ground state and improves the emission. The generation process is similar to the well-known quantum cascade laser which is able to emit multiple THz photons for each injected electron, without the need of population inversion for every transition. The proposed device has the advantage of a simpler structure, without a superlattice, and employs a bosonic cascade regime which is based on sequential transitions of bosons (such as excitons) instead of electrons.

The present thesis is focused on the study of semiconductor microcavities with embedded parabolic quantum wells. We begin by exploring the simplest case of a bare parabolic quantum well and we continue with a study of a microcavity structure with a parabolic quantum well in it. In addition, we present our results on the non-trivial relaxation dynamics of the system and we compare the relaxation of carriers on the parabolic quantum well structure with the relaxation on a conventional one with rectangular quantum wells.

The ultimate aim is to measure THz emission from these specially designed structures. We develop and evaluate a THz spectrometer based on photoconductive antennas for both generation and detection of THz pulses. Due to the spurious emission from the semiconductor samples under external optical pumping, we separate and isolate the different emission sources by employing double lock-in detection. This optical-pump THz-probe technique cuts out the optically generated emission and measures only the optically induced modulation of the THz transmission.

¹The energy states (electron, hole) are equally spaced, the excitonic states are not exactly equally spaced due to their binding energy.

The manuscript is divided into 5 chapters and 2 appendices. Chapter 1 presents an overview of the fundamental background. In Chapter 2, our first study of the parabolic quantum well structures is presented and we continue, in Chapter 3, by studying the energy relaxation dynamics in such structures. Chapter 4 describes the experimental regimes of the THz time domain spectroscopy setup and our first evaluation with different samples, including a microcavity structure. Chapter 5 is a synopsis accompanied by some technical recommendations. Appendix A presents all the experimental techniques, setups, and instruments and Appendix B contains calculations, automation programs, and programming codes.

Chapter 1

FUNDAMENTALS

This chapter introduces a brief overview of the theoretical background and the related fundamental concepts. It starts with an introduction to semiconductors, the type of materials that we use for our samples. Then, the two basic ingredients for light-matter interaction are described. Matter is represented by excitons, so, first, excitons and their confinement are discussed. Light is represented by photons and their confinement is achieved by a special type of structure, the microcavity (MC). After the description of both of them, the basics for their interaction and the concept of polaritons are presented. Then, the phenomenon of polariton condensation and its natural consequence, the polariton lasing, are described. Lastly, THz radiation and the concept of the bosonic cascade laser (BCL) are explained.

1.1 Semiconductors and the bandgap

Solids are divided into three categories on the basis of their electrical conductivity, namely insulators, conductors, and semiconductors. The electrical conductivity is related to the so-called bandgap, an energy range where states cannot exist. The energy band below the bandgap is called the valence band, while the one above the bandgap is called the conduction band. Photons with energy greater than the bandgap, can excite electrons from the valence band to the conduction band. When electrons are in there, they have enough energy to move in the material and create electric current, while when they fall back to the valence band, they can emit light.

Insulators have a large bandgap, therefore, a large amount of energy is required to move the electrons to the conduction band. In conductors, the valence and the conduction bands overlap, thus, they don't have a bandgap. Electrons can effortlessly move between the two bands making the material highly conductive. Semiconductors have an electrical con-

ductivity between insulators and conductors and that property is what makes them useful.

A semiconductor can be roughly defined as a material with a bandgap greater than 0 and less than 4 eV. There are, of course, exceptions to this definition. For example, there are terms such as semi-conducting diamond with a 6 eV bandgap and semi-insulating Gallium Arsenide (SI GaAs) with a 1.5 eV bandgap. There are many different types of semiconductors, e.g., elemental (such as Si), organic (such as Polyacetylene), binary (such as Gallium Arsenide (GaAs)), etc. For a detailed analysis see [1]. Here, we mostly use binary and ternary semiconductors like GaAs, Aluminum Arsenide (AlAs), and Aluminum Gallium Arsenide (AlGaAs).

The bandgap energy is temperature dependent and it decreases as the temperature increases. The following relation (1.1) was suggested by Y. P. Varshni [2] in 1967

$$E_{bg}(T) = E_{bg}(0) - \frac{\alpha T^2}{T + \beta}, \quad (1.1)$$

where $E_{bg}(0)$ is the bandgap energy value at 0 K, α and β are constants which are adjusted depending on the sample and are determined by fitting experimental data, and T is the temperature. A theoretical calculation of GaAs bandgap energy versus temperature using the Varshni equation, with $E_{bg}(0) = 1.519$ eV, $\alpha = 5.405 \cdot 10^{-4}$ eV/K, $\beta = 204$ K, is shown in Figure 1.1. As can be seen, the bandgap energy drops ~ 100 meV, from the lowest temperature to room temperature.

Lastly, the bandgap is divided into two main types, the direct and the indirect. A semiconductor has a direct bandgap when the maximum of the valence band and the minimum of the conduction band have the same momentum (k-vector). Otherwise, the semiconductor has an indirect bandgap. This difference is important for the optical devices. In both the production of an electron-hole pair and the recombination, a direct bandgap semiconductor is better. It's easier for a photon to produce an electron-hole pair in a direct bandgap semiconductor and it's also more efficient for the pair to recombine and emit light. In an indirect bandgap, the momentum is different, so, the processes should be mediated by something else, which in this case is a lattice vibration (phonon), in order for the electron to either gain or lose momentum.

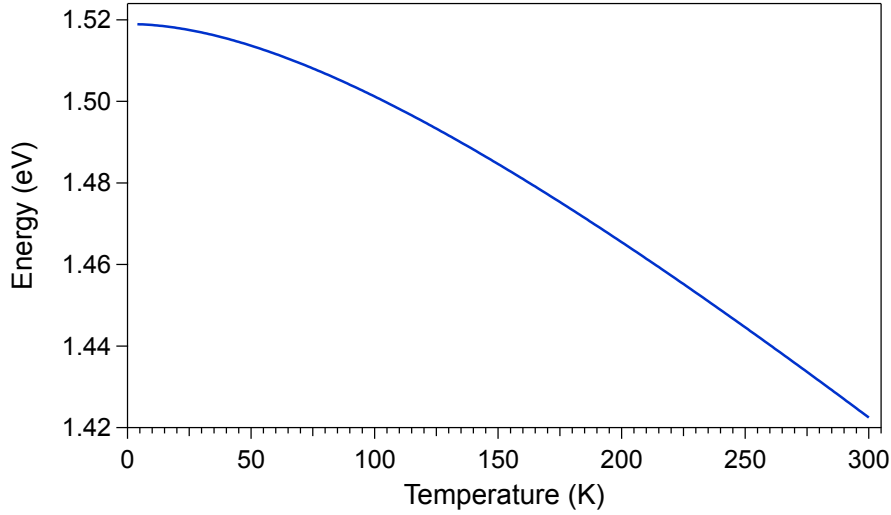


Figure 1.1: Theoretical calculation of GaAs bandgap energy versus temperature using the Varshni equation.

1.2 Excitons and quantum confinement

Experimental optical studies in semiconductors have revealed absorption peaks in energies inside the bandgap, near the conduction band. These peaks correspond to electron-hole pairs bound by the electrostatic Coulomb force, which are called excitons. The concept of excitons can be described by various methods [1, 3], but the simpler is by using the effective mass approximation. Within this approximation, the electron and the hole are considered as two particles moving with the effective masses of the conduction and valence bands, respectively. This approximation also suggests that the Coulomb interaction between electron and hole leads to a Hydrogen-like situation with a Coulomb potential term

$$V_C(r) = \frac{-e^2}{4\pi\epsilon_0\epsilon|r_e - r_h|}, \quad (1.2)$$

where e is the electron charge, ϵ_0 is the vacuum permittivity, ϵ is the medium permittivity, and $|r_e - r_h|$ is the distance between the electron-hole pair. For simple parabolic bands and a direct bandgap semiconductor, the relative motion of electron and hole can be separated from the motion of the center of mass. The dispersion relation of excitons is

$$E_{exc}(n_B, K) = E_{bg} - Ry^* \frac{1}{n_B^2} + \frac{\hbar K^2}{2M}, \quad (1.3)$$

where E_{bg} is the bandgap energy,
 Ry^* is the effective Rydberg energy

$$Ry^* = 13.6 \frac{\mu}{m_0} \frac{1}{\epsilon^2}, \quad (1.4)$$

where μ is the reduced exciton mass

$$\mu = \frac{m_e m_h}{m_e + m_h}, \quad (1.5)$$

where m_e , m_h are the electron and hole masses,
 m_0 is the free electron mass,
 ϵ is the medium permittivity,
 n_B is the principal quantum number

$$n_B = 1, 2, 3, \dots, \quad (1.6)$$

\hbar is the reduced Planck constant,
 K is the exciton wave-vector

$$K = k_e + k_h, \quad (1.7)$$

where k_e , k_h are the electron and hole wave-vectors,
 M is the translational mass

$$M = m_e + m_h, \quad (1.8)$$

where m_e , m_h are the electron and hole masses.

There are two types of excitons, Frenkel excitons [4], named after the Soviet physicist Jacov Frenkel, and Wannier-Mott excitons [5], named after the Swiss physicist Gregory Wannier and the British physicist Nevill Francis Mott. Frenkel excitons are found in materials with small dielectric constants (like organic materials), where the Coulomb interaction is strong, thus, the excitons are small. Their typical binding energy is ~ 1 eV and their typical radius is ~ 1 nm. Wannier-Mott excitons are found in materials with large dielectric constants (like inorganic semiconductors), the Coulomb interaction is weak, thus, the excitons are large. Their typical binding energy is ~ 10 meV and their typical radius is ~ 10 nm. Note that, Coulomb force depends on the dielectric constant of the medium and is inversely proportional to it. The dielectric constant is also known as relative permittivity, is dimensionless, and it is given by the equation $\kappa = \epsilon_r = \epsilon/\epsilon_0$.

In the present thesis, inorganic semiconductors were used, therefore, the term exciton is referred to the Wannier-Mott type. The binding energy of the excitons is an important factor for their temperature stability. Wannier-Mott excitons have small binding energy, thus, low temperature helps exciton to survive. The value for the exciton binding energy in GaAs for example, is 4.2 meV [6], while room temperature energy is $kT = 25.7$ meV. Therefore, excitons dissociate at high temperature. Lastly, it should be noted that the photon energy required for absorption is lowered by the exciton binding energy.

When one or more dimensions of a material are reduced, its electrical and optical properties are affected. The result is a low-dimensional structure, typically ~ 1 -1000 nm. To be more precise, when the dimension approaches a critical quantum term called exciton Bohr radius, the effect of quantum confinement takes place. Quantum confinement changes the properties of a material and both the bandgap and the ground state energy are increased.

For a free particle with effective mass m^* , confined in an infinite potential energy in the z direction, the allowed wave-vectors k_z are given by the relation $k_{zn} = 2\pi/\lambda_n = n\pi/L$, $n = 1, 2, 3, \dots$. Its ground state energy is increased by the amount ΔE relative to the unconfined case

$$\Delta E = \frac{\hbar^2 k_z^2}{2m^*} = \frac{\hbar^2 \pi^2}{2m^* L^2}. \quad (1.9)$$

The energy ΔE is called the confinement energy of the particle and it is a consequence of Heisenberg's uncertainty principle. In addition to the ground state energy increase, quantum confinement also causes the particle's excited state energies to become quantized.

There are three main kinds of quantum confined low-dimensional structures, depending on the number of degrees of freedom in the particle momentum (or on the number of dimensions with confinement). Confinement of excitons is possible along 1, 2, or 3 dimensions, creating quantum wells, quantum wires, and quantum dots respectively. As can be seen from Table 1.1, in the 3-Dimensional structure (bulk) there is no quantum confinement and the particle is free to move. In the 2-Dimensional structure (the quantum well) the quantization occurs in one dimension, while the particle is free to move in the other two dimensions. In the 1-Dimensional structure (the quantum wire), the quantization occurs in two dimensions, while the particle is free to move in one dimension. Finally, in

the 0-Dimensional structure (the quantum dot) the quantization occurs in all three dimensions.

Structure	Quantum confinement	Free dimensions
Bulk	0	3
Quantum well	1	2
Quantum wire	2	1
Quantum dot	3	0

Table 1.1: Categories of low-dimensional structures.

In the present thesis, quantum wells (QWs) are used for the exciton confinement. Practically, a QW is realized with a thin semiconductor layer embedded between two semiconductor layers of wider bandgap (e.g. GaAs QW embedded in two AlGaAs layers). These thin nanostructures can be fabricated using crystal growth methods with precise and controlled stacking of semiconductor layers, such as molecular beam epitaxy (used here) and metalorganic chemical vapour deposition.

1.3 Microcavities and light confinement

A MC is a structure that traps light. It is an optical resonator, comparable to the dimension of the wavelength of light and it is used to confine photons [7]. A MC is similar to a planar Fabry-Perot cavity with two opposing flat mirrors which are formed from distributed Bragg reflectors (DBRs). A DBR consists of alternate layers of semiconductor materials of low and high refractive index, specially designed for a specific wavelength λ_0 . The combination of two layers, one with low refractive index and the next one with high refractive index, is called a pair. The thickness of each layer is given by

$$l_{DBR_x} = \frac{\lambda_0/n_x}{4}, \quad (1.10)$$

where λ_0 is the desired wavelength and n_x is the refractive index of each material of the pair. This periodic structure creates a mirror-like response with a broadband high-reflectivity region centered at λ_0 , called the stop-band (Figure 1.2 left), with oscillating side-lobes on either side [8].

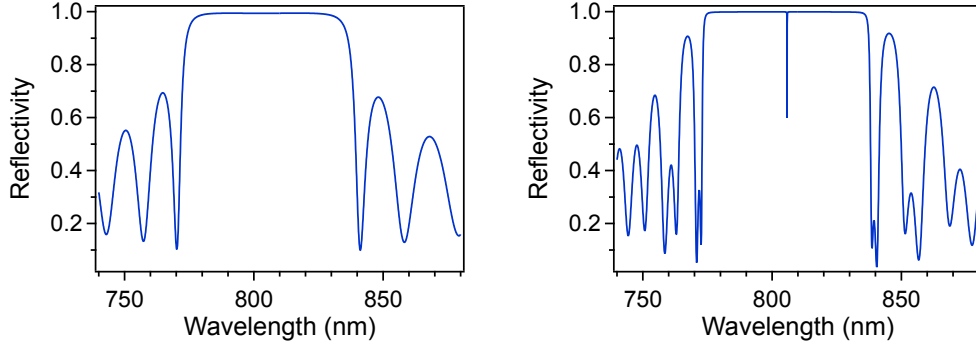


Figure 1.2: Reflectivity simulation of a DBR (left) and a MC (right).

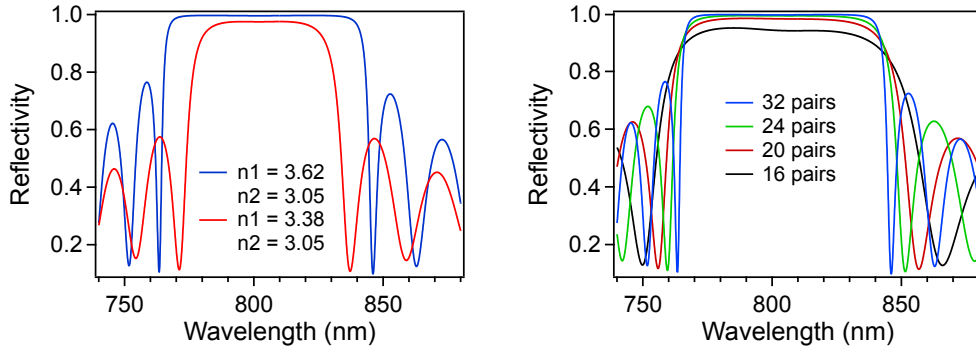


Figure 1.3: Reflectivity simulation of a DBR showing the effect of the refractive index contrast (left) and the number of pairs (right).

Light waves that propagate in the transmission direction interfere destructively, while light waves that propagate in the reflection direction interfere constructively. The reflectivity without losses is given by

$$R = 1 - 4 \frac{n_{ext}}{n_c} \left(\frac{n_{low}}{n_{high}} \right)^{2N}, \quad (1.11)$$

where n_{ext} , n_c , n_{low} , n_{high} are the refractive indices of the external medium, the cavity material, the low and high refractive index layers of the pair, and N is the number of pairs. Thus, to achieve high reflectivity, materials with high refractive index contrast, and a high number of pairs should be used (see Figure 1.3 for an example). The cavity exists between two DBRs and its thickness determines the so-called cavity mode. The cavity mode is the one wavelength that will be formed as standing wave inside the cavity (Figure 1.2 right). According to the Bragg condition, the thickness of the cavity should be an integer multiple of $\lambda_0/2$ in the cavity medium, and

is calculated by

$$l_c = m \frac{\lambda_0/n_c}{2}, \quad m = 1, 2, 3... \quad (1.12)$$

where λ_0 is the desired wavelength and n_c is the refractive index of the cavity material. The short cavity length leads to photon quantization in the growth direction and provides no confinement perpendicular to the growth axis, thus, the photon has an in-plane dispersion. DBRs force the wave-vector k_z in the medium to be $2\pi/L_c$, therefore, the cavity photon energy is

$$E = \frac{\hbar c}{n_c} k = \frac{\hbar c}{n_c} \left[\left(\frac{2\pi}{L_c} \right)^2 + k_{\parallel}^2 \right]^{1/2}, \quad (1.13)$$

and the dispersion is parabolic near $k_{\parallel} = 0$. This relation works well in simple empty cavities but for more complicated structures the transfer matrix theory should be used. The transfer matrix method includes losses and it is used to calculate the optical properties of the structure, such as reflectivity (shown in Figure 1.3), transmission, and absorption, together with the electric field inside the cavity [8]. A schematic diagram of a typical MC and a scanning electron microscope (SEM) image of a real structure, are shown in Figure 1.4.

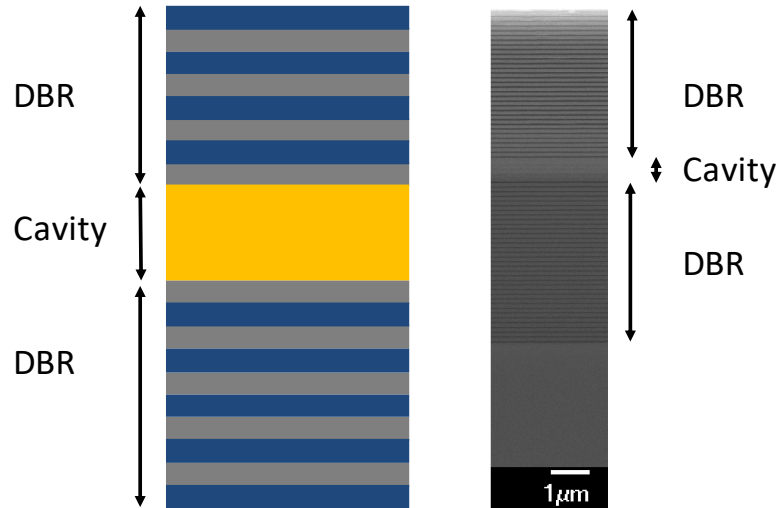


Figure 1.4: Schematic of a MC structure, showing the two DBRs and the cavity between them (left), SEM image of a MC structure (right).

1.4 Light-Matter interaction and polaritons

To take advantage of both photon confinement (light) and exciton confinement (matter), one or more QWs are placed inside the cavity and the cavity mode is designed to be near the excitonic transition in the QW. In semiconductor MCs, depending on the conditions, light-matter interaction is divided into two regimes, the weak and the strong coupling regime (SCR) [9].

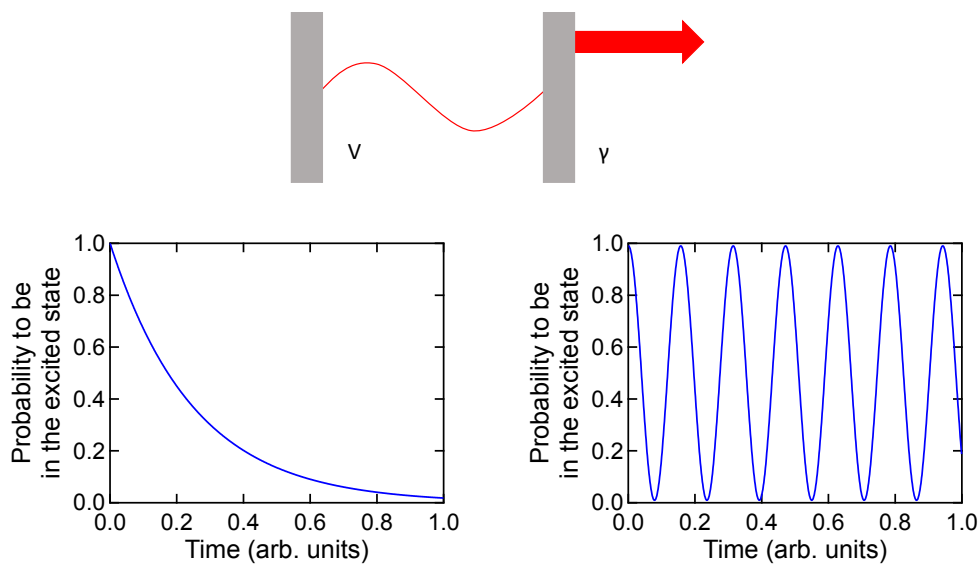


Figure 1.5: Weak (left) and strong (right) coupling regime. Coupling strength V is related to the probability for a photon to interact with the medium. Losses γ are related to the quality of the mirrors, and the exciton and photon decay rates (or lifetimes). When $V \ll \gamma$ the probability for the medium to be in an excited state decays with time (left). When $V \gg \gamma$ the photon stays enough time to interact with the medium, becomes exciton, this exciton emits a photon and so on (right).

Figure 1.5 shows a representation of the two regimes. When the coupling strength V is much smaller than the losses γ ($V \ll \gamma$), the photon leaks the cavity after some reflections (weak coupling), while when $V \gg \gamma$ the photon interacts and re-excites the medium (strong coupling). Therefore, in the weak coupling regime, the probability for the medium to be in an excited state decays with time (Figure 1.5 left). On the contrary, in the strong coupling regime, the probability oscillates with time (Figure 1.5 right). The state constantly oscillates back and forth between the

cavity photon and the exciton, the distinction between light and matter is lost, and new modes called exciton-polaritons (polaritons from now on) are produced, having both a photonic and an excitonic part. In reflectivity, the cavity mode is replaced by two polariton modes, as shown in the simulation of Figure 1.6. Note that one mode means that there is no strong coupling but two modes doesn't necessarily mean the existence of strong coupling. The characteristic feature of strong coupling is the anticrossing behaviour which is described at the end of the present section.

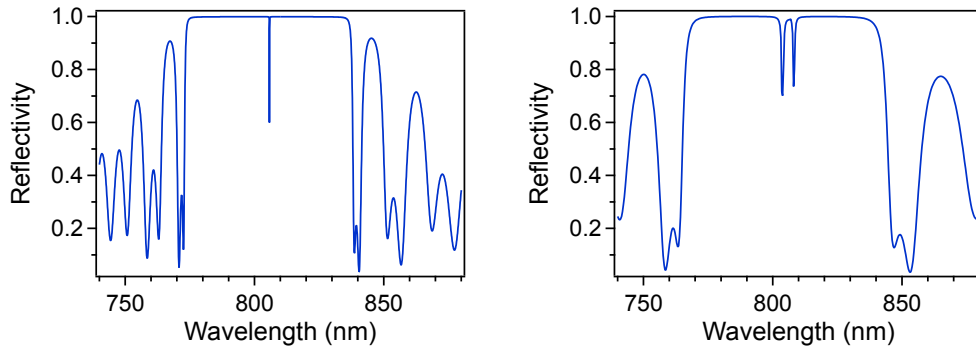


Figure 1.6: Reflectivity simulation of a MC structure in weak (left) and strong (right) coupling regime. The single dip in the weak coupling is the cavity mode which coincides with the excitonic transition at $k=0$. The two dips in the strong coupling correspond to the upper and lower polariton energies. More information can be found at the end of the present section where the dispersion curves are presented.

A polariton is a quasiparticle, which means that behaves like a particle. It is the result of the strong coupling of photons with an excitonic transition. It has mass but it is better described in momentum space. It is short-lived with a typical lifetime of a few picoseconds. If it decays radiatively, emission of photons occurs which carries energy and phase information. It is a boson, which means that many of them can occupy the same quantum state.

The mathematical description of polaritons starts with the Hamiltonian of the system. Here, the basic steps are presented, for a detailed analysis see [7], [10], and [11]. The Hamiltonian [10] of the exciton-photon system is

$$H_P = H_C + H_X + H_I, \quad (1.14)$$

where P is polariton, C is cavity photon, X is exciton, and I is the interaction between the photon and the exciton,

$$H_P = \sum_{k_{\parallel}} E_C(k_{\parallel}) \hat{a}_{k_{\parallel}}^{\dagger} \hat{a}_{k_{\parallel}} + \sum_{k_{\parallel}} E_X(k_{\parallel}) \hat{b}_{k_{\parallel}}^{\dagger} \hat{b}_{k_{\parallel}} + \sum_{k_{\parallel}} \hbar V \hat{a}_{k_{\parallel}}^{\dagger} \hat{b}_{k_{\parallel}} + \hat{a}_{k_{\parallel}} \hat{b}_{k_{\parallel}}^{\dagger}, \quad (1.15)$$

where $E_C(k_{\parallel})$ is the cavity photon energy, $\hat{a}_{k_{\parallel}}^{\dagger}$, $\hat{a}_{k_{\parallel}}$ are the photon creation and annihilation operators, $E_X(k_{\parallel})$ is the excitonic transition energy, $\hat{b}_{k_{\parallel}}^{\dagger}$, $\hat{b}_{k_{\parallel}}$ are the exciton creation and annihilation operators, and V is the coupling strength between the cavity photon and the exciton. The following transformation [10] is used to diagonalise the Hamiltonian

$$\hat{p}_{k_{\parallel}} = X_{k_{\parallel}} \hat{b}_{k_{\parallel}} + C_{k_{\parallel}} \hat{a}_{k_{\parallel}}, \quad (1.16)$$

$$\hat{q}_{k_{\parallel}} = -C_{k_{\parallel}} \hat{b}_{k_{\parallel}} + X_{k_{\parallel}} \hat{a}_{k_{\parallel}}, \quad (1.17)$$

where $X_{k_{\parallel}}$ and $C_{k_{\parallel}}$ are the Hopfield coefficients [11]. The Hamiltonian now is

$$H_P = \sum_{k_{\parallel}} E_{LP}(k_{\parallel}) \hat{p}_{k_{\parallel}}^{\dagger} \hat{p}_{k_{\parallel}} + \sum_{k_{\parallel}} E_{UP}(k_{\parallel}) \hat{q}_{k_{\parallel}}^{\dagger} \hat{q}_{k_{\parallel}} \quad (1.18)$$

where $\hat{p}_{k_{\parallel}}^{\dagger}$, $\hat{p}_{k_{\parallel}}$, $\hat{q}_{k_{\parallel}}^{\dagger}$, $\hat{q}_{k_{\parallel}}$ are the eigen-modes of the system, and LP, UP correspond to the lower and upper polariton branches.

Hopfield coefficients give the photonic and excitonic part of the branch and should satisfy the equation

$$|X_{k_{\parallel}}|^2 + |C_{k_{\parallel}}|^2 = 1. \quad (1.19)$$

For example, when $|X_{k_{\parallel}}|^2 = |C_{k_{\parallel}}|^2 = \frac{1}{2}$, the polariton branches are half photon and half exciton.

The detuning δ is defined as the energy difference between the cavity photon and the exciton at $k_{\parallel} = 0$,

$$\delta = E_C - E_X, \quad (1.20)$$

and $X_{k_{\parallel}}$, $C_{k_{\parallel}}$ are

$$|X_{k_{\parallel}}|^2 = \frac{1}{2} \left(1 + \frac{\delta}{\sqrt{\delta^2 + 4\hbar^2 V^2}} \right), \quad (1.21)$$

$$|C_{k_{\parallel}}|^2 = \frac{1}{2} \left(1 - \frac{\delta}{\sqrt{\delta^2 + 4\hbar^2 V^2}} \right). \quad (1.22)$$

By diagonalising the Hamiltonian (1.18), the eigen-energies [10] can be calculated

$$E_{LP,UP}(k_{\parallel}) = \frac{1}{2} \left(E_C(k_{\parallel}) + E_X(k_{\parallel}) \pm \sqrt{\delta^2 + 4\hbar^2 V^2} \right). \quad (1.23)$$

Equation 1.23 gives the polariton energy-momentum dispersion curves, the lower polariton (LP) and upper polariton (UP) branches.

When the dispersion curve is measured, in weak coupling, photons from the cavity mode and the excitonic transition are observed, as shown in Figure 1.7 (a). In strong coupling, instead of observing the cavity mode and the excitonic transition, two new branches appear. At zero detuning δ , the two polariton branches have the minimum energy separation, which is equal to $2\hbar V$ and it is called the vacuum Rabi splitting. The main characteristic of strong coupling is the anticrossing of the two branches. In Figure 1.7 (b), (c), and (d), the LP and UP branches are shown, in different detuning values δ . Detuning δ can be zero (b), negative (c), or positive (d). Experimentally, the polariton branches can be measured with optical measurements like photoluminescence (PL). Note that there is one more term for polariton branches, the middle polariton (MP) branch, which appears when two or more excitons are present. Two excitons create one MP branch and three excitons create two MP branches. The code for the calculation of the dispersion curves is shown in Appendix B.3.

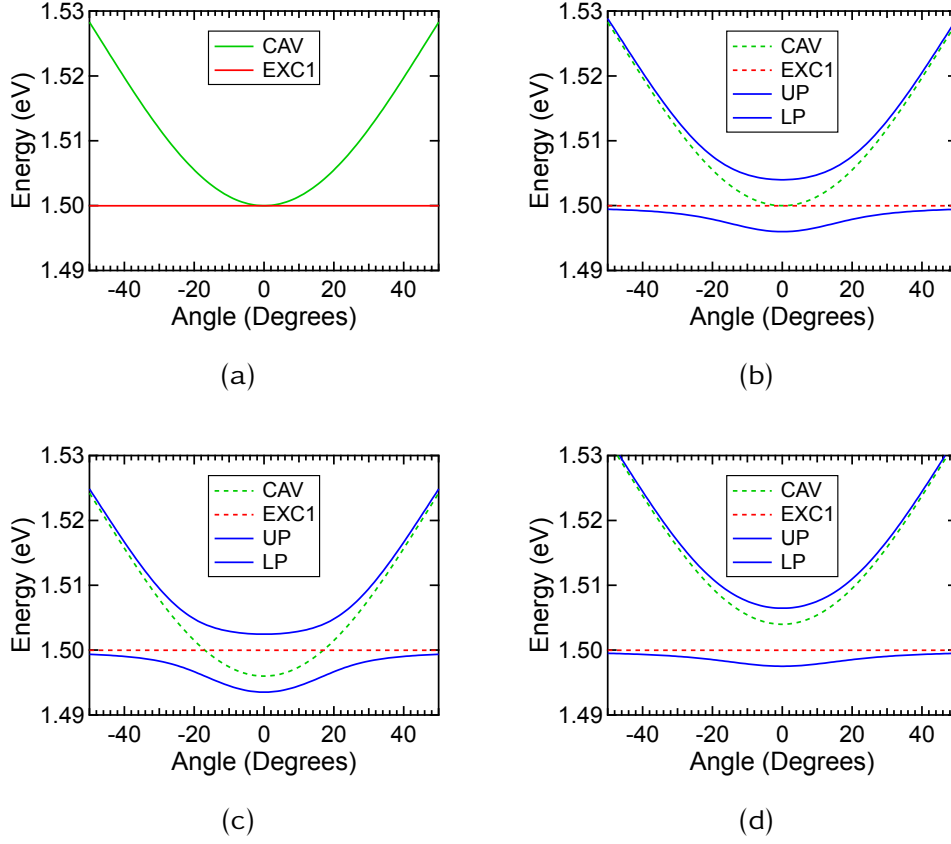


Figure 1.7: Dispersion of cavity photon and one exciton in weak coupling (a). Polariton dispersion curves for zero detuning $\delta = 0$ meV (b), negative $\delta = -4$ meV (c), and positive $\delta = 4$ meV (d), for the same coupling strength.

1.5 Polariton condensation and lasing

In physics, most of the times, the word condensation recalls the Bose-Einstein condensation (BEC). The BEC, like superfluidity and superconductivity, is related to a phase transition to a quantum condensate phase. The phenomenon of BEC is known since 1924 [12], when Satyendra Nath Bose and Albert Einstein theoretically predicted that above a critical density (or below a critical temperature), a large number of bosons can spontaneously occupy the same quantum state, at the lowest available energy of the system. A BEC is a highly coherent state of matter where all the particles have the same phase.

Despite the very early theoretical prediction of the BEC, the experimental

realization came almost 70 years later. The reason was the extremely low critical temperature which is below $2 \mu\text{K}$ (near absolute zero) in the case of the atomic systems. Such low temperatures can only be reached by using special techniques, like laser cooling and magnetic evaporative cooling. It wasn't until 1995, when the experimental realization of BEC was finally demonstrated. Within a few months, three different approaches succeeded in creating BEC in Rubidium [13], Lithium [14], and Sodium [15] atoms, to temperatures 170 nK, 100-400 nK, and $2 \mu\text{K}$ respectively, and densities $\sim 10^{12} - 10^{14} \text{ cm}^{-3}$. In 2001, The Nobel Prize in Physics was awarded jointly to Eric Cornell, Wolfgang Ketterle and Carl Wieman "for the achievement of Bose-Einstein condensation in dilute gases of alkali atoms, and for early fundamental studies of the properties of the condensates".

As mentioned above, one difficulty of BEC is the low critical temperature, therefore, research is focused on systems able to operate at higher temperatures. A way to increase the temperature is to use a system with lighter effective mass than atoms (or, as usually called, atomic gases), like excitons, or even better, polaritons. Table 1.2 compares the basic parameters of polaritons to semiconductor excitons and atomic gases, which are the major systems for quantum phase studies [16]. It can be seen that polaritons have 8 orders of magnitude smaller effective mass than atomic gases ($10^{-5} m_e$ compared to $10^3 m_e$ for atomic gases) and can create a system able to operate at higher temperatures (1 K - 300 K). These values of temperature are easily achievable by standard cryogenic techniques.

Parameter	Atomic gases	Excitons	Polaritons
Effective mass (m^*/m_e)	$\sim 10^3$	$\sim 10^{-1}$	$\sim 10^{-5}$
Bohr radius (\AA)	$\sim 10^{-1}$	$\sim 10^2$	$\sim 10^2$
Critical temperature	$\sim 1 \text{ nK} - 1 \mu\text{K}$	$\sim 1 \text{ mK} - 1 \text{ K}$	$\sim 1 \text{ K} - 300 \text{ K}$
Lifetime	$\sim 1 \text{ s}$	$\sim 1 \text{ ns}$	$\sim 1 - 10 \text{ ps}$
Thermalisation time	$\sim 1 \text{ ms}$	$\sim 10 \text{ ps}$	$\sim 1 - 10 \text{ ps}$

Table 1.2: Parameter comparison for condensation (or BEC) in atomic, excitonic, and polaritonic systems. Data from [16].

A restriction of polaritons is their very short lifetime (some ps compared to $\sim 1 \text{ s}$ for atomic gases), therefore, polariton condensation requires a

high quality MC and strong light-matter coupling, to create long-lived polaritons. Note that, the polariton effective mass and lifetime are predominantly determined by their photonic component, whose effective mass is much lighter and lifetime is much shorter than the excitonic part. The photons have a finite lifetime due to leakage of the light through the MC mirrors [17].

A first approach to polariton condensation was made in 2002 by Deng et al. [18], where a phase transition from a classical thermal mixed state to a quantum-mechanical pure state of polaritons was observed in a GaAs multiple QW MC. They observed a non-linear threshold behaviour in the pump-intensity dependence of the emission, a polariton-like dispersion relation above threshold, and a decrease of the relaxation time into the LP state. The first experimental observation of polariton condensation (with clear evidence) was presented in 2006 by Kaszpak et al. [19], where they demonstrated polariton condensation in CdTe/CdMgTe MC with 16 CdTe QWs. Above some critical density, condensation took place in the ground state, at 19 K. The phase-transition character of the phenomenon was clearly seen for the first time in the solid state, by the build-up of spatial coherence and macroscopic polarization across the entire condensate.

Polariton condensation is a very important phenomenon because it brings pure quantum effects to the macroscopic scale. It's also important to clarify that a polariton condensation is not the same as the atomic BEC, even if sometimes the term polariton BEC is used. BEC is based on an ideal bosonic gas in 3-Dimensions. Ideal bosonic gas means: non-interacting bosons and thermal equilibrium. A polariton condensation is not an ideal gas since polaritons interact with each other, it is not at thermal equilibrium¹, and the system is in 2-Dimensions. Actually, the only similarity between BEC and polariton condensation is that many bosons occupy the lowest quantum state. Although, this is not entirely true for every case. Here [20, 21], G. Tosi et al. and P. Cristofolini et al., demonstrated that coherence of polaritons is possible, not only in the ground state, but also in higher energy states, simultaneously.

A consequence of polariton condensation is the emission of coherent light. All started in 1996, when A. Imamoglu et al. [22] suggested the possibility for non-linear effects such as lasing, when they proposed a different type

¹The thermalisation time of polaritons is comparable to their lifetime (Table 1.2), meaning that polaritons, in contrast to atoms, do not reach thermal equilibrium.

of laser which operates without electronic population inversion and utilizes many-body coherences. They analyzed elementary properties of exciton and polariton lasers and they discussed the possibility of generating coherent light by spontaneous radiative recombination from a coherent polariton condensation. Before continuing with the polariton lasing phenomenon, it is important to mention that other types of light emitting devices, such as light emitting diodes (LEDs), have also been demonstrated. In 2008, two realizations of a polariton based LED using a GaAs MC with doped Bragg mirrors, operating at 10 K [23], and up to 100 K [24], were presented. Then, S. Tsintzos et al. presented an experimental realization of an electrically pumped semiconductor polariton LED, which emits directly from polariton states near room temperature (235 K) [25] and at room temperature (315 K) [26]. Temperature and angle-resolved electroluminescence measurements on the devices clearly showed the persistence of Rabi splitting and anticrossing behaviour. They also showed that by increasing the number of QWs in the structure, the cut-off temperature for the strong coupling regime can be pushed beyond room temperature, in good agreement with theory. These results are important for the realization of ultra-efficient polaritonic devices.

Laser light emission can be observed in both weak and strong coupling regimes [27], but only that coming from strong coupling can be described as polariton lasing. Emission from the uncoupled cavity mode (which is purely photonic) is photon lasing, while emission from the bottom of the LP branch is polariton lasing, however, the distinction is not always obvious [28]. A good approach to measure the two different lasing phenomena is by performing power dependent PL measurements. The log plot of the curve usually shows two S-like features as shown in Figure 1.8. The first in the low pump power position corresponds to polariton lasing, while the second in the higher pump power position corresponds to photon lasing. In general, lasing is shown in power dependent experiments, by a non-linear increase of light intensity and a simultaneous linewidth decrease of the emission peak. The main advantage of the polariton laser is the low lasing threshold. As mentioned earlier, due to a different operation principle, population inversion is not needed in a polariton laser, therefore, it is expected that the required pump power will be lower than that of a conventional laser based on weak coupling operation. In 2007, S. Christopoulos et al. [29] showed for the first time, room-temperature polariton lasing in bulk Gallium Nitride (GaN) MCs. They showed that luminescence from the LP branch exhibits a transition with a clear threshold to a coherent state which is localized in a few micron sized regions of the

excited sample.

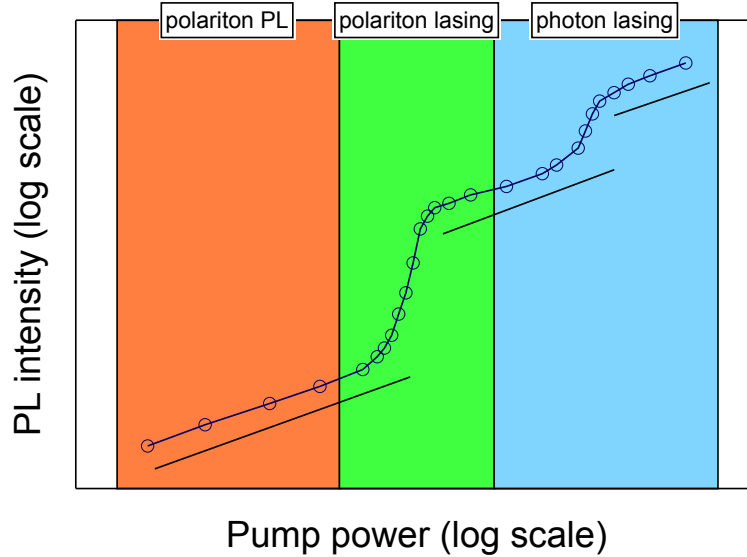


Figure 1.8: Schematic showing different zones of light emission. The first zone (orange) shows the linear response of polariton PL. Then, in the second zone (green), polariton condensation occurs and a non-linear increase of the emission is observed, resulting in polariton lasing. Lastly, in the third zone (blue), the SCR is lost and the bare cavity mode emits photon lasing.

Lastly, a practical polariton laser [30] should be able to operate under electrical injection at room temperature. Recently, in 2014, P. Bhattacharya et al. [31] demonstrated such a device, using a bulk GaN-based MC diode. The large exciton binding energy of the wide bandgap GaN creates robust excitons at room temperature, which is important for practical applications. A low non-linear threshold for polariton lasing was accompanied by a collapse of the emission linewidth and small blueshift of the emission peak. A second threshold, due to conventional photon lasing, was also observed. The above polariton laser is based on GaN, thus, light emission is in the ultraviolet (UV) region, which is also very important from a technological point of view. Nevertheless, polariton lasers have a main disadvantage, their emission power is very low, so for now, their potential applications are limited to those with low laser power requirements.

1.6 Terahertz radiation and bosonic cascade

Three topics will be presented in this section: THz radiation, the quantum cascade laser (QCL), and the concept of the BCL. Before describing these topics, I'll try to explain the main idea

The THz radiation has historically been characterized by a relative lack of efficient emitters, detectors, and transmission technology. Therefore, there is a continuous research effort to increase the number of devices able to emit and detect THz radiation. A successful step towards this direction was the QCL [32] which is based on subsequent intersubband transitions of electrons/holes in a semiconductor superlattice, under external electric field (Figure 1.9). The concept of the BCL was introduced to combine the QCL property of multiple THz photons emission from a single excitation, but in a simpler structure without a superlattice. Another approach for THz generation is the use of a single parabolic quantum well (PQW), which is the subject of the present thesis.

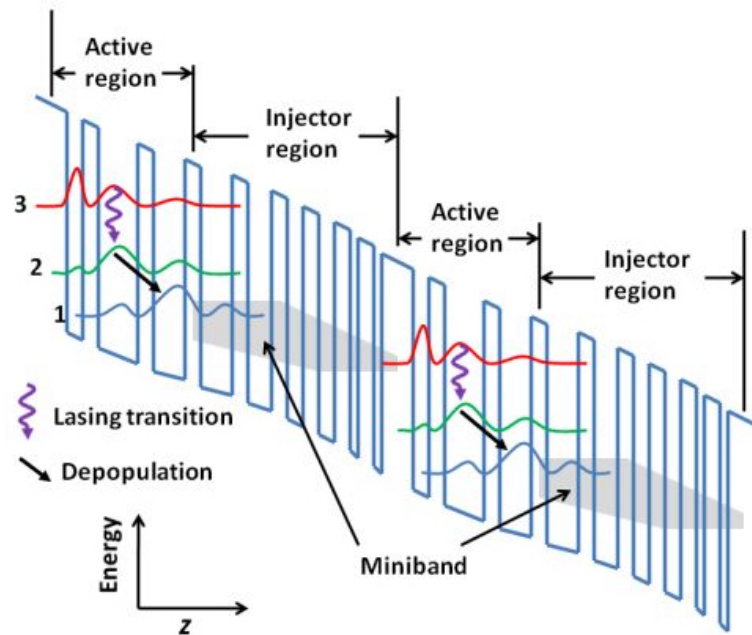


Figure 1.9: Schematic band diagram of two periods of a QCL structure [33].

1 THz has a wavelength of $300\ \mu\text{m}$, a photon energy of 4.1 meV, and a period of 1 ps. The THz region of the electromagnetic spectrum [34] is located between microwaves and infrared radiation, thus, it provides an

interface between electronics and optics. Although, the principles, measurements, and tools, used for optical and electrical waves are different, and THz do not simply fit into either category. For example, the equations that describe electronics (and electromagnetism in general) are the Maxwell equations, while in optics there are the Schrodinger equations. The main type of measurement in electronics is the electric field, while in optics is the intensity. Lastly, the tools used for electronics are circuits and antennas, while in optics are lens systems and mirrors.

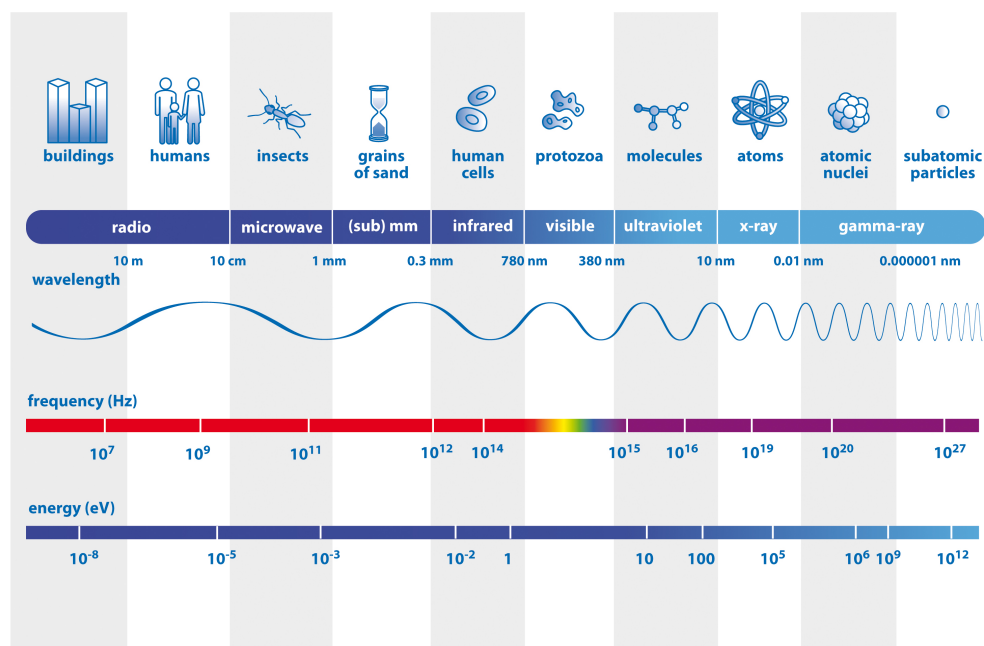


Figure 1.10: A scheme of the electromagnetic spectrum with indication of wavelengths, frequencies, and energies [35]. THz radiation is also known as sub-mm radiation.

Despite these difficulties, THz radiation has useful properties for applications [34]. First, it is non-ionising, which means that due to low photon energies, THz radiation cannot lead to photoionization in biological tissues (unlike X-rays). Also, due to extreme water absorption, THz waves cannot penetrate into the human body, therefore, even if THz waves do cause any harm, it is limited to skin level. Second, THz waves have longer wavelengths than visible light, are less affected by Mie scattering, and are transparent to most dry dielectric materials, such as cloth, paper, wood, and plastic. That's the reason why they are considered very promising in non-destructive evaluation applications. Third, many biological and

chemical compounds have distinct signature responses to THz waves due to their unique molecular vibrations and rotational energy levels, therefore, it is possible to use THz spectroscopy for characterization, and examination of the chemical composition. Additionally, the THz frequency range, often mentioned as 0.1 to 10 THz (~ 0.4 to 40 meV), is of great importance to inorganic semiconductor studies. The THz electric field can stimulate charged carriers such as electrons, holes, excitons, and plasmons, as well as collective excitations such as phonons. It is also sensitive to the conductivity of inorganic semiconductor materials because it is close to their carrier's scattering rates.

The development of the femtosecond laser enabled a new spectroscopic method known as terahertz time domain spectroscopy (THz-TDS). The technique was first described in 1989 [36] and was relied on the optical excitation of photoconductive dipole antennas [37, 38, 39]. Various methods have been used to handle THz radiation, but the most common ones for broadband pulsed THz beams are photoconductive antennas and optical rectification (second-order non-linear effects in electro-optic crystals) [39, 40]. In the present thesis, we use photoconductive antennas for both generation and detection of THz pulses.

A photoconductive antenna [34] consists of a semi-insulating semiconductor substrate, preferably with high carrier mobility (for high generation efficiency), short carrier lifetime (for high response speed), and high dark resistance (for sufficient breakdown voltage). Two metal electrodes with a gap between them are coated to the substrate (Figure 1.11). Since the substrate is semi-insulating, electric energy from an applied voltage can be stored in the gap area. Laser pulses act like switches to open this reservoir of electric energy and release it in the form of THz pulses. Polarization of the THz waves is parallel to the biased field which in turn is perpendicular to the strip lines of the antenna. The same antenna can be used both as an emitter or detector, depending on whether it is biased or not. In both cases, ultrafast laser pulses are needed to induce photo-carriers. A material that is commonly used is low temperature grown Gallium Arsenide (LT-GaAs), which is GaAs grown by molecular beam epitaxy at low temperatures, typically in the range of 180-300 K. The lower the temperature of the growth the shorter the carrier lifetime of the sample. A detailed analysis of our THz-TDS experimental setup is presented in Section A.5.

As previously mentioned, one of the main disadvantages of THz radia-

tion in general, is the lack of reliable, compact, and tunable sources. A great achievement towards this direction was the demonstration of THz QCLs, which can now deliver mW of continuous-wave (CW) coherent THz radiation [32]. In 1971, R. F. Kazarinov and R. A. Suris [41] proposed a theoretical scheme where amplification of electromagnetic waves can be obtained, exploiting a series of intersubband electron transitions, by applying external electric field in a semiconductor superlattice. It wasn't until 1994 that the first QCL was experimentally realised by J. Faist, F. Capasso, et al. [42]. It was designed by proper band structure engineering and was grown by molecular beam epitaxy.

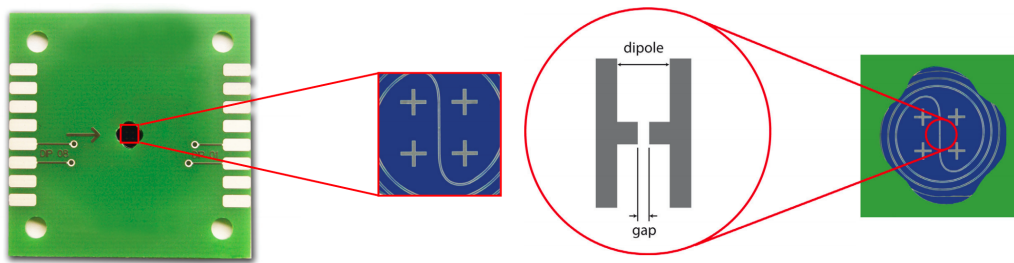


Figure 1.11: Picture of a photoconductive antenna showing the single dipole structure. There is one wrapped dipole structure on the chip and the chip is mounted on a PCB [43].

In conventional semiconductor lasers, light is generated by the radiative recombination of conduction band electrons with valence band holes across the bandgap of the active material. In contrast, electrons in a QCL propagate through a potential ladder of coupled QWs, where the conduction band is split by quantum confinement into a number of distinct subbands. By changing the layer thickness and the applied electric field, lifetimes and tunnelling probabilities of each level can be controlled, to obtain population inversion between two subbands, in a series of identical repeats. The radiation frequency is determined by the energy spacing of the lasing subbands, allowing in principle operation at long wavelengths. In practice, the intersubband transitions pose limitations to the QCL performance, suppressing the emission to the infrared (IR) wavelength range.

In the first demonstration of the QCL [42], electrons were streaming down a potential ladder, sequentially emitted photons at the steps. The steps consisted of coupled QWs in which population inversion between discrete conduction band excited states was achieved by control of tunneling. A strong narrowing of the emission spectrum, above threshold, provided direct evidence of lasing in the IR frequency range, at a wavelength of 4.2

μm , with peak power of 8 mW in pulsed mode operation.

Six years later, in 2002, the first THz-QCL was demonstrated by R. Kohler et al. [44]. They reported a monolithic THz injection laser that was based on interband transitions in the conduction band of a GaAs / AlGaAs semiconductor heterostructure. The structure emitted a single mode at 4.4 THz and showed output power of more than 2 mW. In the last years [32], there are several reports which demonstrate spectral coverage in the range of 0.84-5 THz [45, 46], at temperatures up to 164 K pulsed, and 117 K CW, at approximately 3 THz [47], and output powers up to 248 mW pulsed, and 138 mW CW [48]. Furthermore, a demonstration of a room temperature THz QCL source based on intracavity difference-frequency generation has been presented [49]. They demonstrated devices that operate in mid-IR at 8.9 μm and 10.5 μm and produce THz output at 60 μm via difference-frequency generation with 7 μW at 80 K, 1 μW at 250 K, and approximately 300 nW at 300 K [49]. Difference-frequency generation is a non-linear optical process in which two beams at frequencies ω_1 and ω_2 interact in a medium with effective second-order non-linear susceptibility $\chi^{(2)}$ to produce radiation at frequency $\omega_3 = \omega_1 - \omega_2$.

Perhaps, one of the most important limiting factors of the QCL is the Pauli exclusion principle, which prevents an electron to propagate to the lowest level of the ladder, if this level is already occupied [50]. The concept of the BCL has been proposed [51] to overcome this limitation by replacing the use of fermionic statistics with bosonic. In contrast to the kinetics of fermions, kinetics of bosons allow the transition to the lowest occupied level. The authors proposed a new scheme where excitons are used instead of electrons, exploiting the equidistant levels of a PQW to form the ladder. The bosonic cascade is defined as a series of bosonic energy levels with equal, in the THz range, energy spacing [52]. A boson excited in the highest level can follow a chain of transitions, generating multiple THz photons. The difference between a bosonic cascade and a fermionic one, is that in the bosonic system, the strength of relaxation processes is enhanced by bosonic stimulation. The bosonic final state stimulation enhances the scattering rates such that even in the limit of a weak spontaneous scattering rate, particles can reach the ground level of the cascade [52].

Specifically, the theoretical description starts by considering the weak coupling regime where the optical mode is resonant with the highest excitonic level. The other energy levels are uncoupled to the cavity mode.

The device would emit radiation propagating in the cavity plane in the wave guiding regime. The following set of rate equations was introduced to theoretically describe the BCL [51]:

$$\frac{dN_m}{dt} = P - \frac{N_m}{\tau} - WN_m(N_{m-1} + 1) + W'N_{m-1}(N_m + 1) \quad (1.24)$$

$$\begin{aligned} \frac{dN_k}{dt} = & -\frac{N_k}{\tau} + W[N_{k+1}(N_k + 1) - N_k(N_{k-1} + 1)] \\ & + W'[N_{k-1}(N_k + 1) - N_k(N_{k+1} + 1)] \\ & \forall 2 \leq k \leq m-1 \end{aligned} \quad (1.25)$$

$$\frac{dN_1}{dt} = -\frac{N_1}{\tau} + WN_2(N_1 + 1) - W'N_1(N_2 + 1) \quad (1.26)$$

$$\begin{aligned} \frac{dn_{THz}}{dt} = & -\frac{n_{THz}}{\tau_{THz}} + W \sum_{k=2}^m N_k(N_{k-1} + 1) \\ & - W' \sum_{k=2}^m N_{k-1}(N_k + 1) \end{aligned} \quad (1.27)$$

where m is the highest energy state which is resonantly pumped with rate P and 1 is the lowest energy state, with N being the population of the state. W is the THz emission rate and W' is the THz absorption rate. The lifetime of the cascade levels τ , includes both their radiative and non-radiative decay rates, which includes losses due to phonon scattering. n_{THz} is the THz mode occupation and τ_{THz} is the THz mode lifetime.

A generic scheme of the BCL is presented in Figure 1.12. A series of equidistant energy levels with N population are coupled via THz radiative transitions, having a spontaneous scattering rate W [52]. The highest energy level m is resonantly pumped at rate P and all levels dissipate energy at rate τ^{-1} . The THz mode enters the system at rate P_{THz} , experiences gain Γ from cascade relaxation processes, and leaves it at a rate τ_{THz}^{-1} . When the external THz mode is taken into consideration, the scattering between the modes is further stimulated and enhanced, due to macroscopic number of THz photons. A more detailed analysis of our theoretical model can be found on Section 3.5.

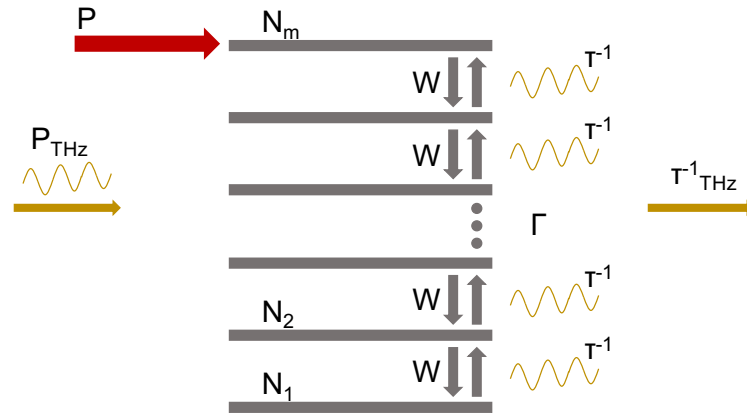


Figure 1.12: Schematic of a BCL. P : cascade pump rate, P_{THz} : THz field, N : population of the level, W spontaneous scattering rate, τ : lifetime.

As already discussed, a PQW is important for the ladder of the equally spaced² levels and for the experimental understanding and the physical impementation of the BCL concept. A study of a single PQW MC for THz cascade is presented in the next chapter.

²Almost-equally spaced. The energy states are equally spaced, the excitonic states are not exactly equally spaced due to their binding energy.

Chapter 2

A PARABOLIC QUANTUM WELL STUDY

This chapter presents a study of PQW structures for THz cascade. After a general introduction, the samples are described, followed by the study of a single PQW without a MC. Then, a similar PQW is embedded in a MC, it is optically characterized, and the results are presented.

2.1 Introduction

The THz spectral region (~ 0.1 to 10 THz) remains one of the most unexploited parts of the electromagnetic spectrum, despite its potential applications in various fields such as medicine, biosensing, and industrial inspection. The main reason has been the lack of reliable and efficient radiation sources, which makes the development of such emitters a technological challenge of high importance. This is mainly due to the fact that direct generation of THz radiation is limited by the lack of materials with appropriately small bandgap. A great achievement towards this direction is the development of QCL demonstrated in 1994 with a frequency of 75 THz [42]. Contrary to typical semiconductor lasers which use interband transitions to emit light, QCLs use intersubband transitions which nowadays are able to produce light with even lower frequency, typically in the 1 to 5 THz range [45, 46]. To combine strong optical gain and carrier transport through the device, a complex band structure is required, particularly because the active region is repeated several times [32].

Alternative ways for the emission of THz photons using MC systems in the SCR [53, 54, 55, 56, 57, 58, 59] have been recently proposed [51, 60, 61]. Such devices are based on the strong coupling between light (photons in a cavity) and matter (excitons in semiconductor QWs forming new quasi-particles called polaritons. Theoretical proposals describe the production of THz emission from the transition between the UP and LP state [60] and the use of the oscillation of the dipole moment of polaritons from coupled QWs [61]. Of particular interest is a recent theoretical proposal of

a BCL using the equally spaced excitonic levels of a PQW [51]. In polaritonic structures the possibility to have a macroscopically occupied ground state is expected to enhance the transitions to the ground state (through bosonic stimulation) and thus improve THz emission. Therefore, the study of semiconductor MCs utilizing PQW capable of supporting stimulated cascaded relaxation between equidistant energy levels for THz emission is imminent.

This chapter reports on the SCR in a MC containing a PQW [51, 60, 62, 63, 64]. When the PQW is studied alone [65], the expected equally spaced excitonic transitions are observed. When placed in a MC, the full structure exhibits a clear anticrossing between the ground state heavy hole (hh) / light hole (lh) excitons and the cavity mode, revealing the SCR. The study of the excitonic relaxation shows oscillations with frequencies in the THz range. Furthermore, under non-resonant optical excitation, the MC exhibits stimulated emission in the weak coupling regime. This is a necessary prerequisite for a cascaded bosonic relaxation which will result in THz emission.

2.2 Samples

Both samples under study were grown by molecular beam epitaxy on n^+ GaAs substrate with n^+ GaAs buffer layer and a GaAs cap layer on the top to prevent them from oxidation. The first one is a single PQW grown by varying the Aluminum concentration of $\text{Al}_x\text{Ga}_{1-x}\text{As}$, producing a 50 nm QW at the top of potential profile with its band structure presented in Figure 2.1 (a). The parabolic potential is broken into several linear growth segments and the Aluminum concentration is adjusted continuously during growth. The structure was designed to provide a reasonable number (≈ 15) of equally spaced excitonic energy levels which include both hh and lh excitonic transitions. All allowed transitions are shown with arrows in Figure 2.1 (a).

In the second sample (Figure 2.2) a similar PQW was embedded inside a MC. A λ cavity layer was sandwiched between two $\text{Al}_{0.15}\text{Ga}_{0.85}\text{As}/\text{AlAs}$ DBRs with 22 pairs for the bottom one and 17 for the top one. The PQW was inserted at the center of the $\text{Al}_{0.15}\text{Ga}_{0.85}\text{As}$ cavity layer at the antinode of the electric field to maximize the light-matter coupling. Figure 2.1 (b) is a SEM image which shows the central region of the MC and Figure 2.1 (c) is the calculated electric field along that part of the structure.

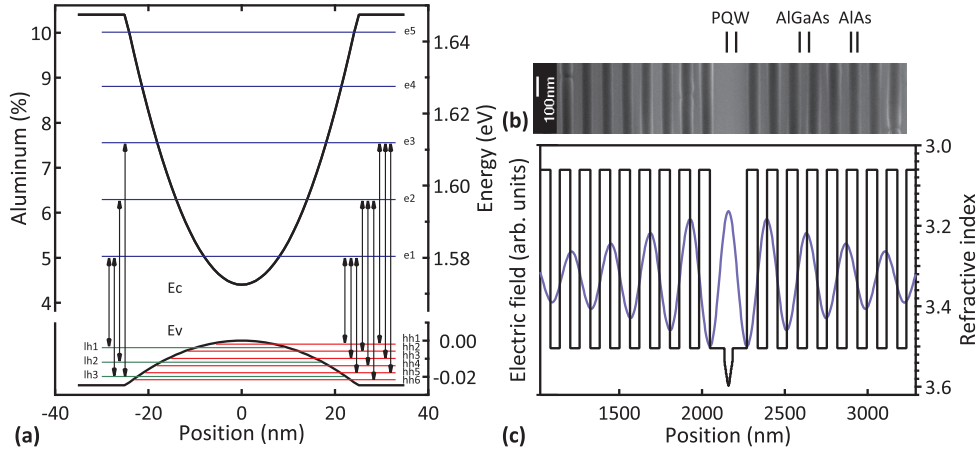
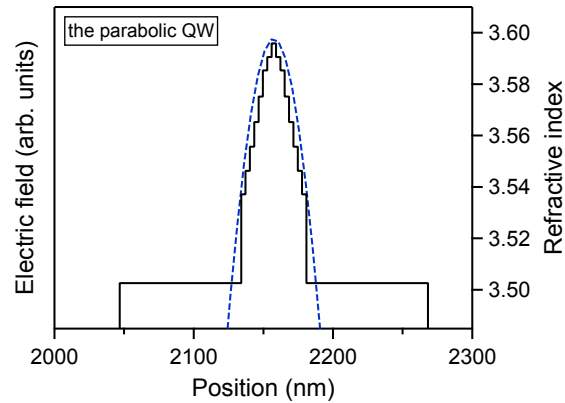


Figure 2.1: (a) The designed PQW composition profile ($\text{Al} \approx 4.5\% - 10.5\%$), calculated valence (E_v) and conduction (E_c) bands, electron (e), heavy hole (hh) and light hole (lh) energy levels with the allowed transitions (vertical arrows). (b) SEM image of the central region of the MC and (c) the corresponding simulation of the electric field along the structure and the refractive index distribution inside the MC.

SAMPLE 242

9	GaAs 60 Å	
8	AlGaAs 561.4 Å Al=15%	x17
7	AlAs 642.6 Å	
6	AlGaAs 872 Å Al=15%	
5	AlGaAs PARABOLIC 500 Å	
4	AlGaAs 872 Å Al=15%	
3	AlAs 642.6 Å	x22
2	AlGaAs 561.4 Å Al=15%	
1	n+ GaAs buffer	
n+ GaAs(100)		

(a)



(b)

Figure 2.2: (a) The MC structure with the embedded PQW. (b) The PQW design, zoom-in from Figure 2.1 (c). The design code is shown in Appendix B.2.

2.3 Excitonic levels and terahertz oscillations

We first assess the quality of the PQW by measuring the different excitonic levels, at 28 K, in the structure without MC. Brewster angle reflectivity (Appendix A.3.2) was employed to probe these transitions due to its high signal to noise ratio. At the Brewster angle, the reflection from the surface of the sample is greatly reduced and, consequently, the sensitivity to the refractive index modulations caused by the excitonic resonances is increased. In our setup, light from a halogen lamp passes through a polariser to acquire transverse magnetic (TM) polarisation, a lens is used to focus the light on the sample and a mirror to guide it on the specific Brewster angle ($\approx 74^\circ$). The reflectivity is collected and sent to a spectrometer coupled to a liquid-nitrogen-cooled charged coupled device (CCD).

Figure 2.3 (a) shows the Brewster angle reflectivity spectrum of the PQW (right side of the graph). Both hh and lh excitons from the fundamental transition can be seen with a 2.6 meV splitting. At higher energies, smaller spectral features that we attribute to specific excitonic transitions are visible, noted with the respective numbers. The electron-hole energy levels were calculated by solving the Schrodinger equation while the binding energies were computed by the variational method [66, 67]. Some transitions are not clearly noticeable due to their lower oscillator strength. The extracted energy positions of all observed states are plotted in the inset graph showing the expected equally spaced optical transitions with energy separation of ~ 4.3 meV. These equally spaced energy levels are characteristic of harmonic confinement proving the successful realisation of the parabolic profile and potentially allow the bosonic cascade THz emission recently proposed [51]. The area of the circular markers (log scale) is proportional to the calculated oscillator strength of the excitonic levels. Good agreement between measured reflectivity dips and calculated oscillator strengths is found. Potential discrepancies could result from deviations from the parabolic potential of the fabricated QW which could slightly modify the energy positions of some of the excited states.

In order to reveal the potential of the PQW for THz generation we study the dynamics of excitonic relaxation by using pump-probe spectroscopy (Appendix A.6). In our setup, the 80-femtosecond pulses from a Ti:Sapphire laser are used for the pump and probe beams. The reflectivity of the probe beam is measured at normal incidence geometry, by using a monochromator with a photodiode connected to a lock-in amplifier. This spectral

selection allowed us to detect signal for different excitonic transition as a function of delay between the pump and probe pulses.

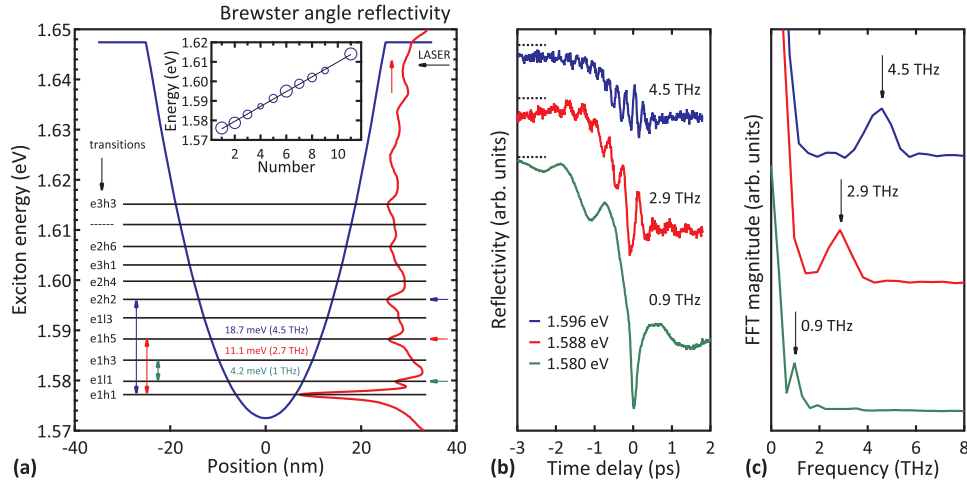


Figure 2.3: (a) Potential profile in the PQW (blue line) and reflectivity spectrum in Brewster angle configuration (red line, right side), horizontal black lines show the excitonic energy levels. (a) (inset) Energy position of the excitonic transitions (open circles) along with a linear fit (black line). The area of the circles (log scale) is proportional to the corresponding oscillator strength of each excitonic level. (b) Pump-probe reflectivity measurements in three different detection energies, which are shown in (a) with horizontal colored arrows, demonstrating the quantum beats of different excitonic states, which are shown in (a) with vertical colored arrows. The colored numbers in (a) are the energy (frequency) distances between the interfering states obtained from the reflectivity spectrum. Time traces were vertically spaced for clarity and zero baselines are shown with horizontal dashed lines. (c) The Fast Fourier Transform of the time traces.

Figure 2.3 (b) shows the pump-probe reflectivity measurements for three different detection energies. These show pronounced oscillations, which we interpret as quantum beats between the 1st and 6th, 1st and 4th, 2nd and 3rd excitonic levels. Quantum beating is not a proof of the cascade relaxation, however, it is an indication of real and pure excitonic states able to support transition between them. The frequencies of oscillations (extracted by Fast Fourier Transform shown in Figure 2.3 (c)), are in the THz range, 4.5 THz, 2.9 THz, and 0.9 THz, corresponding to energy separation of 18.6 meV, 12 meV, and 3.7 meV respectively. Vertical arrows

of corresponding colors in Figure 2.3 (a) show the excitonic levels which contribute to the quantum beats. This data demonstrates that excitons occupying different quantum confined states in PQW maintain mutual coherence for a few picoseconds, defined by the decay time due to inhomogeneous broadening of the excitonic states in the structure under study. We note here, that any remaining background in Figure 2.3 (b) is due to the long-lived excitonic reservoir states which have typical lifetimes of several nanoseconds [68].

2.4 Strong coupling and non-linear emission

We now study the possibility of achieving the SCR with such a PQW embedded in a MC. For that, we characterized our MC sample at 28 K using a PL imaging setup. The sample is excited with a tuneable continuous-wave Ti:Sapphire laser, at a wavelength corresponding to the first minimum of the DBR reflectivity on the high energy side of the spectrum (753 nm), just below AlGaAs barrier absorption, to directly inject carriers in the PQW. Laser light is focused through an objective lens and the emission at the Fourier plane is imaged on the entrance slit of an imaging spectrometer coupled to a liquid-nitrogen-cooled CCD.

Figure 2.4 (a) shows the measured energy versus angle PL image of the sample. A strong emission peak exhibiting the characteristic dispersion of a lower LP branch is clearly visible. By saturating the color scale it is possible to observe two extra polariton branches, the middle (MP) one and the upper (UP) one (Figure 2.4 (a) inset). These three branches reveal the SCR involving both the hh and lh excitons. The fitted polariton branches were extracted by a 3×3 coupled harmonic oscillator model [69, 70] and the characteristic anticrossing behaviour of the SCR is observed. The hh-lh energy separation is 2.7 meV which is in good agreement with the reflectivity measurement on the bare PQW.

To examine the non-linear emission characteristics of this PQW MC we measure power dependent PL under excitation at the reflectivity dip at the edge of the DBR stop-band and tuned just below AlGaAs barrier energy to avoid absorption and to ensure that all light is absorbed by the QW. The measured normal incidence PL spectra with increasing excitation power, taken for optimal exciton-photon detuning, are plotted in Figure 2.4 (b) (i). It shows an initially linearly increasing emission and blueshift presented in Figure 2.4 (b) (iii). At higher powers, non-linear stimulated emission is

observed with simultaneous line narrowing, plotted in Figure 2.4 (b) (ii), and collapse of SCR. Further evidence for stimulated relaxation is obtained from two-pump time-resolved experiments [71], presented in the next chapter, which show strong enhancement of the PL spectrum just below threshold for small time delays.

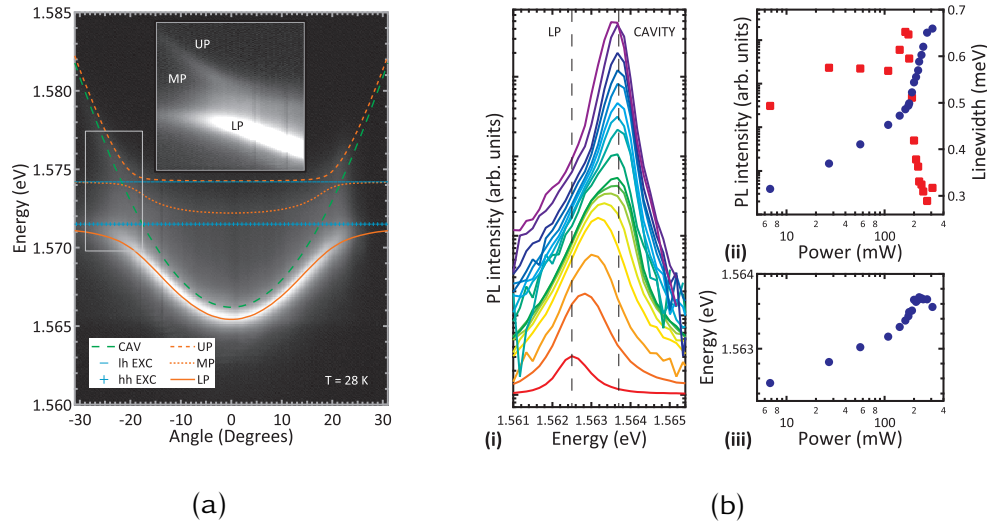


Figure 2.4: (a) Energy versus angle PL image and dispersion fittings obtained from the solutions of a 3×3 coupled harmonic Hamiltonian. Heavy hole (hh) and light hole (lh) excitons (horizontal plus and minus symbols respectively). Polariton branches, upper (dashed line), middle (dots), lower (continuous line). Cavity mode (parabolic dashed line). (b) (i) PL spectra at normal incidence to the sample for an increasing power. (ii) The integrated PL (circles) along with the linewidths (squares) versus power and (iii) the corresponding peak positions. The dispersion of (a) and the power dependence of (b) were performed at different exciton-photon detuning conditions.

The collapse of the SCR is observed from the position of lasing emission peak which coincides with the modelled bare cavity mode energy obtained from the fit to the polariton dispersions (Figure 2.4 (b) (i)). Here, we note that although the observed non-linear emission is not achieved in the SCR, nevertheless, it is a potential sign of bosonically enhanced relaxation in this system which could be utilized for THz emission as proposed in [51]. However, deterministic answer requires further experiments and is a subject of ongoing investigation.

2.5 Conclusion

In conclusion, we observe the expected equally spaced excitonic transitions of a PQW and quantum beating at THz frequencies between the discrete energy levels of QW excitons. When a single PQW is placed in a MC, the full structure shows a clear anticrossing between heavy hole / light hole excitons and the cavity mode, revealing the SCR. Furthermore, under non-resonant optical excitation, the MC exhibits non-linear stimulated emission. Such results constitute the first step towards the development of THz emitters based on bosonic cascade.

Chapter 3

ENERGY RELAXATION DYNAMICS

This chapter presents a study on the energy relaxation dynamics in [PQW](#) structures and, for comparison, in conventional rectangular [QW](#) structures. After a short introduction, the samples are described followed by the study of a single [PQW](#). Then, the exciton dynamics of two [MC](#) structures are presented. This work is important for further understanding of the bosonic cascade concept and the stimulated relaxation phenomenon.

3.1 Introduction

Here, we continue the project of the [PQW](#) started in the previous chapter by presenting further studies of the relaxation dynamics in [PQW](#) structures. First, we present the reflectivity spectrum and the power dependent [PL](#) of the single [PQW](#) without a [MC](#). Then, we study the non-trivial exciton dynamics of the bosonic cascade [MCs](#) by employing a pump-pump technique and compare it to a conventional structure containing rectangular [QWs](#). Excitons relax much faster in the parabolic potential, which seems to be an indication of stimulated relaxation in the bosonic cascade.

3.2 Samples

Three semiconductor samples were grown by molecular beam epitaxy for the purpose of this study. One sample with a single [PQW](#) and two [MC](#) samples, one with a single [PQW](#) and one with multiple rectangular [QWs](#).

More specifically, sample 1 is a single [PQW](#) grown by varying the Indium concentration of Indium Gallium Arsenide ([InGaAs](#)) producing a 50 nm [QW](#). The parabolic potential is broken into several linear growth segments and the Indium concentration is adjusted continuously during growth, from $\sim 2\%$ near the [InGaAs/GaAs](#) interface to $\sim 6\%$ in the middle of the [QW](#). [InGaAs](#) is chosen to mainly observe the intense [hh](#) excitons and avoid [lh](#)

excitons, due to material's larger separation between hh and lh energies.

Sample 2 is a MC structure containing a single PQW grown by varying the Aluminum concentration of $Al_xGa_{1-x}As$, from $\sim 10.5\%$ near the $AlGaAs/AlAs$ interface to $\sim 4.5\%$ in the middle of the PQW , producing a 50 nm PQW . A λ cavity layer was sandwiched between two $Al_{0.15}Ga_{0.85}As/AlAs$ DBRs with 22 pairs for the bottom one and 17 for the top one. The PQW was inserted at the center of the $Al_{0.15}Ga_{0.85}As$ cavity layer at the antinode of the electric field to maximize the light-matter coupling.

Sample 3 is a $5\lambda/2$ MC having two $Al_{0.15}Ga_{0.85}As/AlAs$ DBRs with 35 pairs for the bottom one and 32 for the top one. 12 rectangular GaAs QW s are embedded in the cavity layer.

3.3 Excitonic levels and indication of a cascade mechanism

We first assess the quality of the PQW by measuring the different excitonic levels of sample 1, at 5 K. This time, instead of Brewster angle reflectivity, we employ a different method, the λ -modulated reflectivity (Appendix A.7). Figure 3.1 (a) shows the reflectivity spectrum where 11 excitonic states can be identified, having an energy spacing of ~ 6 meV (~ 1.45 THz).

Power dependent PL measurements were performed, as shown in Figure 3.1 (b). The sample was excited with a CW laser, resonantly tuned to the barrier layer above the 11^{th} quantum confined excitonic state. The integrated PL peaks versus pump power, corresponding to specific transitions, are plotted in Figure 3.1 (b). It can be seen that PL intensity from the lowest level increases and then saturates, as power increases. At the same time, PL intensity from the excited levels follows a similar behaviour, it increases and then saturates, as power increases. The full set of the PL data was analyzed by the deconvolution of each spectrum into a set of Lorentzian curves which correspond to different excitonic transitions. As earlier mentioned, the pump is resonantly tuned to the excitonic resonance in the barrier layers, thus it directly creates excitons rather than uncoupled electron-hole pairs. The relaxation of electron-hole pairs differs from the relaxation of the excitons. If electron-hole pairs are created by non-resonant excitation, a broad background appears in the PL spec-

tra. The important result here is that the observed behaviour of the time integrated PL intensities of resonant excitonic peaks is a characteristic of PQWs. It's an indication that excitons may relax via a cascade mechanism between neighboring energy levels.

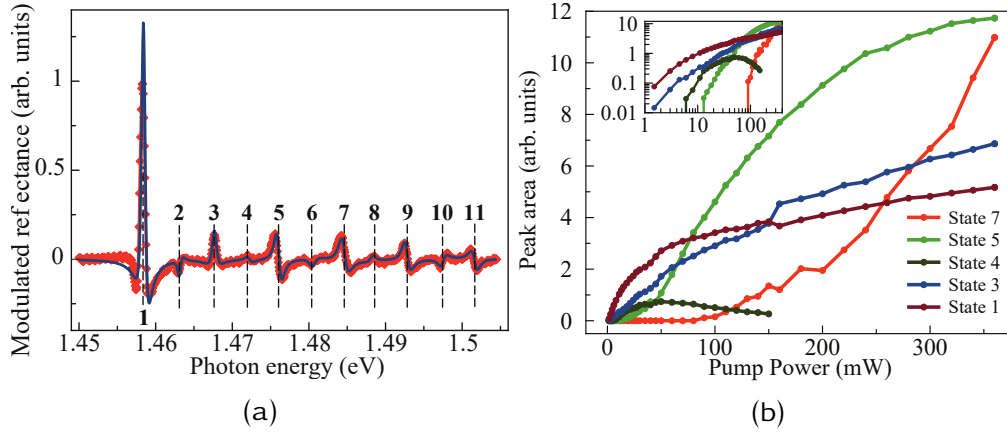


Figure 3.1: (a) λ -modulated reflectivity spectrum of the single PQW without MC (sample 1) showing the equally spaced quantum confined excitonic states. (b) Power dependent PL from different quantum confined excitonic states. The pump wavelength was tuned to the excitonic resonance in the barrier layer (above the 11th excitonic state). The inset presents the same curves plotted in logarithmic scale to reveal the low power region.

3.4 A comparative study of exciton relaxation

To investigate the relaxation processes in the PQW MC structure, a double pump PL technique is used (Appendix A.8). The important property of the stimulated cascade relaxation is its strong dependence on the lower excitonic state. The double pump method is based on the typical PL experiment but instead of one pump pulse, employs two pulses with a controlled time delay between them. The first pulse creates an initial exciton density and the second pulse creates additional excitons at the highest level. The relaxation of such excitons strongly depends on the population of the low energy excitonic levels created by the first pump pulse. If this population is large enough, the stimulated relaxation is triggered and accelerated (Figure 3.2). This acceleration should result in a non-linear increase of the total PL.

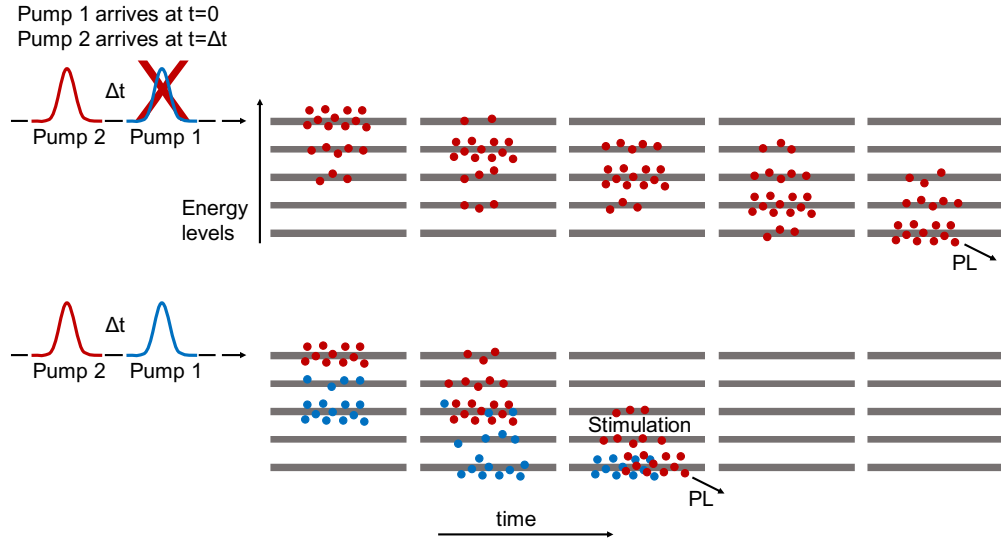


Figure 3.2: The relaxation of the excitons is accelerated when a critical exciton population already exists in the low level (blue oval). The excited excitons from the second pulse (red oval) in the double pulse case, need less time to relax compared to the case where no other excitons exist in the low level (single pulse case).

In addition, it is expected that the PL intensity will depend on the delay between the two pulses. Non-linear PL increase should not occur at very large delays, where the excitons created by the first pulse relax and recombine before the second pulse arrives. We use the double pump method to study the two MC samples, sample 2 with the PQW and sample 3 with the rectangular QWs. The samples were cooled down to 5 K and the time integrated PL spectra were acquired as a function of the time delay.

Figure 3.3 shows PL spectra versus the delay time for different pump power values, for both MC samples. The pump power values were chosen to be close to the lasing threshold. There are several points to discuss here.

First, there is an initially PL increase at the first negative delay times. The delay range is considerably smaller for the PQW sample which is around 150 ps (the graph shows from -150 to 0 ps), compared to the other sample which needs several hundred ps. Second, a narrow dip at delay 0 appears in sample 2 (PQW) but doesn't appear in sample 3 (rectangular QWs). This is an indication of different relaxation processes in these samples.

Third, both samples have an asymmetry for negative and positive delay times. This is caused by the difference in the pump power values of the two pulses. When the weak pulse comes first (negative delay), the exciton population is relatively low, therefore, the bosonic stimulation is weak and the exciton relaxation is slow. When the strong pulse comes first (positive delay), the stimulated relaxation occurs and accelerated. Lastly, an additional peak appears in both samples for positive delay time values, when the pump power exceeds the lasing threshold power. It is narrower and in a shorter delay time in sample 2, compared to sample 3, due to faster relaxation dynamics in the sample with the PQW.

To better understand the second peak, the results from another study, related to the time dependence of PL intensity, can be used [72]. PL kinetics were studied at different excitation powers for both below and above the polariton lasing threshold (P_{th}). It was found that, when $P < P_{th}$, PL intensity slowly rises and reaches its maximum at $\sim t_1 = 100$ ps. Then, PL intensity slowly decreases with a characteristic decay time of $\sim t_2 = 400$ ps. When $P > P_{th}$, a strong pulse of polariton laser emission appears at time t_1 with a 10-20 ps pulse duration. These findings allow us to assume the following for our results. When the sample is pumped by two pulses and the first pulse has higher power than the threshold, two maxima of the polariton laser emission may be seen. The reason is that the number of excitons remained after the first pulse of the polariton lasing peak plus the number of excitons created by the second pulse, is sufficient enough for the formation of a second peak of polariton laser emission. This double appearance of polariton lasing is seen in both samples, but the time delay and the width of the second peak strongly depends on the relaxation dynamics. It can be concluded that the relaxation in sample 2 is faster than in sample 3.

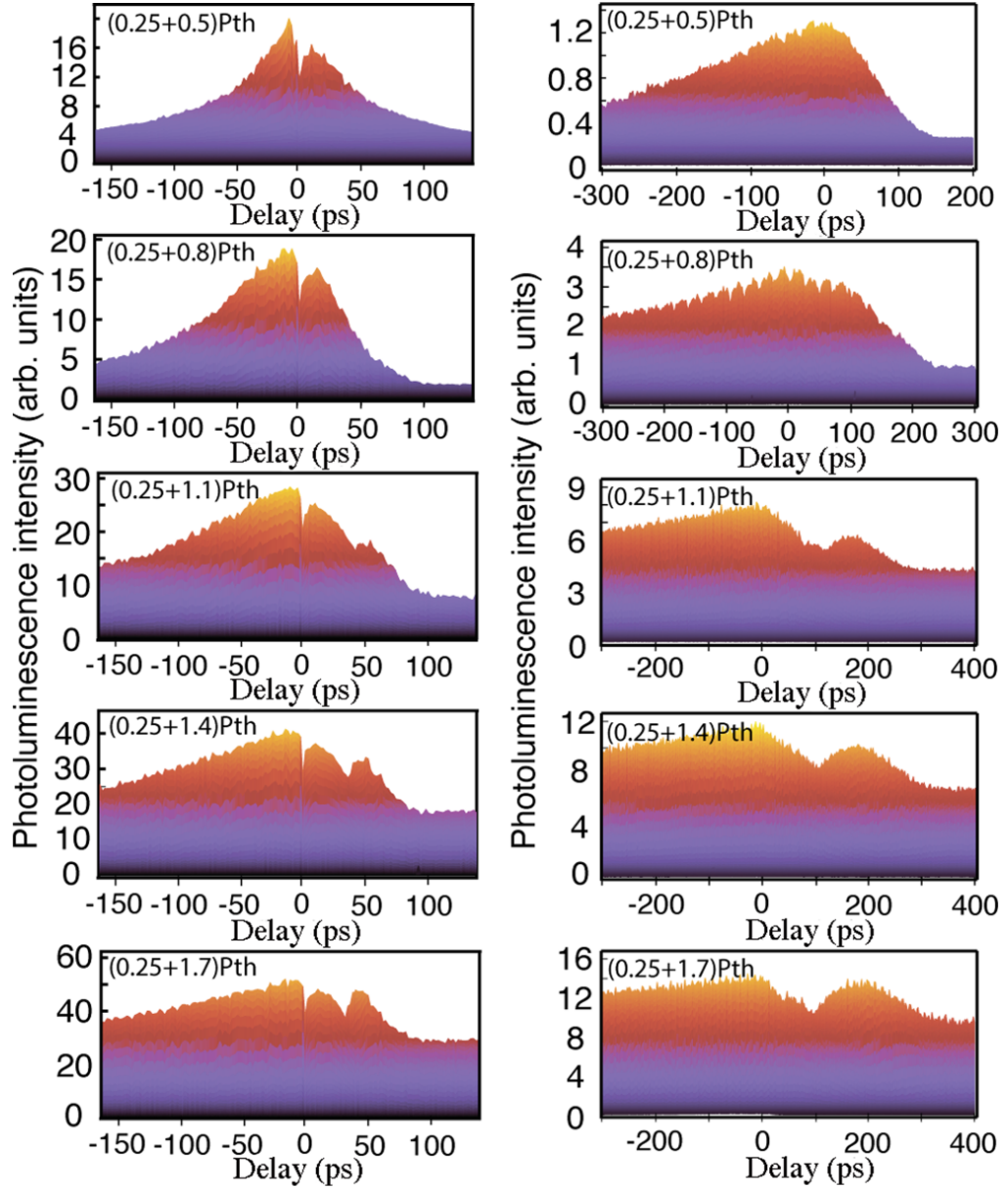


Figure 3.3: PL intensity versus the delay time between the two pump pulses for different pump power values. (left) Sample 2 with PQW and (right) sample 3 with rectangular QWs.

3.5 Theoretical modeling

For a theoretical analysis of our PQW structures, we start from the rate equations introduced in [51]. Considering m the maximum number of the excitonic levels in a PQW and k each level from 2 to $m - 1$, the population dynamics of each level can be described by the following set of rate equations [71]:

$$\begin{aligned} \frac{dN_m}{dt} = & -\frac{N_m}{\tau_u} - \sum_{i=1}^{m-1} W_i N_m (N_{m-i} + 1) \\ & + \frac{\alpha}{2} N_{m-1}^2 (N_m + 1) (N_{m-2} + 1) \\ & - \frac{\alpha}{2} N_m N_{m-2} (N_{m-1} + 1) \end{aligned} \quad (3.1)$$

$$\begin{aligned} \frac{dN_k}{dt} = & P_k^{(1)}(0) + P_k^{(2)}(\tau_{\text{delay}}) - \frac{N_k}{\tau_p} \\ & + \sum_{i=1}^{m-k} W_i (N_{k+i} (N_k + 1)) - \sum_{i=1}^{k-1} W_i N_k (N_{k-i} + 1) \\ & - \alpha N_k^2 (N_{k+1} + 1) (N_{k-1} + 1) + \alpha N_{k+1} N_{k-1} \\ & \times (N_k + 1)^2 + \frac{\alpha}{2} N_{k+1}^2 (N_k + 1) (N_{k+2} + 1) \\ & - \frac{\alpha}{2} (N_{k+1} + 1)^2 N_k N_{k+2} - \frac{\alpha}{2} N_{k-1}^2 (N_k + 1) \\ & \times (N_{k-2} + 1) + \frac{\alpha}{2} N_{k-2} N_k^2 (N_{k-1} + 1)^2, \\ & k = 2 \dots m - 1 \end{aligned} \quad (3.2)$$

$$\begin{aligned} \frac{dN_1}{dt} = & -\frac{N_1}{\tau_g} + \sum_{i=1}^{m-1} W_i N_{i+1} (N_1 + 1) \\ & + \frac{\alpha}{2} N_2^2 (N_1 + 1) (N_3 + 1) - \frac{\alpha}{2} N_1 N_3 (N_2 + 1)^2 \end{aligned} \quad (3.3)$$

N is the occupation of the level, α describes the exciton-exciton scattering, P is the pumping rate, $-N/\tau$ describe the radiative and non-radiative decay rate of excitons at each level, τ is the decay time of the levels (ground, pumped, and above the pumped level), and W_i is related to the

transition from a level k to a level $k-i$. Phonon-assisted exciton relaxation is taken into account, except for the first level where only the radiative recombination is considered. Transitions between adjacent levels may be mediated by THz emission, as suggested in the proposal [51]. We assume that the pumping is centered at one of the middle levels of the cascade.

Experimentally, the system is excited by fs pulses which are relatively broad in energy and are able to simultaneously pump several energy levels of the cascade. To account such a spectral broadening of the pulse in the theoretical model, we assume that the excitation is possible, not only at the level k , but also at the nearest levels $k-1$ and $k+1$. In the numerical simulations the cascade has 9 levels, with level 6 receiving the major part of pulse power ($2/3$) and levels 5 and 7 receiving the $1/6$ of total input power each.

Figure 3.4 shows the time evolution of exciton densities at each energy level, plotted for zero and -5 ps delay between the pulses. If the system is excited by a single pulse (zero delay, solid lines in Figure 3.4), levels 5–7 are populated and all the other levels are almost empty, for the first ~ 10 ps after the pulse. Due to high exciton density at level 5, the bosonic stimulation from the upper levels 6 and 7 is switched on resulting in a huge population increase of level 5. The population of level 5 reaches its maximum at time ~ 5 ps, while at the same time levels 6 and 7 become empty.

The low energy levels, 4-1, are slowly populated. A critical exciton density value for bosonic stimulation is achieved for level 4 first, due to our model consideration that relaxation between adjacent levels is more efficient. This explains the threshold-like increase of population of level 4 at time ~ 30 ps. Similarly, populations of levels 3 and 2 rapidly increase at time ~ 60 ps and ~ 120 ps, respectively.

However, the population of the lowest level 1 is not efficiently boosted via this pathway due to the low population of the adjacent level 2. Therefore, we have to assume in our model that there is a direct relaxation of excitons from the pumped level 5 to the lowest level. As we will see below, this process explains the second maximum which is experimentally observed in pump-pump experiments shown in Figure 3.3.

Non-radiative losses of excitons, described by terms $-N/\tau$ in rate equations, compete with the relaxation processes. Losses depend on the time spent by excitons at the excited levels. This time can be drastically short-

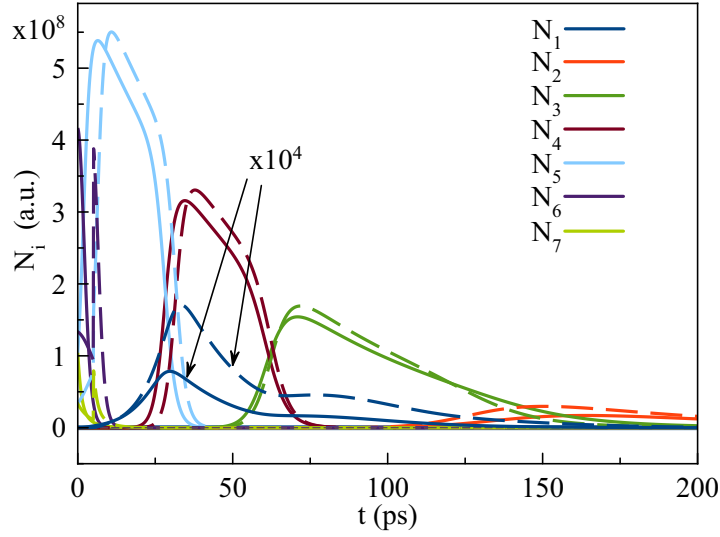


Figure 3.4: Time evolution of exciton densities at each level in the PQW. Solid lines are calculated for zero delay between pulses and dashed lines show the same for a time delay of -5 ps.

ened and, correspondingly, the PL yield can be increased, in the bosonic stimulation regime. Separation of the excitation pulse into two pulses controls the non-radiative losses by controlling the population of different excitonic levels.

Once the excitons created by the first pulse have relaxed to level 5 (it takes about 5 ps), the excitons created by the second pulse which is delayed by 5 ps, rapidly relax from levels 6 and 7 to level 5 via bosonic stimulation. This stimulation gives rise to the increased population of level 5 relative to that obtained for zero delay, as it can be concluded comparing solid and dashed lines of level 5 in Figure 3.4. The corresponding increase of population in the double pulse case is also observed for other levels. In particular, a remarkable increase of population is observed for level 1, which is the key point for understanding of the dip in the delay dependent PL intensity experimentally observed and shown in Figure 3.3 (left).

Figure 3.5 shows the integral of PL intensity I_{PL} , as a function of the delay between pulses for two excitation powers with total power $P^{(1)} + P^{(2)} < P_{th}$, where P_{th} is the lasing threshold. The other curves represent the contribution of each transition term into the total PL. As it can be seen, the theoretical modeling predicts a dip in the PL intensity at delays near zero.

Further increase of the delay time between the pulses gives rise to the depopulation of level 5 when the second pulse arrives. As a result the bosonic stimulation of levels 6 and 7 excited by the second pulse becomes less efficient and the non-radiative losses increase. This explains the decrease of PL intensity at delays 10-40 ps as shown in Figure 3.5 (b). However, when the delay > 40 ps, the population of the ground level is so large that the direct bosonic stimulated relaxation from level 6 becomes an efficient pathway for the exciton relaxation to the ground level. Correspondingly, efficient depopulation of level 6 occurs that results in the decrease of non-radiative losses. These processes explain the appearance of a second peak at the delay dependence of PL intensity. The calculated behaviour of total PL intensities at weak and strong pumping qualitatively reproduce the experimental results shown in Figure 3.3 for the PQW.

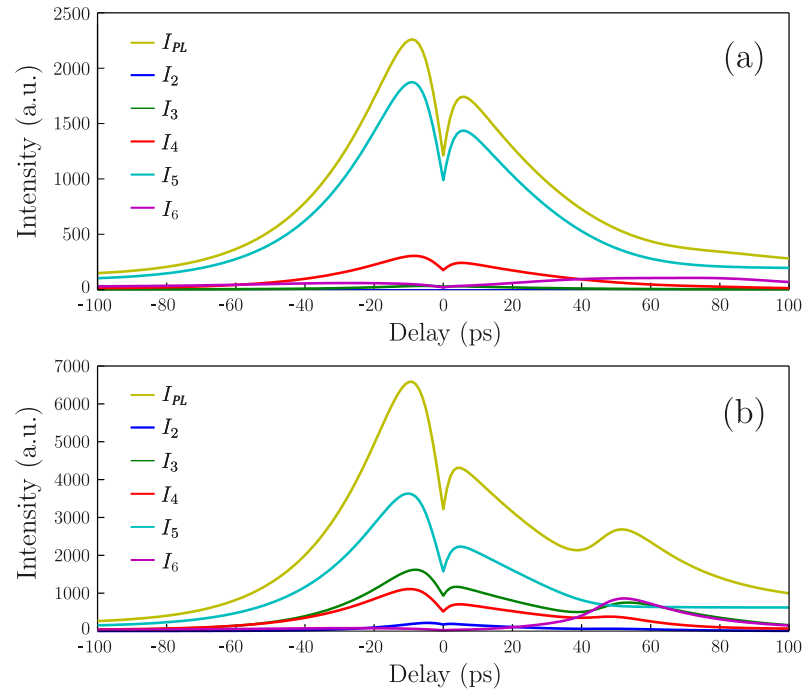


Figure 3.5: Modeling of PL intensity versus the delay time between two pulses. The total PL intensity from the ground level I_{PL} is plotted, along with the separate contribution of each transition, for two different values of pump powers: (a) $P^{(1)} = 0.25P_{th}$, $P^{(2)} = 0.3P_{th}$ and (b) $P^{(1)} = 0.25P_{th}$, $P^{(2)} = 0.7P_{th}$.

3.6 Conclusion

The results presented in this chapter extended our understanding on the exciton dynamics in bosonic cascade systems. We investigated two PQW samples, with and without DBRs and we compared the relaxation dynamics of the PQW MC structure to a conventional MC with rectangular QWs. Strong difference in the relaxation characteristics between the samples was found. We have found a qualitative agreement between the theoretical model and the experimental results. A quantitative agreement was not possible due to the strong non-linearity of the PL on the pump power close to the lasing threshold. The theoretical modeling showed that there are two different pathways for the relaxation of the system. The first pathway is the relaxation via cascade transitions where all levels are being filled, while the second pathway is the direct transition from the pumped level to the ground level. The difference in PL for samples 2 and 3, shown in Figure 3.3, can be explained by including the observation that the PL minimum at zero delay time occurs only in multi-level excitation [71]. The energy levels in a rectangular QW increase with n^2 meaning that high energy levels are separated from each other by a greater distance than low energy levels are, thus excitons are excited only at one energy level. Consequently, multi-level excitation cannot be achieved and there is no minimum at zero time delay in the rectangular QW structure.

Chapter

4

TOWARDS TERAHERTZ EMISSION AND DETECTION

One of the main objectives of the project is to investigate the possibility of generating THz radiation in semiconductor [MCs](#). For that reason, we need an experimental setup able to generate and detect THz light. In general, a fundamental limitation preventing the realization of a reliable solid state THz source, is the low spontaneous emission rate of THz photons. The spontaneous emission time of a THz photon typically is in the ms range, while the lifetime of photo-excited carriers and crystal excitations typically is in the ps range. The spontaneous emission rate can be increased either by placing the emitter in a THz cavity or by using the cascade effect in [QCLs](#) [60, 73, 74]. In the last decade, it was proposed that the rate can be additionally increased by the phenomenon of bosonic stimulation, if a radiative transition occurs into a condensate state [51, 60, 73]. To investigate this amplification of spontaneous emission and THz radiation we developed a [THz-TDS](#) system described in Appendix [A.5](#). This chapter presents the basic methodology and preliminary results from the first evaluation and testing.

4.1 The basics

There are two main experimental regimes [75], [THz-TDS](#) and optical pump THz probe ([OPTP](#)) spectroscopy (which is also considered a [THz-TDS](#) technique as it is an extension of it). These two regimes measure the transmission of the THz waves (which is directly related to the electrical conductivity) at carrier equilibrium and in photo-excited state, respectively. In the [THz-TDS](#) experiment, the sample is probed with a THz pulse with electric field $E(t)$ as a function of time. The THz pulse $E_s(t)$ is transmitted through the sample, therefore it is delayed and its intensity is decreased due to absorption. A Fourier transform is applied to every $E(t)$ to obtain the corresponding frequency domain $E(\omega)$ of the pulse. The transmission

function in the frequency domain is given by the ratio

$$T(\omega) = \frac{E_s(\omega)}{E_{ref}(\omega)}. \quad (4.1)$$

In the **OPTP** technique [76], the sample is probed with a THz electric field $E(t)$, similar to the **THz-TDS** case, while at the same time it is photo-excited by an optical pump pulse. As already mentioned, the photo-excitation of charged carriers increases the electrical conductivity, and thus, decreases the transmission of the THz probe pulse. The difference between the transmitted THz pulses with and without photo-excitation is defined as

$$\Delta E(t) = E_s^{ON}(t) - E_s^{OFF}(t), \quad (4.2)$$

where $E_s^{ON}(t)$ is the electric field of the THz pulse in the excited regime of the sample and $E_s^{OFF}(t)$ in the unexcited regime. A term that is typically used is the $\Delta T/T$, which is the change in transmission due to photo-excitation, and can be calculated by

$$\frac{\Delta T(\omega)}{T(\omega)} = \frac{\Delta E(\omega)}{E(\omega)} = \frac{E_s^{ON}(\omega) - E_s^{OFF}(\omega)}{E_s^{OFF}(\omega)}. \quad (4.3)$$

The **OPTP** setup is able to measure two different kinds of data, photo-conductivity spectra and photoconductivity decays, depending on which delay stage is scanned. A photoconductivity spectrum can be obtained when the THz probe delay stage is scanned, while a photoconductivity decay can be obtained when the pump delay stage is scanned and the probe delay is fixed at the peak of the THz pulse. It should be noted that, to extract conductivity σ from $T(\omega)$ on the **THz-TDS** method and $\Delta\sigma$ from $\Delta(T\omega)/T(\omega)$ on the **OPTP** method, requires consideration of many parameters, such as the sample geometry and the wave propagation through the sample.

The chopped pump pulse modulates the sample between the photo-excited and unexcited regime, therefore, the transmitted THz pulse is modulated between the $E_s^{ON}(t)$ and $E_s^{OFF}(t)$ state. As mentioned in Section A.5, the **OPTP** setup is based on double lock-in detection. The first lock-in amplifier measures the average of $E_s^{ON}(t)$ and $E_s^{OFF}(t)$, which is

$$\frac{1}{2}(E_s^{ON}(t) + E_s^{OFF}(t)), \quad (4.4)$$

while the second measures the difference $\Delta E(t)$ (shown in Equation 4.2). Using Equation 4.2, the average becomes equal to

$$\frac{\Delta E(t)}{2} + E_s^{OFF}(t). \quad (4.5)$$

Generally, the difference is much smaller than the electric field, $\Delta E(t) \ll E_s^{OFF}(t)$, therefore, it can be considered that the first amplifier measures the $E_s^{OFF}(t)$, which is needed for the calculation of $\Delta T(\omega)/T(\omega)$. A typical way to present OPTP spectrum and decay data is by plotting $\Delta E(t)$ versus the appropriate time delay t . In addition, if many scans of both kinds of measurements are combined, a 2-Dimensional graph can be produced, having the two different delay times in x and y axes and $\Delta E(t)$ in the z axis.

Furthermore, by fitting a single or double exponential to the THz decay curve (OPTP pump scan), the decay time constants (or carrier lifetimes) can be obtained. The equations of the exponential fits are

$$f(x) = y_0 + Ae^{-(x-x_0)/\tau} \quad (4.6)$$

for the single exponential, and

$$f(x) = y_0 + A_1 e^{-(x-x_0)/\tau_1} + A_2 e^{-(x-x_0)/\tau_2} \quad (4.7)$$

for the double exponential, where x_0 , y_0 are the offsets and A , A_1 , A_2 are the amplitudes of the exponential terms, corresponding to the carrier populations which decayed with τ , τ_1 , and τ_2 lifetimes [77].

THz waves are absorbed from polar molecules, such as water [36], therefore, it is better to perform measurements in a low humidity environment. Usually, THz-TDS setups are enclosed in a box and atmospheric air is replaced to reduce the humidity level. In our setup, a constant flow of gas nitrogen is used to replace air and eliminate the absorption peaks of water. Figure 4.1 shows the effect of nitrogen in the experimental THz measurement, both in time and frequency domain. 30 minutes of constant flow is enough time to eliminate the water absorption peaks.

Sometimes, to improve the accuracy of the amplitudes of a Fourier transform of a signal, a technique called zero padding is used. Zero padding is the process of adding zeros to the end of a time domain signal to increase its length. The technique is also used in specific Fourier transform algorithms which require input data with a power of 2 length, so it is applied to fill the missing points. When zero padding is applied to a signal,

the resulted frequency domain appears interpolated with higher number of points compared to a non-padded signal. However, there is a misconception whether zero padding increases the frequency resolution or not and it's happening due to different definitions of the term resolution. After all, it is important to understand that zero padding may reveal, but cannot create, useful information about the initial signal. The effect of zero padding to our data is shown in Figure 4.2, where the amplitude of the absorption lines of water is increased.

When a double lock-in detection is used (OPTP), the two amplifiers are serially connected and they need two reference frequencies. Usually, one of them has a high frequency (f_{1h}) and the other one a low (f_{2l}), with low and high time constants respectively (τ_{1l} , τ_{2h}). To make the double lock-in detection work [34], the following relationship should be satisfied

$$f_{1h} \gg \frac{1}{\tau_{1l}} \gg f_{2l} \gg \frac{1}{\tau_{2h}}. \quad (4.8)$$

Most of our results were taken using the values shown in Table 4.1. As you will probably realize, there are many parameters to consider when choosing the appropriate values. Begin with the values of Table 4.1 and then, adjust them accordingly, trying to reveal and measure the signal in a reasonable time duration of the experiment.

Lock-in	Frequency	Time constant
1	42 kHz	640 μ s
2	56 Hz, 73 Hz	3 sec, 2 sec

Table 4.1: Values used in the lock-in amplifiers.

Note that the highest time constant determines the duration of the experiment. Typically, three times the time constant is enough time for each point of the scan to be measured. The lowest time constant τ_{1l} is also important. We need a low value to achieve a high frequency and increase the frequency distance from f_{2l} . By increasing the frequency distance from $\frac{1}{\tau_{1l}}$ to f_{2l} , we also decrease the corresponding distance from f_{1h} to $\frac{1}{\tau_{1l}}$, although, this is not so crucial because we can easily increase the first frequency from the function generator and maintain a big difference between them. Equation 4.9 shows the result of a combination of Equation 4.8 and Table 4.1.

$$42 \text{ kHz} \gg \sim 1.5 \text{ kHz} \gg 56 \text{ Hz} \gg 0.33 \text{ Hz} \quad (4.9)$$

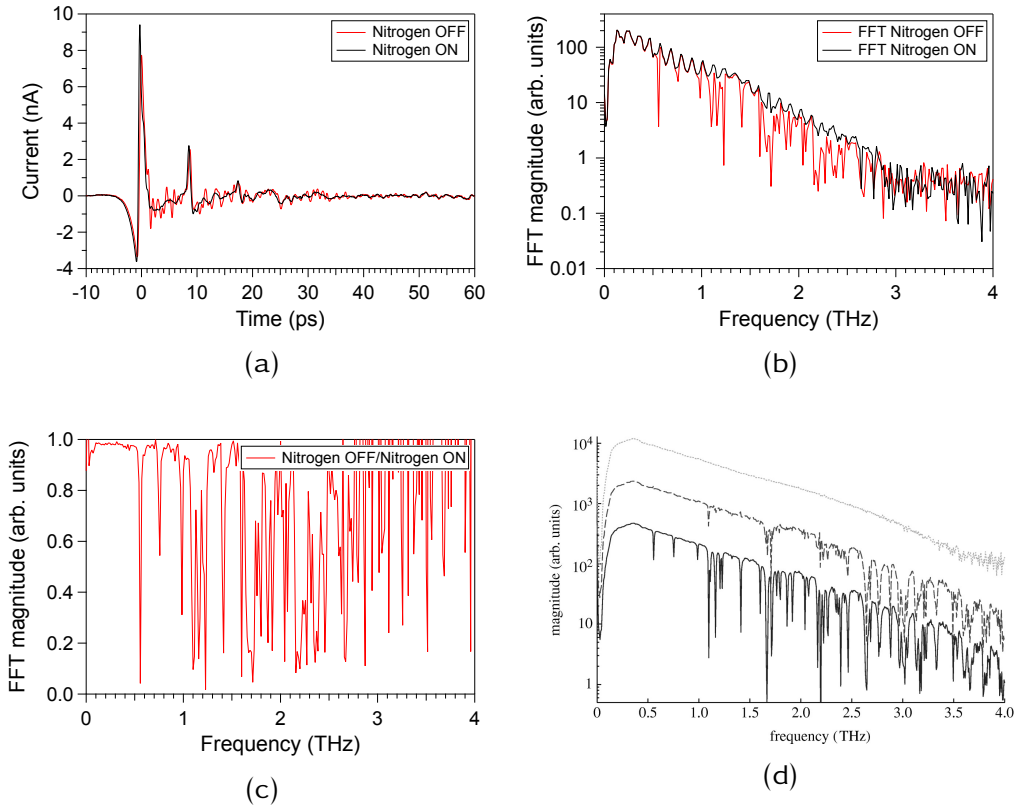


Figure 4.1: The effect of gas nitrogen to THz waves in our THz-TDS system. (a) The THz pulse in the time domain (THz-TDS probe scan) and (b) the corresponding Fourier transform in the frequency domain. The second peak that appears in our THz-TDS probe scans can be attributed to reflections in the THz path. (c) The absorption lines of water. (d) Data from [78] for comparison, solid line is in water vapour atmosphere.

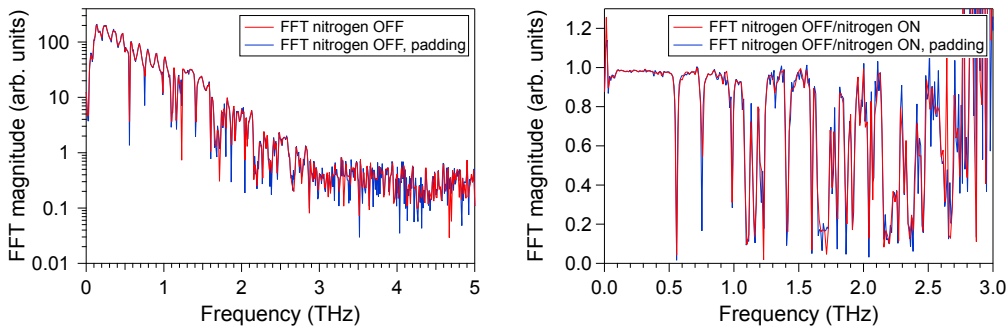


Figure 4.2: The effect of zero padding to the water absorption lines in the Fourier transform of a THz-TDS signal.

It should be noted that, for the cryostat's windows we use either Sapphire or Quartz, which are transparent in both THz and visible regions with a transmission of $\sim 50\text{-}70\%$. However, organic materials like TPX (polymethylpentene), PE (polyethylene), and PP (polypropylene), have higher transmission than crystalline materials, $\sim 80\text{-}90\%$, with TPX being the best alternative to our existing setup.

To perform **OPTP** measurements, the appropriate pump delay time should be found. A sample able to easily emit THz pulses upon laser irradiation, such as **LT-GaAs**, can be used [77]. First, two **THz-TDS** probe scans are performed to find the delayed THz signal through the sample, as shown in Figure 4.3 (a). Then, to find the pump delay time, a **THz-TDS** pump scan is performed, as shown in Figure 4.3 (b).

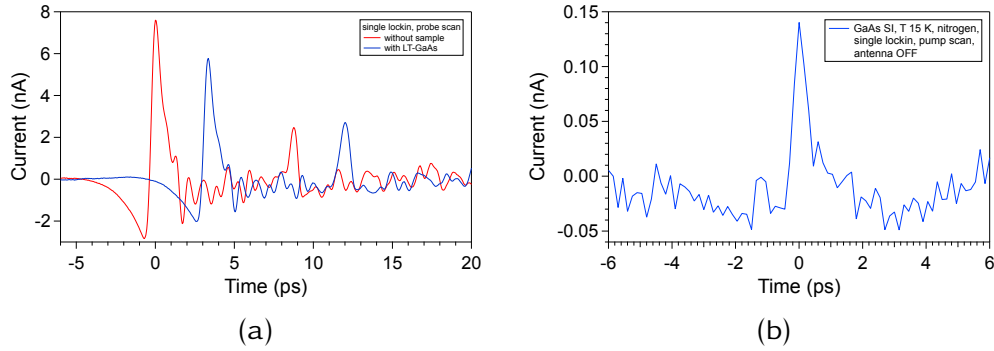


Figure 4.3: (a) **THz-TDS** probe scans reveal the delayed THz peak. (b) **THz-TDS** pump scan to measure the THz emission from the sample and find the pump delay time.

Another important step is to find a good spatial overlap between the THz beam passing through the sample and the pump laser beam exciting the sample (Figure 4.4). To achieve that, it is crucial to use a sample with a high carrier lifetime, such as high resistivity Silicon (**Si HR**). First, the delayed THz wave that travels through the sample is found, as shown in Figure 4.5 (a), and then, the effect of the pump laser at the THz peak is observed (pump OFF/ON), as shown in Figure 4.5 (b) and (c). Additionally, it is necessary to avoid focusing the pump beam because the pump spot size should be larger than the THz spot size. This ensures a uniform photo-excited carrier density over the area probed by the THz pulse [75, 79].

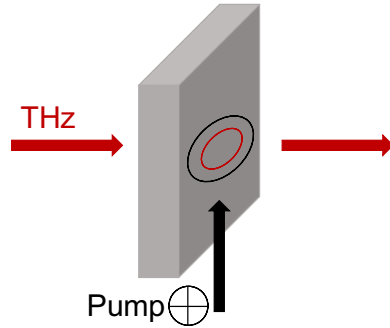


Figure 4.4: Schematic showing the orientation of the sample and the THz, pump beams. For a uniform photo-excited carrier density over the probed area, the pump spot size should be larger than the THz spot size.

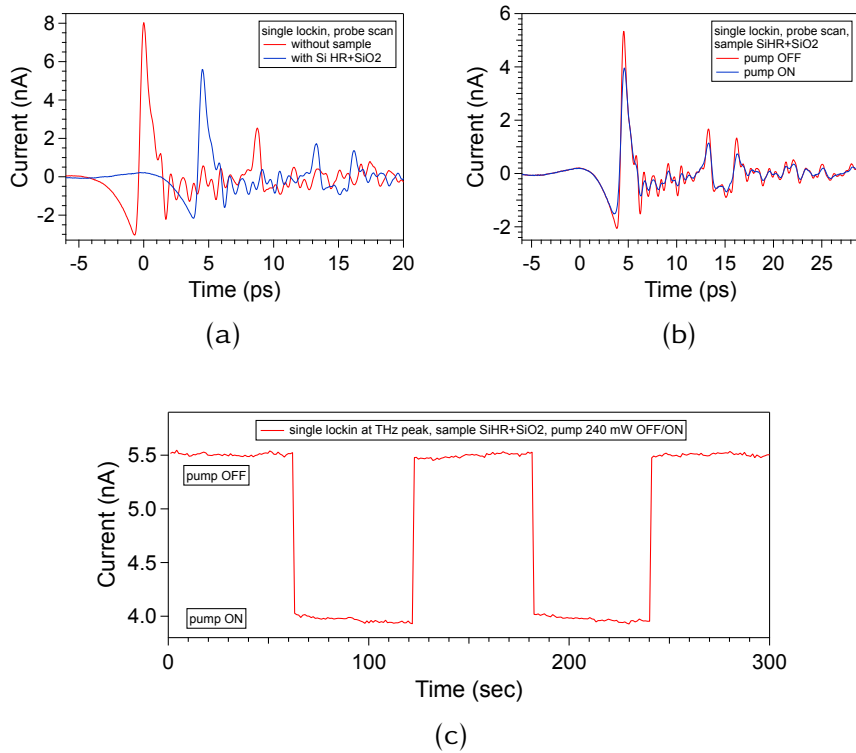


Figure 4.5: **Si HR** is used to find the overlap between the THz beam passing through the sample and the pump laser beam exciting the sample. (a) The delayed THz signal from the sample. (b), (c) The effect of the pump laser beam to the transmitted THz signal from the sample.

In general, repeating a scan multiple times and averaging a series of signals results in reduced random noise. Averaging is effective in the time domain, but not in the frequency domain when a non-linear operator, such as an absolute (when the magnitude of the Fourier transform is displayed), is applied [80, 81]. Decreasing the scan step can reveal the signal fluctuations, thus, a good combination of a relatively small step with a number of repeated measurements should be found. It should be noted that, as the scan step is reduced, the time needed for a single scan of the same total length is increased. Figure 4.6 shows the effect of averaging a number of repeated **OPTP** pump measurements for a 0.5 ps step.

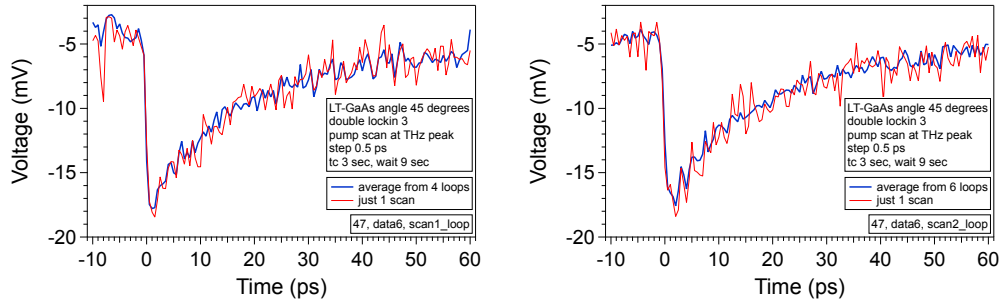


Figure 4.6: Averaging a number of repeated measurements reduces the noise. Comparison of one scan and an average of four scans (left) and six scans (right).

4.2 Results

As previously mentioned, the **THz-TDS** technique can be used to measure the absorption of molecules, such as the water absorption shown in Figure 4.1. It is also used to measure free carrier absorption. We will use a **LT-GaAs** sample to demonstrate such a measurement.

OPTP pump scans at the THz peak of a **LT-GaAs** sample were performed. The sample was placed at a 45 degrees angle to the surface normal and different delay steps and number of repeats (loops) were tried. The probe delay was fixed at the THz peak and the modulation of this peak is studied by scanning the pump delay. First, upon carrier injection, a fast reduction of the THz signal is observed, and then, the signal recovers exponentially near its initial value. The photo-excitation of the sample modifies the probe THz pulses generated from the antenna, by THz absorption.

THz absorption is related to conductivity, therefore, it provides carrier information. It should be noted that, to generate enough carriers, the pump source should be a powerful fs laser system [77].

Figure 4.7 shows the THz decay curves and the corresponding single exponential fittings for a **LT-GaAs** sample. The obtained decay time constant is approximately 16 ps. In addition, it should be noted that, the lower the temperature of the growth of **LT-GaAs**, the shorter the carrier lifetime of the sample. Defects due to the non stoichiometric growth of **GaAs** at low substrate temperature, act as carrier traps [77, 82] and decrease their lifetime. Our sample was grown at ~ 300 K. Faster time decays are usually observed in samples grown at temperature ~ 180 -250 K.

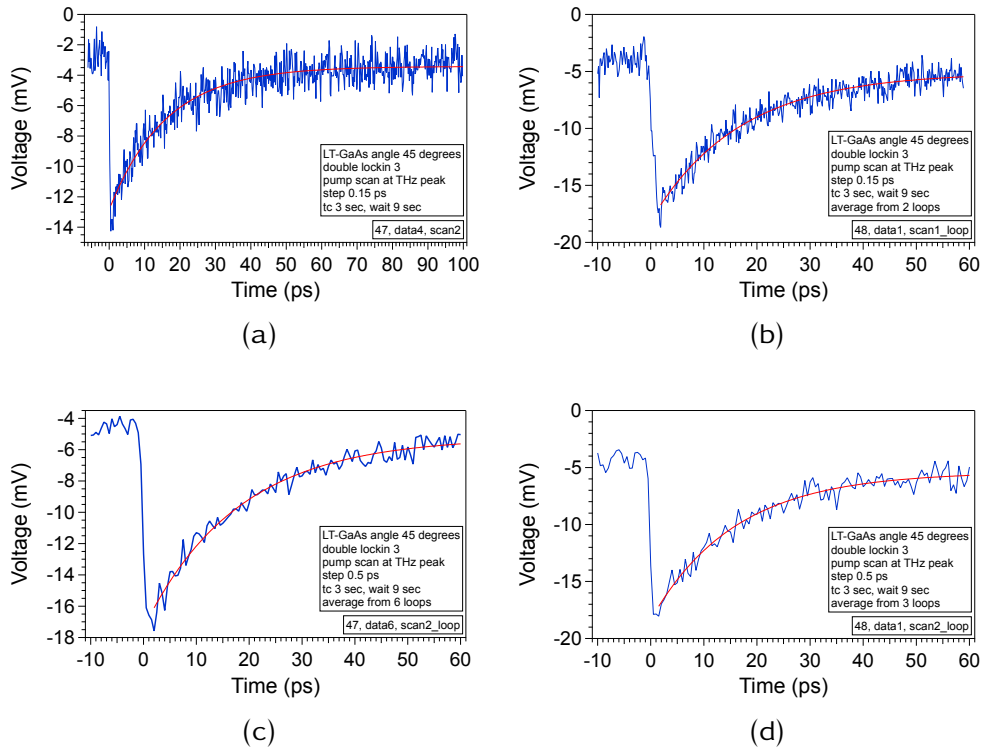


Figure 4.7: **OPTP** pump scans at the THz peak of **LT-GaAs**. In all cases the sample is at 45 degrees angle to the incident pump beam. The exponential fit is shown in red. Decay time constants are: (a) $\tau = 16$ ps, (b) $\tau = 16.6$ ps, (c) $\tau = 17.8$ ps, (d) $\tau = 15.8$ ps.

To provide more evidence that the measured signal is the effect of the pump beam to the THz pulse that passes through the sample, we performed 3 different scans, as shown in Figure 4.8. The signal is zero when either the antenna or the pump beam is disabled.

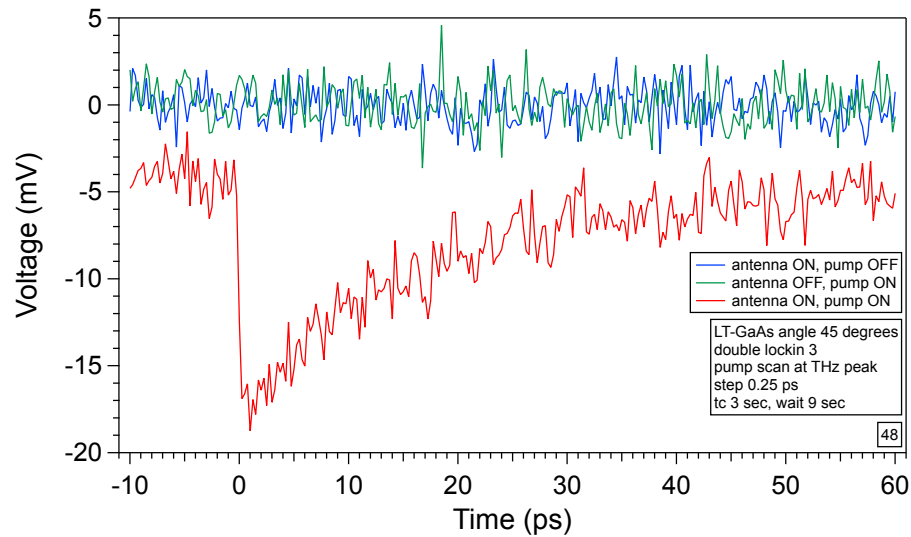


Figure 4.8: **OPTP** pump scans at the THz peak of a **LT-GaAs** sample. Three different cases with antenna/pump ON/OFF as shown in the annotation. The sample is at 45 degrees angle to the incident pump beam. The measurement is detectable only when both the generation antenna and the pump laser are enabled.

In Figures 4.9 and 4.10, a preliminary two dimensional analysis is shown. First, a **THz-TDS** probe scan is presented which shows the different probe delays for the pump scans. Then, all of them are plotted in the following two graphs. The emission starts with a low amplitude for negative pump delay times, then rises up to a maximum amplitude at pump delay = 0 ps, and then slowly decays for positive pump delay times. The same process was repeated one more time. In Figure 4.9 every data file is one scan, while in Figure 4.10 every data file is a loop of 3 scans, and that's why the last appears smoother. Consequently, from a 2-D graph, both the **OPTP** pump and probe scans can be extracted by taking slices at fixed delays.

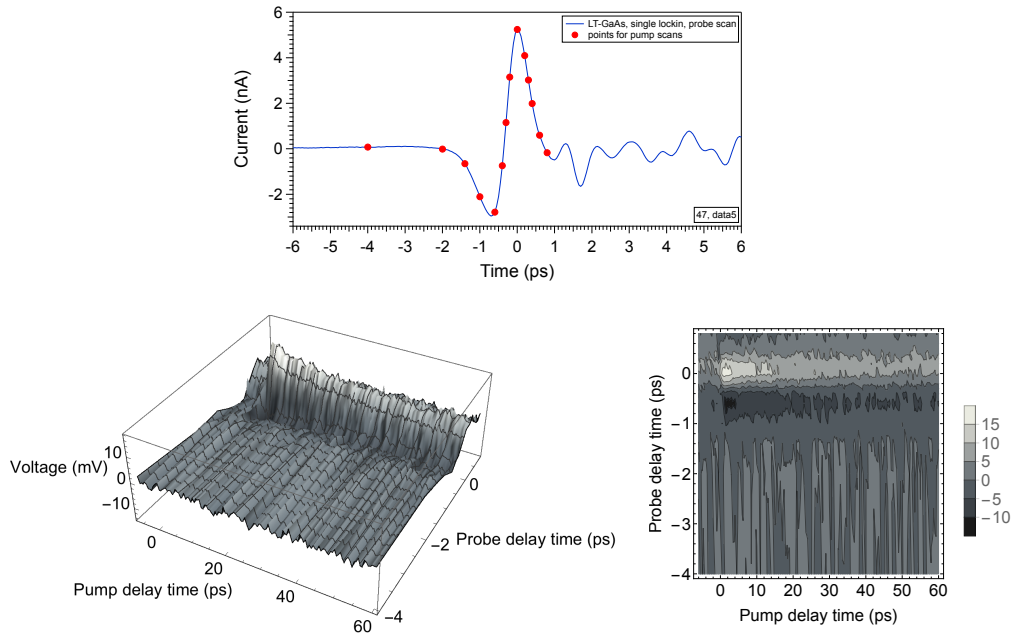


Figure 4.9: A 2D representation of the photo-induced change in THz transmission $\Delta E(t)$ in **LT-GaAs**. Red points in a **THz-TDS** probe scan show the positions of the pump scans. Then, a 2D graph and a contour plot from the same data show all the **OPTP** pump scans for the different probe delays.

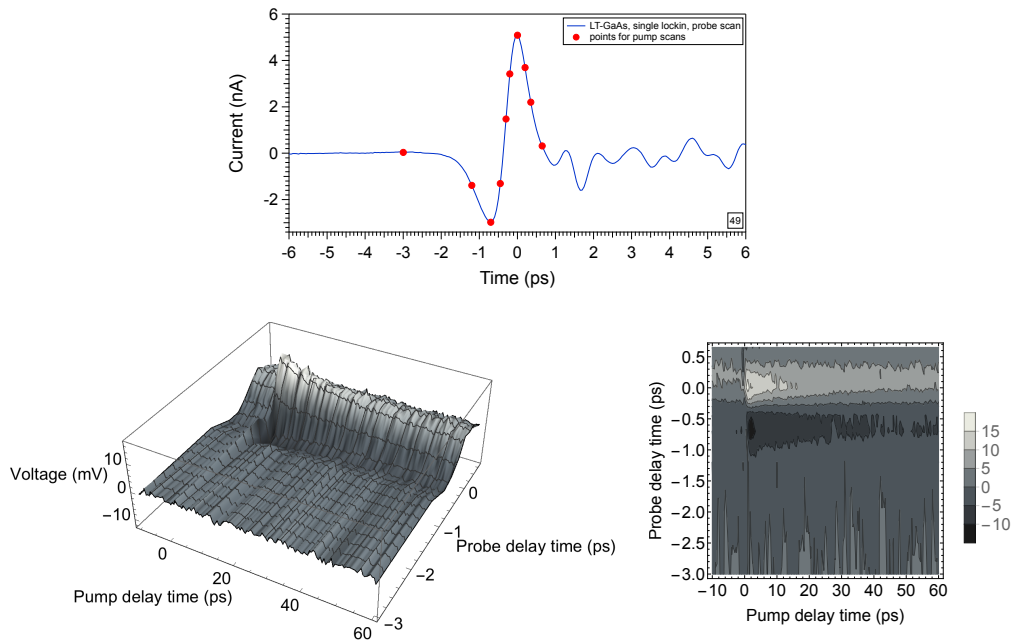


Figure 4.10: Repeat of measurements presented in Figure 4.9, but here every measurement is an average of 3 scans.

Our next step was to design and test a new structure based on the concept of PQWs. It's a MC structure with 4 embedded InGaAs PQWs, on a SI GaAs substrate. The parabolic potential is achieved by varying Indium concentration from 0 to 4%, along the growth direction. The DBRs are alternate layers of GaAs and AlAs, with 29 periods for the bottom and 25 for the top. The complete structure is shown in Figure 4.11.

s496

9	GaAs 588.3 Å	x25
8	AlAs 695.2 Å	
7	GaAs 1000.2 Å	
6	InGaAs PARABOLIC 0-4-0 400 Å	x4
5	GaAs 760 Å	
4	GaAs 240.2 Å	
3	AlAs 695.2 Å	x29
2	GaAs 588.3 Å	
1	GaAs buffer	
SI GaAs(100) substrate		

Figure 4.11: The MC structure with four PQWs.

A sample like this is expected to provide a THz gain due to the cascade phenomenon. We externally pump the sample, so a THz emission from the semiconductor itself will be emitted. To decouple the sample's THz generation from the measured signal, we use the double lock-in detection of the OPTP method.

In summary, first, the THz-TDS probe scan is checked to measure the THz radiation that passes through the sample. Then, the ability of THz emission from the sample is evaluated along with the effect of the pump beam to the THz probe peak. Finally, the OPTP technique is employed to photo-excite the carriers and perform both pump and probe scans to measure the change in transmission, both the decay at the THz peak and the entire THz waveform.

The sample generates and emits THz radiation, as shown in Figure 4.12 (a), where a THz-TDS pump scan is presented. Then, a THz-TDS probe scan (Figure 4.12 (b)) shows the THz beam that passes through the sam-

ple. It should be noted that these measurements are at low temperature ($T = 15$ K), so the signal is low due to the intensity reduction from the cryostat's windows. In Figure 4.12 (b) there are two scans, without and with the optical pump beam. If there is a difference, it's a small one, so a more careful measurement should be done. To examine it, we fix the delay at the specific peak and let the pump beam ON and OFF. Figure 4.12 (c) shows the results. The pump pulses reduce the intensity in a tiny but observable amount. It is difficult to observe the difference in the scans of Figure 4.12 (b) and there is no difference in the corresponding Fourier transforms¹ shown in Figure 4.12 (d).

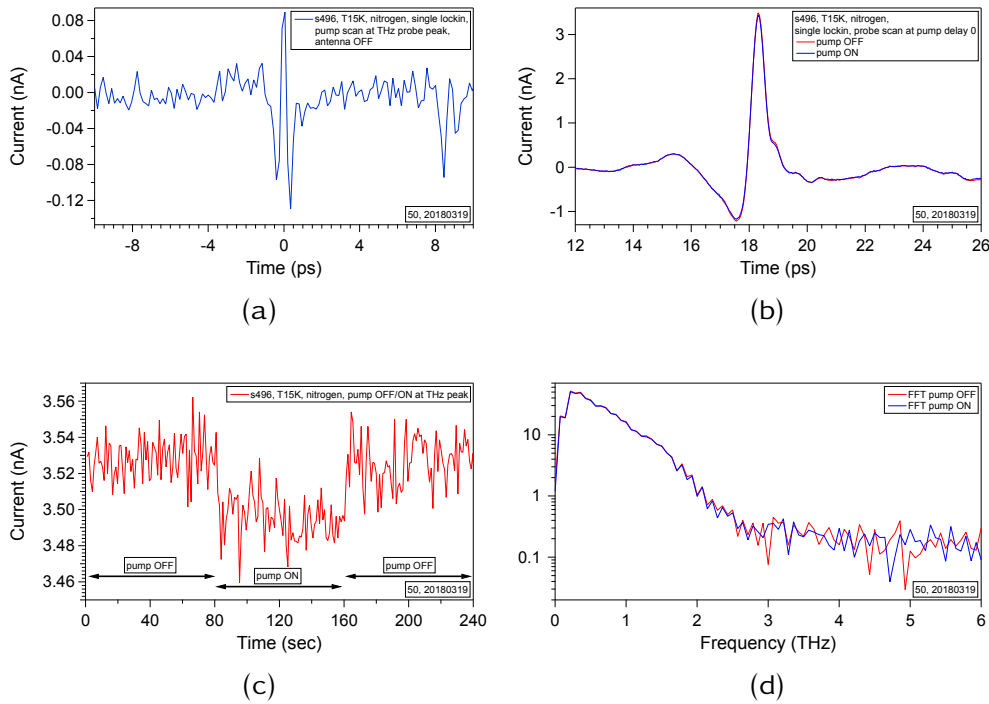


Figure 4.12: Sample 496 at 15 K. (a) THz-TDS pump scan. (b) THz-TDS probe scan with/without the pump laser and (d) the corresponding Fourier transforms. (c) The effect of the pump beam to the THz peak.

To continue, we repeat the OPTP measurement previously presented. In Figure 4.13 (a), it is shown that carriers in the new sample seem to be unable to decay and the absorption remains constant, contrary to LT-GaAs where they decay as shown on the same graph for comparison. The mea-

¹For the Igor Pro code of the Fourier transform see Appendix B.5.

surement is again the same, the pump delay is scanned and the probe delay is fixed at the THz peak.

An **OPTP** probe scan is shown in Figure 4.13 (b). It shows three scans at low temperature with antenna/pump ON/OFF as noted in the annotation. As already mentioned, the signal is only measured when both the generation antenna and the pump beam are enabled.

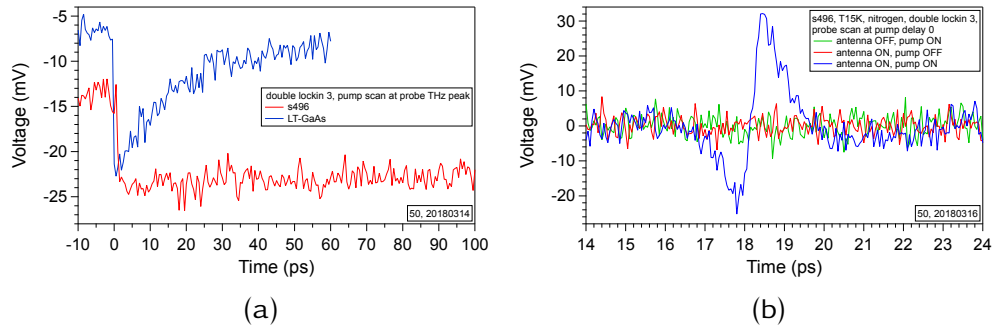


Figure 4.13: **OPTP** measurements on s496. (a) Pump scan at THz probe peak for s496 and **LT-GaAs** for comparison. (b) Probe scans at low temperature (15 K) for three different combinations of the antenna and the pump beam.

We believe that the **OPTP** probe scan of the **MC** sample in Figure 4.13 is related to absorption, not gain. It is not obvious from just the **OPTP** probe scan if the measurement is absorption or gain. An initial signal, such as the black one in Figure 4.14 (a), undergoes an intensity reduction when it's absorbed and an intensity increase when it's amplified. The differences between the two signals (black minus red/blue), for the two cases, are shown in Figure 4.14 (b). The main difference is which increases first and which second. As it can be seen, the red starts, decreases and then increases, while the blue does the opposite. The red is related to absorption while the blue to gain. We compare this behaviour to our results.

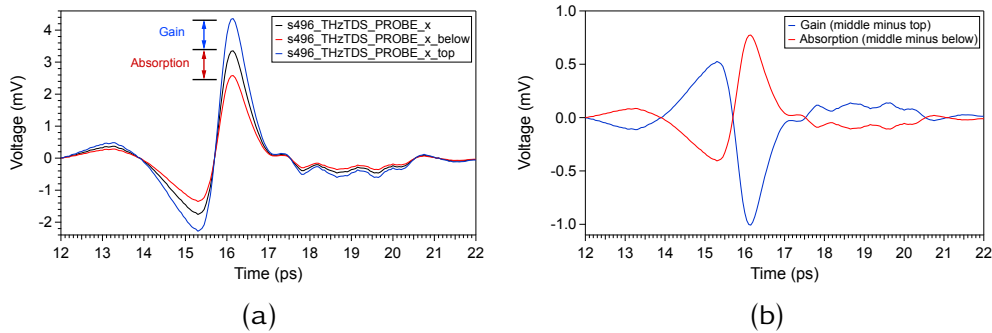


Figure 4.14: A representation of absorption and gain. (a) When a signal is absorbed, its intensity decreases (black to red), while when a signal is amplified, its intensity increases. (b) The corresponding difference.

To provide more information, we compare the response of known samples that exhibit absorption (such as [Si HR](#)) to the [MC](#) sample. In [Figure 4.15](#) we show the [THz-TDS](#) and the [OPTP](#) scans for two samples, the [Si HR](#) and the [MC](#) sample (s496). In addition to the x value of the lock-in amplifier which is commonly presented, we also show the y and r values accompanied with the corresponding phase. The phase is shown to ensure that it's zero near the main THz peak and remains zero when the sample under study is changed from the [Si HR](#) to the [MC](#) one. The measurements are at low temperature (40 K) and the box is purged with gas nitrogen. Three samples ([Si HR](#), [LT-GaAs](#), and s496) are glued with silver paint to the specially designed copper mount inside the cryostat, at 45 degrees angle to the surface normal. As already discussed, [Si HR](#) is used for the overlap between the optical and the THz pulse and [LT-GaAs](#) for the estimation of the zero pump delay.

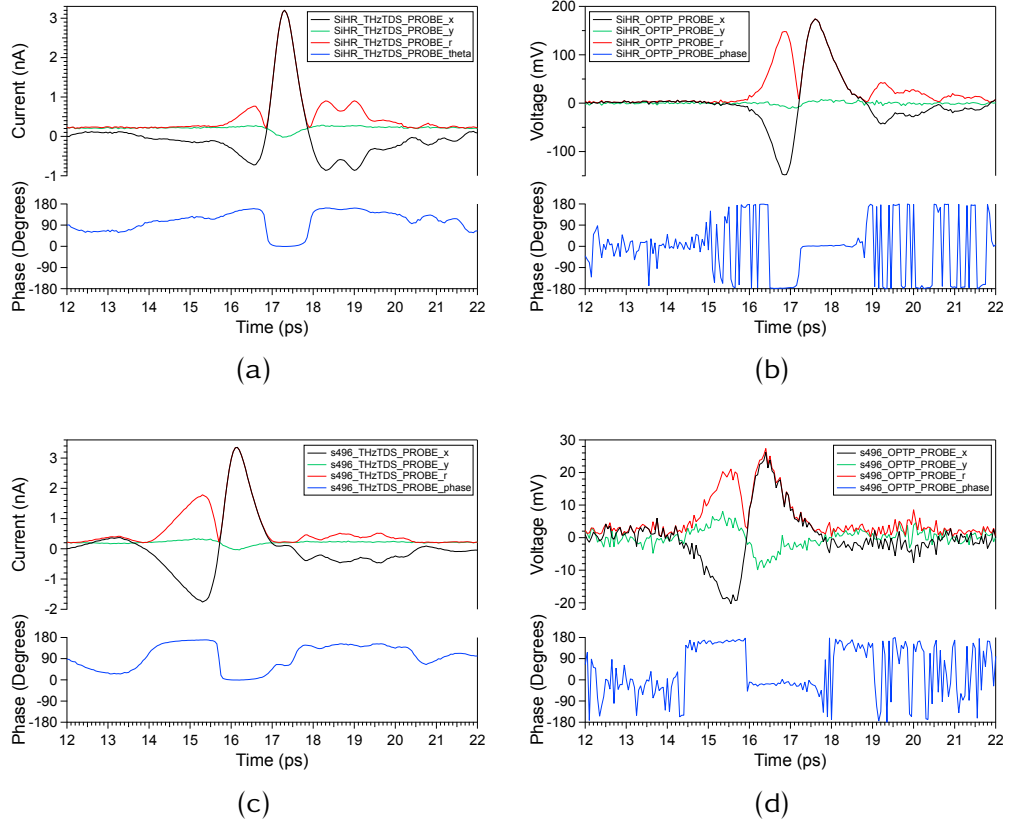


Figure 4.15: THz-TDS and OPTP scans for two samples, Si HR and s496, at low temperature (40 K), showing all the available lock-in amplifier measurements, x, y, r, and phase. (a) THz-TDS of Si HR, (b) OPTP of Si HR, (c) THz-TDS of s496, (d) OPTP of s496.

In the above configuration with three samples inside the cryostat, we can move the position of the cryostat to select a specific sample. After finding the zero pump delay time from the THz emission of LT-GaAs, we select the Si HR sample and perform an OPTP pump scan at its THz peak. We expect to observe a step change near the zero pump delay time, as presented in Figure 4.16. Si HR has high carrier lifetime, therefore we observe a constant change which will not return to its initial value in the timescale of the experiment (some ps). The phase at the THz peak is zero and constant during the OPTP pump scan. It's also possible to quantify the change in terms of the percentage of absorption, as it can be seen in the right axis of Figure 4.16. By knowing the absorption change of the sample when it is optically pumped, such as the one measured with single lock-in detection in Figure 4.5 (c) and Figure 4.12 (c), we can assign it to the initial absorp-

tion that is displayed in the negative delay time of Figure 4.16. As it can be seen in Figure 4.16, the additional change is 2% (from 30% to 32%) and it is clear that the technique is able to measure even smaller changes.

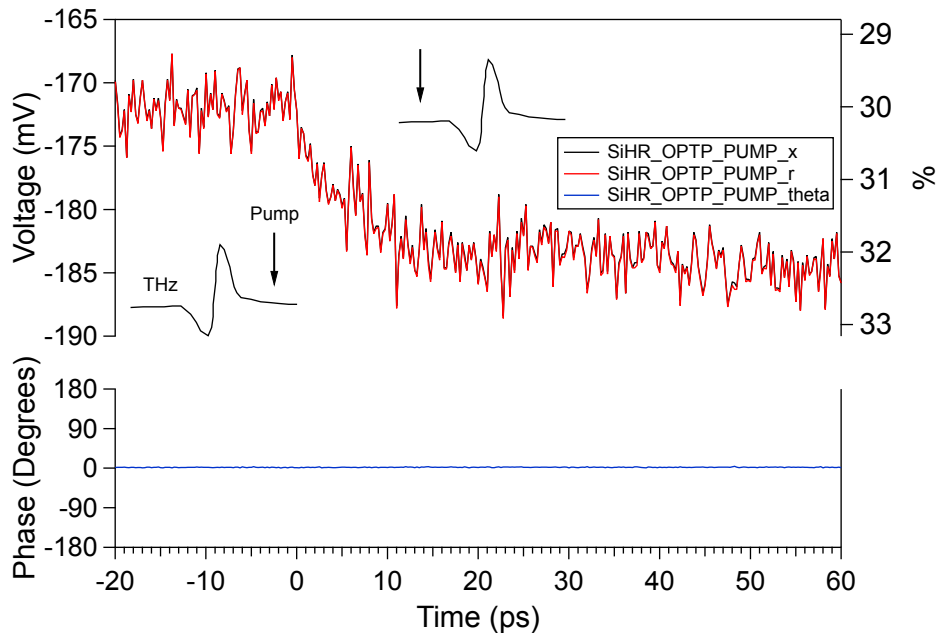


Figure 4.16: **OPTP** pump scan of **Si HR**. The zero pump delay has already been found from a **THz-TDS** pump scan measurement of **LT-GaAs**. Negative time means that the pump pulse comes after the THz pulse, while positive time means the opposite, as shown in the schematic.

The histogram of the **OPTP** pump scan of **Si HR** is presented in Figure 4.17. A Gaussian fit for each absorption state is applied to provide a clearer view. The standard deviation σ of the fit is 1.15 mV for the first peak and 0.84 mV for the second peak, while the separation between the maximum of the peaks is 11.7 mV. The FWHM is 3.81 mV for the first peak and 2.78 mV for the second peak, corresponding to a percentage difference of 0.52% and 0.38% respectively, as shown in the annotation.

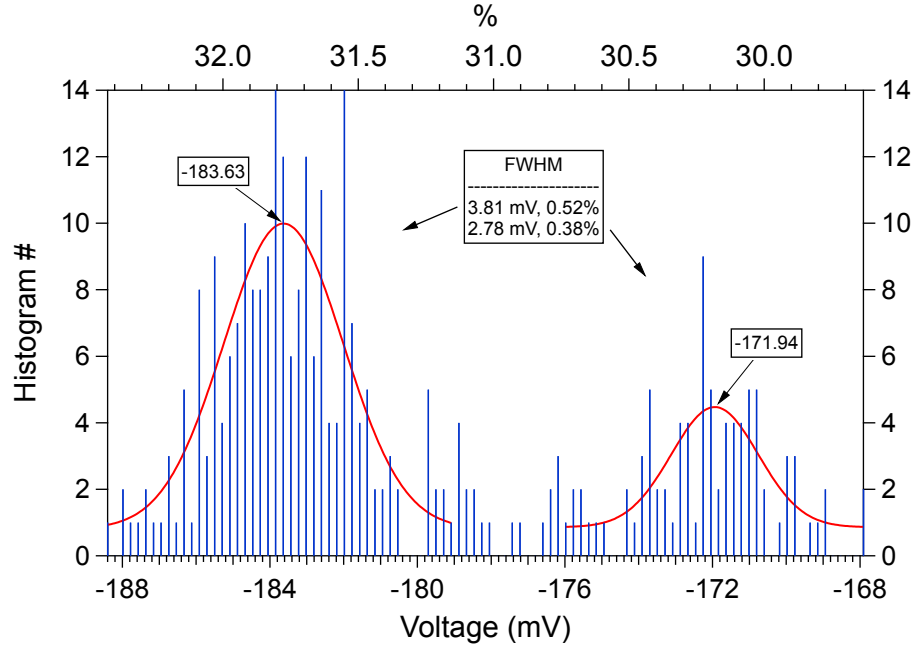


Figure 4.17: Histogram of the OPTP pump scan of Si HR showed in Figure 4.16.

Another step is to rotate the MC sample at 90 degrees angle to the THz pulse. In this orientation, not just a projection of the emission, but the whole possible amplification can be measured. This is due to the theoretical proposal's suggestion that the emission from this kind of structures is from their sides. Therefore, the sample should be appropriately placed in the specific angle. This wasn't achieved till the writing of the present thesis and it's a subject of ongoing investigation.

If a link to physical parameters is needed, a suitable method to extract the conductivity σ and $\Delta\sigma$ from the measured transmission function T and $\Delta T/T$ should be applied². Physical parameters such as charge carrier scattering rate, may be obtained by fitting the spectra with physical models, such as the Drude model [75]. The Drude model is a classical model for the conductivity $\sigma(\omega)$ of metals and semiconductors and describes the motion of charge carriers under an alternating electric field. It connects the conductivity with parameters such as the charge carriers scattering rate, density, and mobility [75]. Many systems are complex

²THz-TDS and OPTP techniques provide the frequency dependent conductivity spectra $\sigma(\omega)$ and the photoconductivity spectra $\Delta\sigma(\omega)$, respectively.

and deviate from the standard Drude model, therefore, there are extensions of the Drude model aimed to describe specific systems (such as the Drude-Smith model for nanowires).

4.3 Conclusion

The THz-TDS experimental setup was successfully realized. Preliminary results presented a general idea of the important aspects of the measurements. A very careful alignment is crucial and more experiments are needed to fully explore the samples in the bosonic cascade regime. Theoretical proposals suggest that the THz radiation from this kind of structures is emitted from their sides. In our first attempts, the sample was placed in a 45 degrees orientation as shown in Figure 4.18 (left). It was a necessary step to better understand the basic principles of the experiments. To be able to measure the entire THz emission, the sample should be placed at 90 degrees angle to the THz pulse as shown in Figure 4.18 (right). This wasn't achieved till the writing of the present thesis and it's a subject of ongoing research. In our configuration, we compared the signal of Si HR, which we know that exhibits absorption, to the MC sample. We observe a similar behaviour and we conclude that the response of the MC structure is related to absorption, not gain.

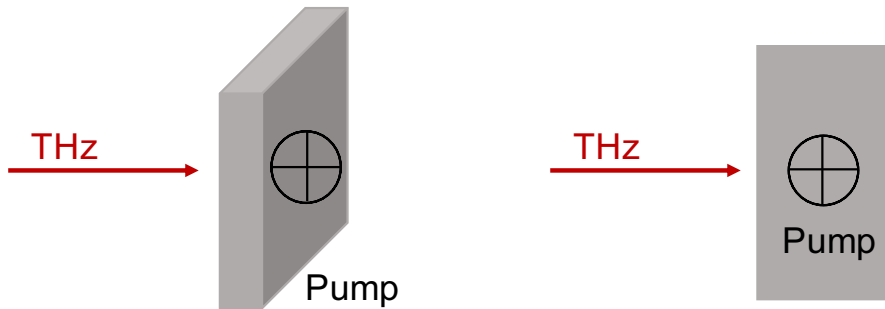


Figure 4.18: Orientation of the sample in the OPTP technique. At 45 degrees angle to the surface normal (left) and at 0 degrees angle to the surface normal (right).

Chapter 5

OVERVIEW AND FINAL THOUGHTS

The work presented in this dissertation was focused on two goals with a common ultimate purpose; the cascade THz emission from polaritonic structures. The main idea was based on the concept of the [BCL](#) which uses the equally spaced excitonic levels of a [PQW](#) and the phenomenon of bosonic stimulation to generate and improve THz emission.

The first goal was the study of semiconductor [MC](#) structures utilizing a [PQW](#), capable of supporting stimulated cascaded relaxation [83]. It was shown that the [PQW](#) exhibits almost-equally spaced excitonic transitions and we observed quantum beating at THz frequencies between specific levels. The [MC](#) structure showed a clear anticrossing between the excitons and the cavity mode, revealing the [SCR](#). Furthermore, under non-resonant optical excitation, the [MC](#) exhibits non-linear stimulated emission. This part was based on the proposal of a [BCL](#) [51]. However, studies of exciton dynamics showed that the radiative cascade wasn't the dominant relaxation mechanism [71, 84]. A recent theoretical study tried to explain this suppression of the radiative transitions and proposed a new alternative scheme based on double [QW](#) structures [84]. Nevertheless, we showed that excitons relax much faster in the parabolic potential compared to a structure with conventional rectangular [QWs](#). The theoretical modeling of relaxation dynamics qualitatively agreed with the experimental results and predicted the time evolution of exciton densities at each level of the [PQW](#), along with the photoluminescence contribution of each transition.

The second goal was the design, build, and evaluation of a new [THz-TDS](#) experimental setup. The setup was successfully built and tested and preliminary results were presented. It is able to generate and detect THz radiation, externally pump the sample under study, and perform measurements at low temperatures by the use of a cryostat. Both [THz-TDS](#) and [OPTP](#) measurements are possible. A preliminary evaluation was performed using samples such as [LT-GaAs](#), [Si HR](#), and a [PQW MC](#) structure.

Results on absorption/gain measurements on parabolic quantum well microcavities were also presented.

For a future perspective, an important step is to explore the propagation of THz radiation on a waveguide. This will result in a long gain medium and will significantly increase the overlap between the optical pump and the THz probe beams. Some investigations have already been published but there are mainly in plasmonic systems [85]. Nevertheless, it is a positive step towards the development of THz wave guiding materials and techniques.

The scientific community continues to study BCLs and propose new ways, structures, and systems capable of emitting THz radiation [50, 52, 71, 84, 86, 87]. Technology is advancing and THz related components and setups are getting better, faster, and more reliable. THz spectroscopy has evolved into a well established technique and many companies build and sell THz systems for spectroscopic and imaging applications.

Here, I'll discuss my thoughts for future changes and improvements. I'll point out some remarks, hoping that will help and accelerate the progress of the related experiments in the lab. My recommendations are mostly technical and are related to the specific setup in our lab.

About the optical elements:

First, the THz experimental setup, like the majority of this kind of setups, employs off-axis parabolic mirrors to guide the THz beam. These mirrors are useful because they are achromatic and turn the light path off-axis. Usually, these optics are 90 degrees off-axis, meaning that either they accept a divergent beam from a point source at their focal length and reflect it to a collimated beam at 90 degrees or they accept a collimated beam and reflect it to a focused beam at their focal length at 90 degrees. However, they are extremely sensitive to every movement and rotation and they are very difficult to align. Therefore, either lock their rotation and use high precision robust and fixed mounts or replace them. A good alternative is based on plastic materials (such as TPX) which are used to construct special lenses able to manipulate THz radiation in a much simpler approach. Using these lenses, a four-parabolic-mirror setup can be transformed to a one-line setup, easier to align and handle. Second, THz antennas are usually accompanied by a silicon lens to collimate, focus, or just decrease the high divergence of the THz beam. The position of this lens is also very important and sensitive, so it is better to choose an

antenna with the silicon lens pre-aligned and mounted from the company. There is no need to change the distance between the antenna and the silicon lens and you'll have one less thing to worry about.

About the instruments:

For the [OPTP](#) setup, two lock-in amplifiers are needed. It is better to have two digital amplifiers with pc connectivity. It is important because the setup will be able to simultaneously measure the signal from both of them in one scan, which considerably decreases the time needed. Till now, our automation programs can control two lock-in amplifiers, the SR830 and the EGG7260 (Appendix [A.5](#)).

About the lasers:

The setup is based on one laser, for both the operation of the antennas and the pumping of the sample. Antennas are very efficient around specific wavelengths, which typically are ~ 800 nm, 1060 nm, and 1550 nm, depending on the type of the antenna. In our experiments the most common one is the 800 nm. Therefore, keep in mind that there is a limitation of the laser wavelength tuning. The wavelength should be tuned near the antennas' optimized value of 800 nm. The same wavelength is used to photo-excite the sample. In addition, it has been noticed that when the laser wavelength is altered, the laser beam position slightly changes.

About the optical delay lines:

In a future upgrade of the setup consider replacing the delay lines. The translation stages and their controller are bulky and they take a lot of space on the table and on the shelves too. Concerning the optics on the stages, it is better to use a combination of a prism mirror and a 90 degrees V-Block with mirrors. Excellent compact optical delay line systems are commercially available.

About the automation control program:

Averaging is very important in this kind of measurements and this feature should be improved to the current automation program. It is very useful to easily scan multiple times and save all the scans and the average automatically. If two digital lock-in amplifiers with pc connectivity are available, add to the program the ability to measure both of them simultaneously. Finally, I believe it is time to re-write all the automation programs in NI LABVIEW. It will take some time but I am sure that it will be worth it.

About taking measurements:

An experimental setup like this has many different components. As you probably know, we don't live in a ideal world and something is almost always not working as intended. Therefore, when you are lucky enough and everything is working properly, try to take as much data as you can.

Appendix A

EXPERIMENTAL TECHNIQUES

Here, the experimental techniques, setups, and instruments are described. For temperature and position control the samples are usually mounted on a cryostat, so, first, the vacuum and cooling system is briefly explained. Second, the laser is described, a system common to the majority of the experimental setups. Then, the main characterisation techniques, reflectivity and luminescence, are presented, and finally our inhouse THz spectroscopy setup is described.

A.1 Vacuum and cooling system

To perform experiments at low temperatures, a cooling system is apparently needed. We use a closed cycle cryostat which is capable of reaching temperatures near 14 K without the need for cryogenics. The main components of the system are the expander (also known as the cold finger), the compressor, the vacuum chamber, and the vacuum pump.

The vacuum pump creates the necessary vacuum in the vacuum chamber where the cold finger is located and the refrigeration cycle takes place. In our system, a pressure of 10^{-6} mbar is usually obtained. Two gas lines from the compressor are connected to the expander. One line is responsible of providing high pressure Helium gas to the expander and the other of returning low pressure Helium gas to the compressor. The samples are glued with thermal conductive silver paint to special designed copper mounts which are placed at the end of the cold finger. The expander is mounted on a X-Y-Z axes stage for the position control of the sample.

For the temperature control, a temperature controller with a sensor and a heater is used. Both the sensor and the heater are located inside the cold finger and are responsible of maintaining the desired temperature. Our experiments usually require a temperature range of 4-300 K.

VACUUM PUMP: Pfeiffer vacuum Hicube.

COMPRESSOR: APD Cryogenics, HC-2 Helium vacuum cryo compressor, water cooled.

EXPANDER: APD Cryogenics, DE-202.

TEMPERATURE CONTROLLER: Oxford Instruments, 3120.

TEMPERATURE SENSOR: Oxford Instruments, 3-point calibrated Rhodium-Iron resistance sensor with a range of 1.4-800 K.

A.2 Continuous-wave and pulsed laser system

The great majority of light-matter interaction experiments use a laser as an excitation or probing tool. Our laser system consists of a Coherent Mira 900 and its pump laser, a Coherent Verdi V6.

COHERENT MIRA 900: A mode-locked ultrafast laser that uses Sapphire doped with Titanium (Ti:Sapphire) as a gain medium and is tunable from 700 to 980 nm. It can be operated in both **CW** and pulsed mode. The pulse-width is ~ 150 fs and the repetition rate is 76 MHz. The maximum output power is 500 mW.

COHERENT VERDI V6: A **CW** diode-pumped laser at 532 nm with a maximum output power of 6 W.

A.3 Reflectivity

Reflectivity is the ratio of the intensity of light reflected by the surface of a sample to the intensity of the incident light. Another term, reflectance, is used to describe the case where the sample reflects volumetrically, including its internal reflections between the rear and front faces. Thick opaque samples usually have the same reflectivity and reflectance value, while layered non-opaque samples have different. Even though there is a clear difference between the two definitions, sometimes the term reflectivity is used to describe all cases related to the phenomenon of reflection. In the present thesis, only the term reflectivity will be used, despite

the fact that reflectance is a more appropriate term for our samples.

In our experiments, reflectivity is a vital and very helpful measurement. It's the first characterisation step for every sample because it gives information about the stop-band and the detuning range of the structure. The experimental setup is quite simple; we only need a light source (a white-light lamp), a spectrometer to analyse the spectrum, and some optics/fibers to guide the light to/from the sample. We usually perform two kinds of reflectivity measurements, fiber and free-space, in both room and low temperature. Another reflectivity approach, at Brewster angle, is also used for the measurements of our [PQW](#) samples. All these experimental setups are described below.

A.3.1 Fiber / Free-space reflectivity

Reflectivity using fibers (Figure [A.1](#)) is a straight forward technique. A three-leg reflection probe with fiber cores is used. Two ends of the probe are terminated with connectors, one is connected to a lamp (multi-fiber leg), and the other to a spectrometer (single-fiber leg), while the third end is placed above the surface of the sample. Light from the lamp travels to the end of the leg where the sample is located. The reflected light from the sample enters the same leg and is guided to the spectrometer. The spectrometer is connected to a computer to control the experiment and display the spectrum.

Free-space reflectivity (Figure [A.1](#)) is more complicated but remains a simple experimental setup. It has the advantages of a clearer spectrum and a better focusing of the light. Light from a lamp passes through a series of optics to control the shape of it. We usually use lens to collimate the light and iris to control the size. Then, light goes to a beamsplitter and is focused to the sample with a lens. The reflected light from the sample passes through the same lens which collimates it. After that, it passes through the beamsplitter and is guided with mirrors to the spectrometer where it is focused to the slit with a lens. The spectrometer is again connected to a computer to control the experiment and display the spectrum.

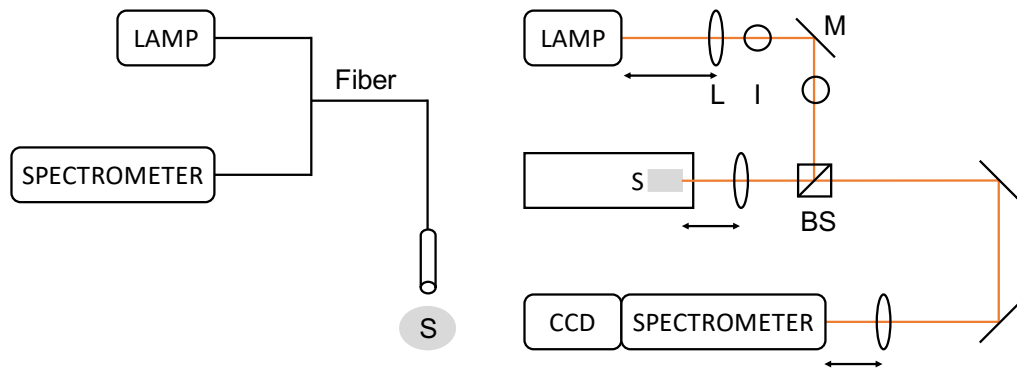


Figure A.1: Fiber (left) and free-space (right) reflectivity setups. S: sample, L: lens, I: iris, M: mirror, BS: beamsplitter. The arrow indicates the focal length of the lens.

LAMP: 1. Ocean Optics LS1 Tungsten Halogen light source.
2. Mikropack DH-2000 Deuterium Halogen UV-VIS-NIR light source.

FIBER: Ocean Optics.

SPECTROMETER: Ocean Optics HR2000CG-UV-NIR.

SPECTROMETER AND CCD: Princeton Instruments Acton SP2500 0.5 m imaging triple grating monochromator spectrograph + Pylon.

A.3.2 Brewster angle reflectivity

Brewster angle reflectivity is used when high signal to noise ratio is needed. The experimental setup (Figure A.2) has a few optical elements but attention is needed to achieve the Brewster angle. Light from a lamp passes through a polariser to acquire p-polarisation (transverse magnetic). A lens is used to focus the light and a mirror to guide it to the sample in the Brewster angle. Then, another mirror collects the light and guides the beam to a lens to focus it on the spectrometer. The spectrometer is connected to a computer to control the experiment and display the spectrum.

To calculate the Brewster angle you need to know the refractive indices of the two media that light travels through. If the initial medium has a refractive index n_1 and the second medium n_2 , the Brewster angle can be calculated by the equation $\theta_B = \arctan(\frac{n_2}{n_1})$. After calculating the Brewster angle, it's easy to find the appropriate lengths (x and y in Figure A.3) in order to place the mirror in the correct position.

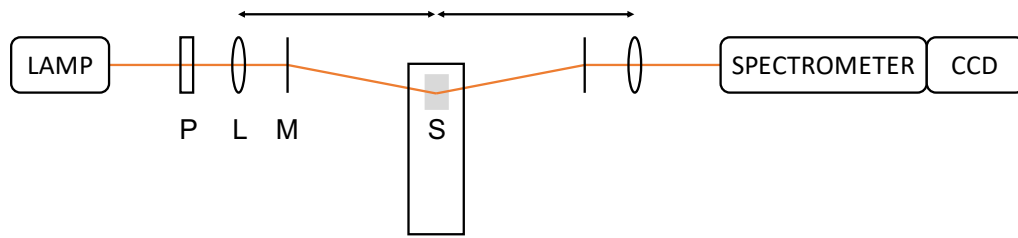


Figure A.2: Brewster angle reflectivity setup. P: polariser, L: lens, M: mirror, S: sample. The arrow indicates the focal length of the lens.

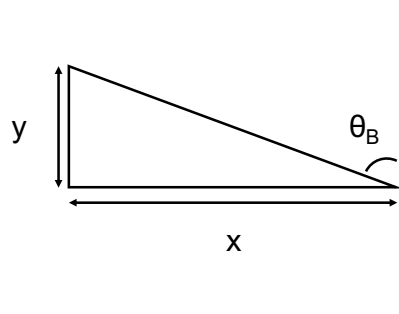


Figure A.3: θ_B : Brewster angle. Length y is related to the height of the mirror while x to the horizontal distance between the mirror and the surface of the sample. Note that y is calculated from the height of the sample, not from the optical table.

A.4 Luminescence

Luminescence is a general term which describes the phenomenon of light emission from a material. When a material absorbs energy, its carriers are excited and due to the unstable nature of the excited states, they fall back to the ground state. The absorbed energy is released in the form of heat, light, or both. There are many different types of luminescence, depending on the cause of the excitation e.g. electroluminescence for electrical current, chemiluminescence for a chemical reaction, etc. Here, laser light is used to excite the samples, therefore, the method is called photoluminescence (PL). The PL experimental techniques are described below.

A.4.1 Photoluminescence

PL is a well established technique and one of the most widely used for the characterisation of semiconductor materials, nanostructures, and devices.

It is a non-destructive method and gives information about processes near the bandgap energy. Depending on what we need to study, the experimental setup slightly changes. A PL experimental setup is relatively simple, but when an angle dependence of the emission is needed, it can be more complicated in terms of alignment.

At its simplest form, a PL setup requires a laser, a spectrometer, one lens for focusing to the sample, and a two-lens system for collecting the emission and focusing it to the spectrometer. In our lab we use an experimental setup for both PL and angle dependent PL (known as k-space imaging) which is described in the next section.

A.4.2 Photoluminescence, k-space / real-space imaging

We usually perform three kinds of measurements, PL, k-space imaging, and real-space imaging. The experimental setup for both PL and k-space imaging is shown in Figure A.4. The setup is the same for both measurements, the only difference is at the settings of the spectrometer. If the spectrometer is in "imaging mode", all the angles which the objective lens is capable of collecting, are shown. If it is in "spectroscopy mode" and the appropriate pixel range is selected, only the angle equals zero is shown.

Laser light is guided through a mirror to a beamsplitter. A part of it is focused to the sample with an objective lens. The same objective lens collects the PL and displays the Fourier plane at its focal length. The Fourier plane is projected to the spectrometer by a combination of two lenses. In case we need to see the surface of the sample, the real-space imaging setup should be used. To change from k-space imaging to real-space imaging, we only need to add or remove one lens. We usually add a lens (Figure A.5) because it's easier to return back to the k-space setup without changing again the alignment.

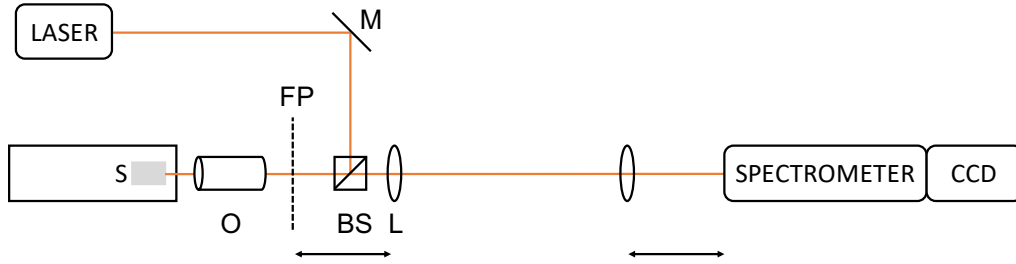


Figure A.4: k-space imaging. S: sample, O: objective lens, FP: Fourier plane, BS: beamsplitter, M: mirror, L: lens. The arrow indicates the focal length of the lens.

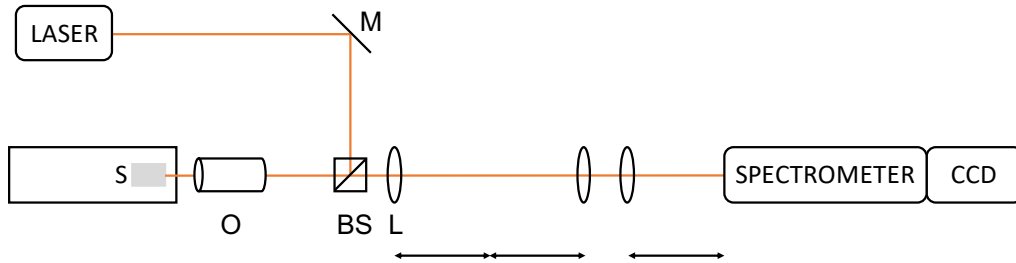


Figure A.5: Real space imaging. S: sample, O: objective lens, BS: beam-splitter, M: mirror, L: lens. The arrow indicates the focal length of the lens.

A.5 Terahertz spectroscopy

The THz setup is based on a typical pump-probe setup where a femtosecond laser beam is split into two parts. The first is used to pump the generation antenna (pump) and the other to activate the detection antenna (probe). The experimental setup is shown in Figure A.6. Light pulses from the femtosecond Ti:Sapphire laser arrive at the first beamsplitter and are split into two parts, the red and the blue. The red part is sent to a beam-splitter and is split into two parts, the red and the green. The red is the one which optically excites the generation antenna and generates THz pulses while the green activates the detection antenna to measure the THz pulses. A linear translation stage is used to change the time delay between the two parts and obtain the whole THz pulse profile.

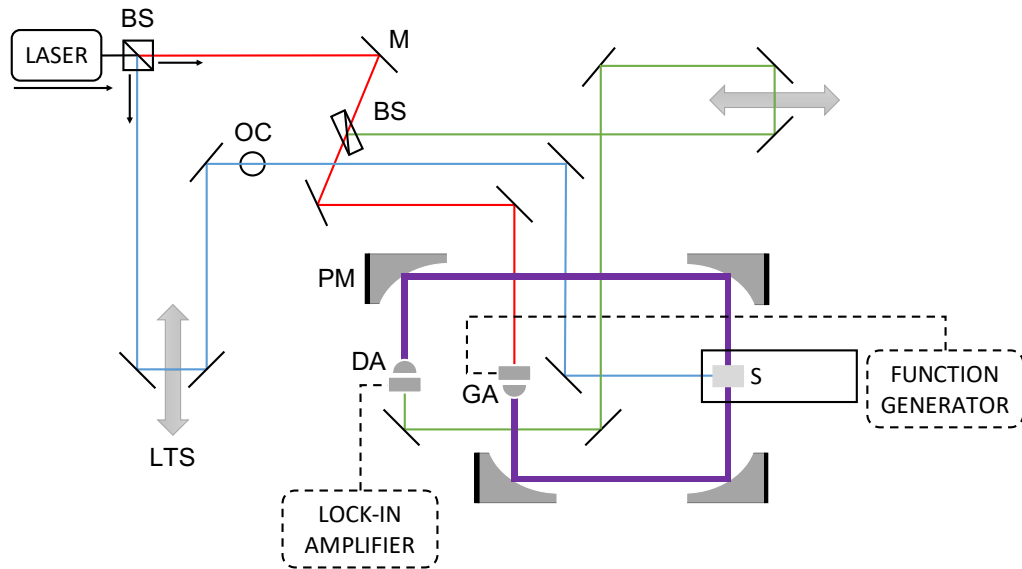


Figure A.6: The THz setup. BS: beamsplitter, LTS: linear translation stage, M: mirror, OC: optical chopper, PM: parabolic mirror, DA: detection antenna, GA: generation antenna, S: sample.

After the THz generation, the THz pulses are collected, transmitted, and focused, by four parabolic mirrors. The first parabolic mirror collects and collimates the pulses and the second focuses them to its focal length. The third, similar to the first, collects and collimates the pulses while the last focuses them to the detection antenna. The sample is placed at the focal length of the second parabolic mirror, in the middle of the distance between the second and the third mirror.

Till now, the effect of the sample to the transmitted THz pulse can be studied. Sometimes though, we need to study the ability of the sample itself to generate THz radiation. This is the first of two reasons why the first beamsplitter splits the beam to the blue line part. This laser part is used to optically excite the sample, usually at a 45 or 0 degrees angle. The emitted THz pulses are collected from the third parabolic mirror, are collimated and transmitted to the fourth, and focused to the detection antenna like the previous case. To obtain the whole THz pulse profile, another linear translation stage is used to scan the time delay between the two paths. The second and most important reason though, is related to another type of a THz-TDS method, the so-called OPTP spectroscopy. The OPTP setup is a modified THz-TDS setup in which the sample is also pumped by an

optical pulse. The THz pulses from the generation antenna pass through the sample, as usual in the original THz-TDS setup. Although, the photo-excitation of charged carriers in the sample increases its conductivity, thus, decreases the transmission of the THz pulse. Therefore, the OPTP technique is used to study the effect of the optical pump on the transmitted THz pulse.

To perform an experiment, a function generator (or a chopper, or both) and a lock-in amplifier (or two) are also required. A computer is used to control all the instruments and acquire the data. The basic measurement consists of scanning the time delay and measuring the THz-induced modulation by a lock-in amplifier. The acquired information is in the time domain and can be transformed to the frequency domain with a Fourier transform.

Here, we performed four kinds of measurements and we refer to them as THz-TDS probe (single lock-in probe), THz-TDS pump (single lock-in pump), OPTP probe (double lock-in probe), and OPTP pump (double lock-in pump). Each one has a specific purpose and different characteristics and instrument connections. All the instrument connections are shown in Figures A.7, A.8, and A.9. The THz-TDS and the OPTP setup mentioned earlier are based on single lock-in and double lock-in detection, respectively.

THz-TDS probe (single lock-in probe) is the basic kind of measurement in which the antenna is used to generate the THz waves, one lock-in amplifier connected to the detection antenna is used to measure, one translation stage controls the time delay, there is no external optical pumping of the sample, and, thus, only the THz radiation that goes through the sample is measured.

THz-TDS pump (single lock-in pump) is the kind of measurement in which the sample is optically pumped in order to measure its own THz generation. The generation antenna is not used, one translation stage controls the time delay, and the same lock-in amplifier, but now with a frequency reference from an optical chopper placed in the pump laser beam, is used to measure the THz emission.

OPTP (double lock-in) is a method which uses two lock-in amplifiers, both the function generator and the optical chopper, and both the translation stages. The first lock-in amplifier, similar to the single lock-in probe setup, receives the signal from the detection antenna and is locked to the fre-

quency of the function generator. The second lock-in amplifier receives the signal from the first amplifier and is locked to the frequency of the optical chopper located in the path of the pump beam. The sample is optically pumped and the effect of this pumping to the transmitted THz waves, is studied. The difference between the two versions of the double lock-in technique is related to which translation stage is fixed and which is scanned. Consequently, double lock-in probe means that the delay stage of the THz is scanned and the delay stage of the pump beam is fixed, while double lock-in pump is the opposite.

LINEAR TRANSLATION STAGE: OWIS SMK02-Z and LIMES120, full step resolution 2.5 μm .

PHOTOCONDUCTIVE ANTENNA: MenloSystems TERA8-1 and T8-H2 holder. The photoconductive material is [LT-GaAs](#), optimized for laser wavelength 800 nm and maximum optical power 10 mW at 100 MHz, 40 Volts maximum bias for emitter, mounted on a 40 mm x 40 mm PCB.

LOCK-IN AMPLIFIER: 1. Stanford Research Systems, SR830 DSP.
2. EG&G Princeton Applied Research model 128A.
3. EG&G Instruments 7260 DSP.

Note that in our automation programs, the measurement is performed either with the SR830 as the second lock-in amplifier or with both the SR830 and the EGG7260 connected and controlled by two separate programs, with SR830 being the first amplifier and EGG7260 the second.

FUNCTION GENERATOR: ISO-TECH GFG2004.

OPTICAL CHOPPER: THORLABS MC2000.

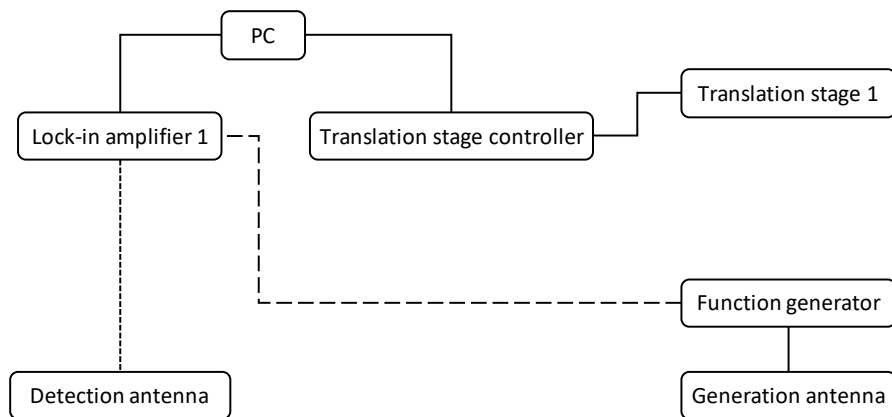


Figure A.7: Instrument connections of THz-TDS probe setup.

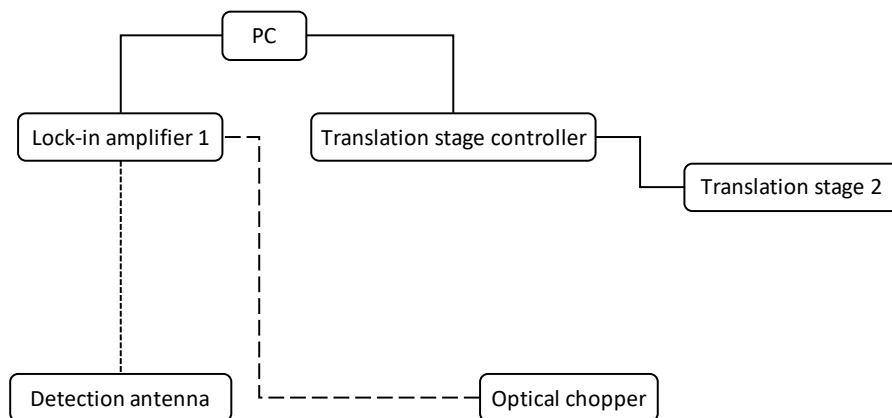


Figure A.8: Instrument connections of THz-TDS pump setup.

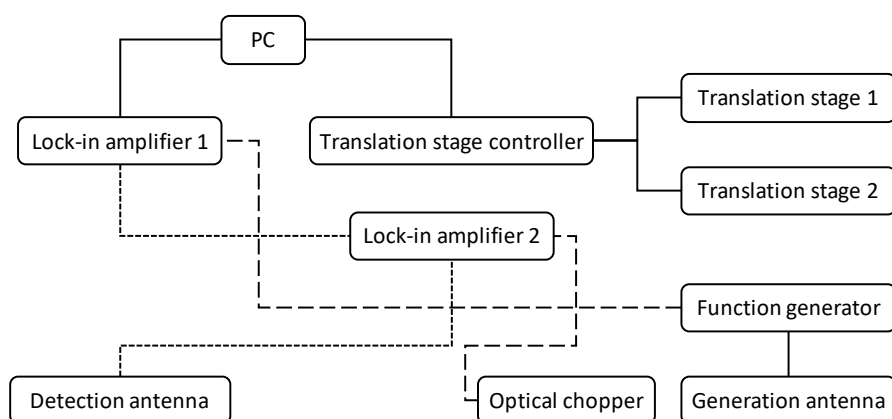


Figure A.9: Instrument connections of OPTP setup, where the first lock-in amplifier is connected to the frequency of the antenna (function generator) and the second to the frequency of the pump beam (optical chopper).

A.6 Pump-probe spectroscopy for THz oscillations

Broadband femtosecond pulses are used to pump and probe the sample. The probe reflection is filtered through a monochromator and is measured by a photodiode connected to a lock-in amplifier. The monochromator is scanned in energy. Oscillations are measured at specific energies and we convert them from frequency to energy. By knowing the selected energy from the monochromator and the converted energy from the oscillation, we can identify specific transitions. This spectral selection allow us to detect different excitonic transitions as a function of the pump-probe delay time.

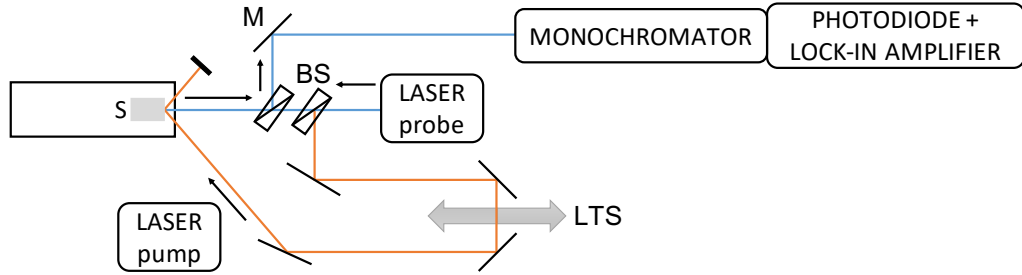


Figure A.10: The pump-probe setup for the observation of THz oscillations. S: sample, BS: beamsplitter, M: mirror, LTS: linear translation stage.

A.7 λ -modulated reflectivity

Instead of directly measuring an optical spectrum, the derivative of this spectrum with respect to a parameter is measured. This can be accomplished by applying the parameter as a small periodic perturbation and measuring the corresponding change in the optical properties with a lock-in amplifier [88].

In our case, the above mentioned parameter is the wavelength. We use a monochromator and a modulation slit which oscillates and periodically changes the output wavelength. A white light lamp is used at the entrance of the monochromator and the output is focused on the sample. The reflection from the sample is detected from a photodiode which is connected to a lock-in amplifier. The oscillating signal that is applied to

the entrance slit of the monochromator is also applied as a reference frequency to the lock-in amplifier. The measured signal from the amplifier is proportional to the derivative of the reflection spectrum.

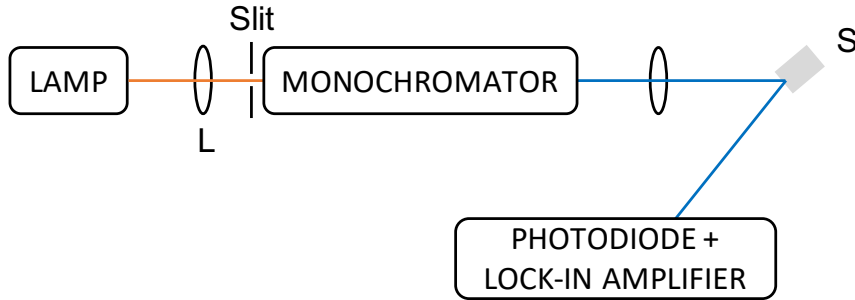


Figure A.11: The λ -modulated reflectivity setup for the identification of the excitonic states in the PQW. S: sample, L: lens.

A.8 Double-pump technique for relaxation dynamics

The setup is based on a typical PL experiment but instead of one pump pulse, it employs two pulses with a controlled time delay between them. It is used to highlight relaxation processes in the PQW MC structures. Laser pulses are split into two paths and one of them is delayed using a linear translation stage. The two pulses meet again and are focused to the sample. PL from the sample is collected and is guided to a spectrometer coupled with a CCD.

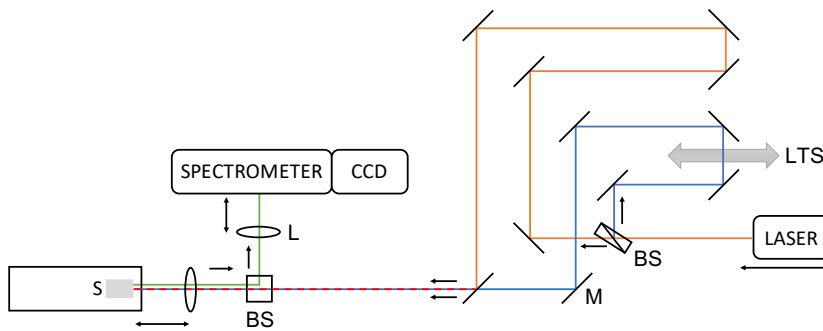


Figure A.12: BS: beamsplitter, LTS: linear translation stage, M: mirror, S: sample, L: lens. The arrow indicates the focal length of the lens.

Appendix B

CODES AND CALCULATIONS

B.1 The parabolic potential well

The parabolic potential well [89] is a direct analogy to the classical-mechanical concept of the harmonic oscillator, where the potential is proportional to the square of the displacement

$$V(z) = C \frac{z^2}{2}, \quad (\text{B.1})$$

where C is a constant and z the displacement. If a particle of mass m is in the equilibrium position and is displaced by Δz , the restoring force is proportional to

$$-\frac{\partial V}{\partial z} = -Cz, \quad (\text{B.2})$$

causing oscillations of amplitude Δz and angular frequency

$$\omega = \sqrt{\frac{C}{m}}. \quad (\text{B.3})$$

The behaviour of a quantum particle (such as an electron or a hole) in a parabolic potential is different. The Schrodinger equation for this case would be

$$-\frac{\hbar^2}{2m^*} \frac{\partial^2}{\partial z^2} \psi + C \frac{z^2}{2} \psi = E \psi, \quad (\text{B.4})$$

and by substituting ω for C the equation becomes

$$-\frac{\hbar^2}{2m^*} \frac{\partial^2}{\partial z^2} \psi + m^* \omega^2 \frac{z^2}{2} \psi = E \psi. \quad (\text{B.5})$$

A detailed solution of the eigen-value problem can be found in [89, 90]. It is shown that the energy levels are given by

$$E_n = \left(n + \frac{1}{2}\right)\hbar\omega, \quad n = 0, 1, 2, 3, \dots, \quad (\text{B.6})$$

where $n = 0$ is the ground state. The above solution shows that the energy levels are quantized and the ground state energy is $\hbar\omega/2$. Above this, the remaining energy steps are equally-spaced (Figure B.1), contrary to the case of the square potential well where the energy levels are proportional to n^2 .

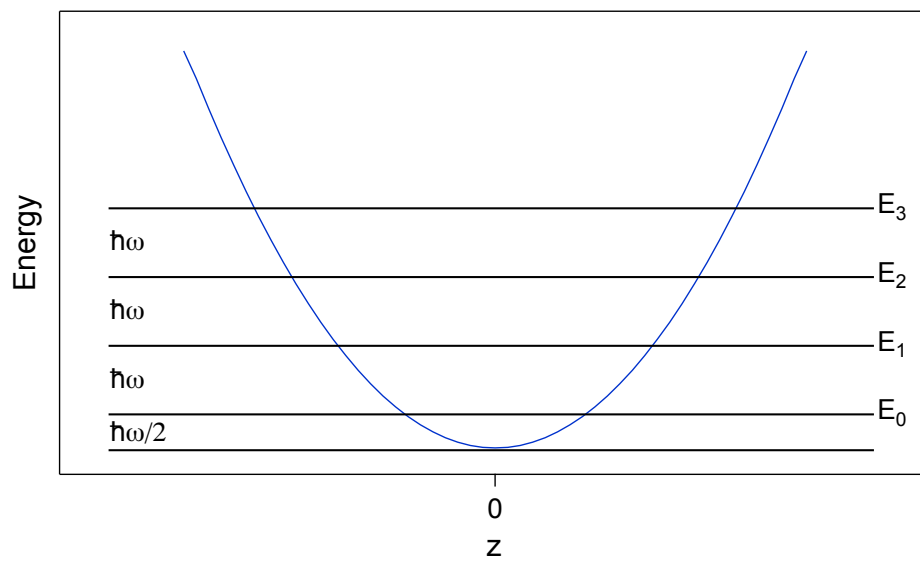


Figure B.1: The quantum-mechanical harmonic oscillator.

B.2 Igor Pro code: Sample structure design

The following code was written in the programming environment of the scientific data analysis software Wavemetrics Igor Pro. The algorithm is used to design the structure of the [PQW MC](#) sample measured in Chapter 2.

```
Function microcav242()           // ParabolicMC Al
  air(50)
  DBR(17,0.15,1,56.14,64.26);    // top mirror
  AlGaAs(0.15,87.2)

  AlGaAs(0.11,3.333)             //parabolic profile
  AlGaAs(0.10,3.333)
```

```

AlGaAs(0.09,3.333)
AlGaAs(0.08,3.333)
AlGaAs(0.07,3.333)
AlGaAs(0.06,3.333)
AlGaAs(0.055,3.333)
AlGaAs(0.05,3.333)
AlGaAs(0.055,3.333)
AlGaAs(0.06,3.333)
AlGaAs(0.07,3.333)
AlGaAs(0.08,3.333)
AlGaAs(0.09,3.333)
AlGaAs(0.10,3.333)
AlGaAs(0.11,3.333)

AlGaAs(0.15,87.2)
DBR(22,1,0.15,64.26,56.14);      // bottom mirror
GaAssubstrate()
End

```

B.3 Igor Pro code: Four oscillator model

The following code was written in the programming environment of the scientific data analysis software Wavemetrics Igor Pro. The algorithm is used to calculate the polariton branches in order to fit the experimental polariton dispersion data. It creates a panel and can calculate four polariton branches (LP, MP1, MP2, UP), taking into account three excitons, the detuning value, and the effective refractive index of the structure. To calculate and display the polariton branches, first run the function Initialize() and then the function Graph(). Adjust the parameters accordingly.

```

#pragma rtGlobals=1
// run initialize

function Initialize()
variable/g Detuning, Ecav, Eexc1, Eexc2, Eexc3, Coupling1, Coupling2, Coupling3, neff

make/n=120/d/O ANGLE_RAD
make/n=120/d/O ANGLE_DEG
make/n=120/d/O CAV
make/n=120/d/O LP
make/n=120/d/O MP1
make/n=120/d/O MP2
make/n=120/d/O UP
make/n=120/d/O EXC1
make/n=120/d/O EXC2
make/n=120/d/O EXC3
make/n=(4,4)/d/O HH
make/n=4/d/O EIGVREAL
SetScale/I x -50*pi/180,50*pi/180,"120", ANGLE_RAD
ANGLE_RAD=x
ANGLE_DEG=ANGLE_RAD*180/pi
execute "SliderPanel()"

```

end

```
function FourOscillator_Tz()
variable ii
nvar Detuning, Ecav, Eexc1, Eexc2, Eexc3, Coupling1, Coupling2, Coupling3, neff
wave ANGLE_RAD, ANGLE_DEG, CAV, LP, MP1, MP2, UP, EXC1, EXC2, EXC3, HH, EIGVREAL
//INPUTS-----
//Neff=3.35
//Detuning=-4 // meV   Cav = Eexc1
//Eexc1=1.5225 // eV
//Eexc2=Eexc1+0.002 // eV
//Eexc3=Eexc1+0.012 // eV
//Coupling1=0.009 // eV
//Coupling2=0.003 // eV
//Coupling3=0.002 // eV
Ecav=Eexc1+Detuning // eV
//INPUTS-----
EXC1=Eexc1
EXC2=Eexc2
EXC3=Eexc3
```

```
for(ii=0; ii<dimsize(ANGLE_RAD,0); ii+=1)
    CAV[ii]=Ecav*(1-(sin(ANGLE_RAD[ii]))^2/Neff^2)^(-1/2) // eV
    HH[0][0]=CAV[ii]
    HH[0][1]=Coupling1
    HH[0][2]=Coupling2
    HH[0][3]=Coupling3
    HH[1][0]=Coupling1
    HH[1][1]=Eexc1
    HH[1][2]=0
    HH[1][3]=0
    HH[2][0]=Coupling2
    HH[2][1]=0
    HH[2][2]=Eexc2
    HH[2][3]=0
    HH[3][0]=Coupling3
    HH[3][1]=0
    HH[3][2]=0
    HH[3][3]=Eexc3

    MatrixEigenV/R HH // matrix solution
    Wave W_Eigenvalues, M_R_eigenVectors
    EIGVREAL=real(W_Eigenvalues)
    Sort EIGVREAL EIGVREAL // rearranging the data values
    LP[ii]=EIGVREAL[0]
    MP1[ii]=EIGVREAL[1]
    MP2[ii]=EIGVREAL[2]
    UP[ii]=EIGVREAL[3]
endfor
end
```

```
Function SliderProc(sa) : SliderControl
STRUCT WMSliderAction &sa

switch( sa.eventCode )
case -1: // control being killed
    break
default:
    if( sa.eventCode & 1 ) // value set
        Variable curval = sa.curval
        FourOscillator_Tz()
    endif
    break
endswitch

return 0
End
```

```
Function SetVarProc(sva) : SetVariableControl
STRUCT WMSetVariableAction &sva

switch( sva.eventCode )
case 1: // mouse up
case 2: // enter key
case 3: // live update
    Variable dval = sva.dval
    String sval = sva.sval
    FourOscillator_Tz()
    break
case -1: // control being killed
```



```

        break
    endswitch

    return 0
End

Window SliderPanel() : Panel
    PauseUpdate; Silent 1 // building window
    NewPanel /W=(711,56,1265,668) as "SliderPanel"
    ShowTools/A
    Slider Detuning_slider , pos={90,18}, size={288,55}, proc=SliderProc
    Slider Detuning_slider , limits={-0.012,0.012,0.0001}, variable= Detuning , vert= 0
    Slider Coupling1_slider , pos={90,90}, size={288,55}, proc=SliderProc
    Slider Coupling1_slider , limits={0,0.01,0.0001}, variable= Coupling1 , vert= 0
    Slider Coupling2_slider , pos={90,161}, size={288,55}, proc=SliderProc
    Slider Coupling2_slider , limits={0,0.01,0.0001}, variable= Coupling2 , vert= 0
    Slider Coupling3_slider , pos={90,234}, size={288,55}, proc=SliderProc
    Slider Coupling3_slider , limits={0,0.01,0.0001}, variable= Coupling3 , vert= 0
    Slider Exciton1_slider , pos={90,318}, size={288,45}, proc=SliderProc
    Slider Exciton1_slider , limits={1.4,1.6,0.0001}, variable= Eexc1 , vert= 0
    Slider Exciton2_slider , pos={90,388}, size={288,45}, proc=SliderProc
    Slider Exciton2_slider , limits={1.4,1.6,0.0001}, variable= Eexc2 , vert= 0
    Slider Exciton3_slider , pos={90,460}, size={288,45}, proc=SliderProc
    Slider Exciton3_slider , limits={1.4,1.6,0.0001}, variable= Eexc3 , vert= 0
    Slider neff_slider , pos={90,532}, size={288,45}, proc=SliderProc
    Slider neff_slider , limits={3,6,0.01}, variable= neff , vert= 0
    TextBox Detuning_title , pos={18,18}, size={60,24}, title="Detuning" , fSize=12
    TextBox Detuning_title , frame=2
    TextBox Coupling1_title , pos={18,90}, size={65,24}, title="Coupling1" , fSize=12
    TextBox Coupling1_title , frame=2
    TextBox Coupling2_title , pos={18,161}, size={65,24}, title="Coupling2" , fSize=12
    TextBox Coupling2_title , frame=2
    TextBox Coupling3_title , pos={18,234}, size={65,24}, title="Coupling3" , fSize=12
    TextBox Coupling3_title , frame=2
    TextBox Exciton1_title , pos={18,318}, size={58,24}, title="Exciton1" , fSize=12
    TextBox Exciton1_title , frame=2
    TextBox Exciton2_title , pos={18,388}, size={58,24}, title="Exciton2" , fSize=12
    TextBox Exciton2_title , frame=2
    TextBox Exciton3_title , pos={18,460}, size={58,24}, title="Exciton3" , fSize=12
    TextBox Exciton3_title , frame=2
    TextBox neff_title , pos={18,532}, size={31,24}, title="neff" , fSize=12, frame=2
    SetVariable Detuning_value , pos={387,18}, size={140,19}, proc=SetVarProc , fSize=12
    SetVariable Detuning_value , limits={-0.012,0.012,0.0001}, value= Detuning
    SetVariable Coupling1_value , pos={387,90}, size={140,19}, proc=SetVarProc , fSize=12
    SetVariable Coupling1_value , limits={0,0.01,0.0001}, value= Coupling1
    SetVariable Coupling2_value , pos={387,161}, size={140,19}, proc=SetVarProc , fSize=12
    SetVariable Coupling2_value , limits={0,0.01,0.0001}, value= Coupling2
    SetVariable Coupling3_value , pos={387,234}, size={140,19}, proc=SetVarProc , fSize=12
    SetVariable Coupling3_value , limits={0,0.01,0.0001}, value= Coupling3
    SetVariable Exciton1_value , pos={387,318}, size={140,19}, proc=SetVarProc , fSize=12
    SetVariable Exciton1_value , limits={1.5,1.6,0.0001}, value= Eexc1
    SetVariable Exciton2_value , pos={387,388}, size={140,19}, proc=SetVarProc , fSize=12
    SetVariable Exciton2_value , limits={1.5,1.6,0.0001}, value= Eexc2
    SetVariable Exciton3_value , pos={387,460}, size={140,19}, proc=SetVarProc , fSize=12
    SetVariable Exciton3_value , limits={1.5,1.6,0.0001}, value= Eexc3
    SetVariable neff_value , pos={387,532}, size={140,19}, proc=SetVarProc , fSize=12
    SetVariable neff_value , limits={3,6,0.01}, value= neff
    ToolsGrid snap=1, visible=1
EndMacro

Function Graph()
    Display CAV,LP,MP1,MP2,UP,EXC1,EXC2,EXC3 vs ANGLE_DEG
    ModifyGraph mirror=1
    ModifyGraph standoff=0
    ModifyGraph tick=2
    ModifyGraph rgb(EXC1)=(65535,21845,0),rgb(EXC2)=(65535,21845,0),rgb(EXC3)=(65535,21845,0)
    ModifyGraph rgb(CAV)=(16385,65535,65535)
    ModifyGraph rgb(LP)=(1,12815,52428),rgb(MP1)=(1,12815,52428),rgb(MP2)=(1,12815,52428),rgb(UP)=(1,12815,52428)
    ModifyGraph fSize=18,font="Arial"
    Label bottom "\\F'Arial'\\Z22Angle (Degrees)"
    Label left "\\F'Arial'\\Z22Energy (eV)"
end

```

B.4 THz-TDS control program: Step calculation

The automation program was written in Agilent Vee. Screenshot examples are shown below. The program controls the lock-in amplifier and the translation stages. The delay stage step calculation used in the program is:

1 cm = 4000 steps, 1 mm = 400 steps, 1 mm = 0.001 m

$$t = \frac{2 \cdot 0.001}{3 \cdot 10^8} = 6.67 \cdot 10^{-12} \text{ s}$$

$$t = 6.67 \text{ ps}$$

$$\frac{6.67}{400} = 0.016675 \text{ ps} \quad (\text{B.7})$$

1 step ($2.5 \mu\text{m}$) = path difference $5 \mu\text{m} = 0.016675 \text{ ps}$

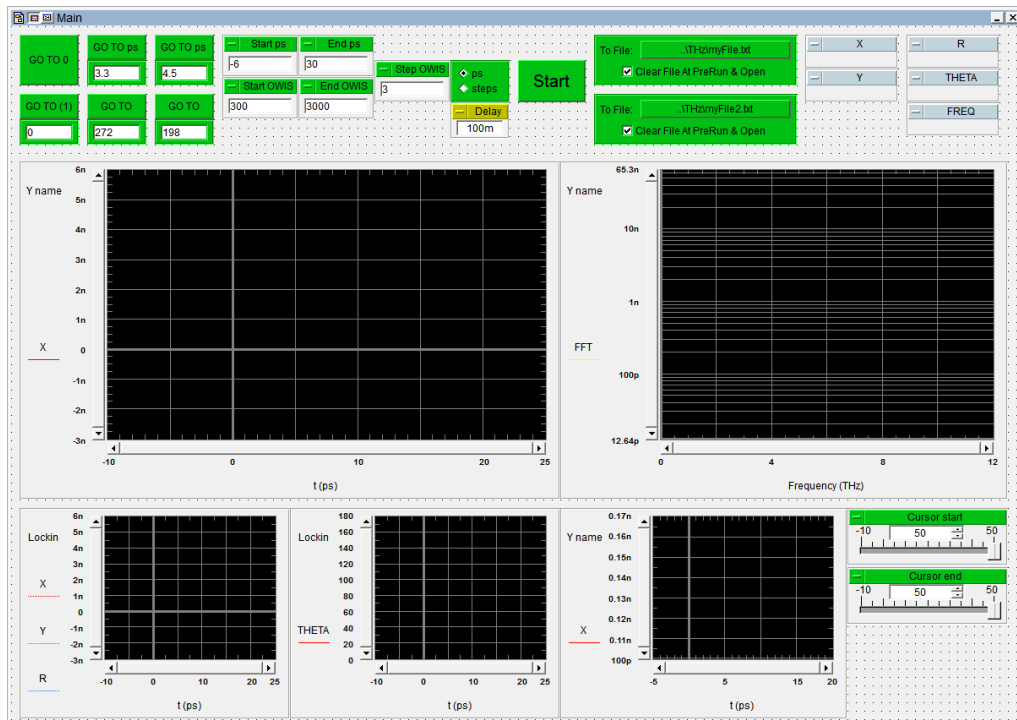


Figure B.2: Screenshot of the automation program showing the interface for the probe scan.

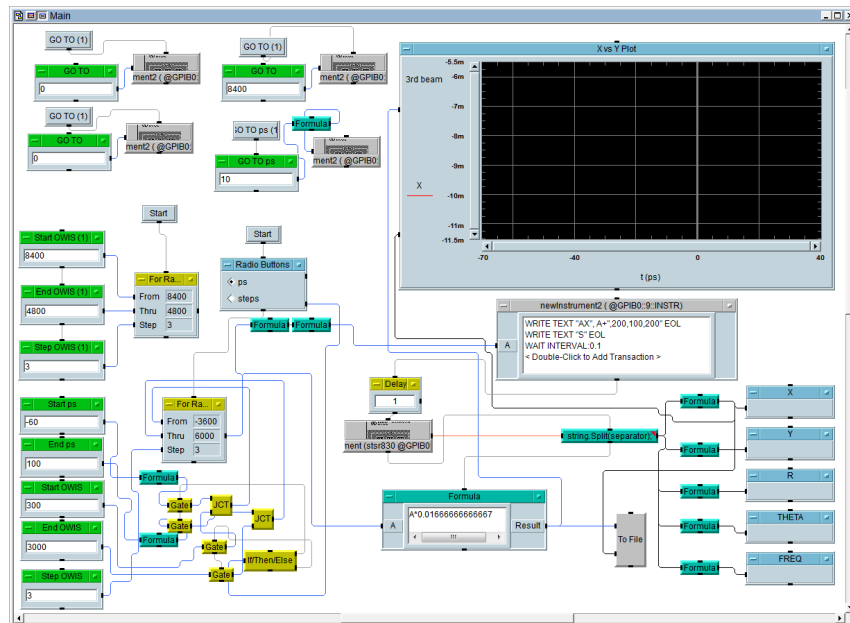


Figure B.3: Screenshot of the automation program showing the code for the pump scan.

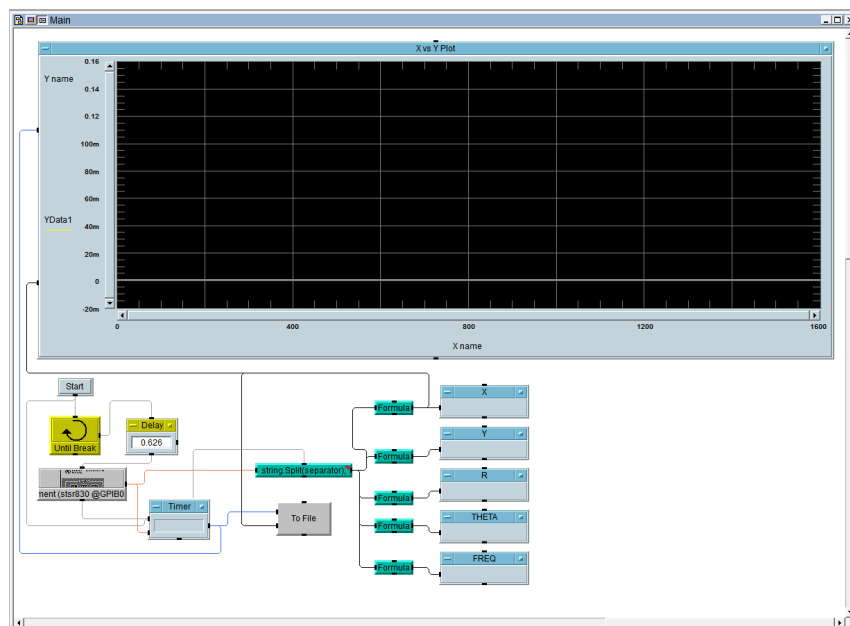


Figure B.4: Screenshot of the automation program showing an example of code to measure the value from the lock-in amplifier as time passes by. This is used to see the fluctuations of the measurement only due to the environment and the instrument, without changing anything else.

B.5 Igor Pro code: Procedure for FFT function and THz menu

The following code was written in the programming environment of the scientific data analysis software Wavemetrics Igor Pro. The algorithm is used to calculate the Fourier transform of time domain data. The first function (THz_FFT()) is used for the Fourier transform of all data and the second (THz_FFT_C()) for data between the two cursors of the program.

```
Function THz_FFT ()
variable numberOfRows, ps_min, ps_max
wave wave0, wave1
// need: wave0 (1 column, x-axis, time in ps),
// wave1 (1 column, y-axis, current in Ampere),
// and even number of rows

numberOfRows=DimSize(wave1,0)

if (mod(numberOfRows,2)==1)
DeletePoints 0,1, wave0
DeletePoints 0,1, wave1
endif

ps_min=wave0[0]
ps_max=wave0[numberOfRows-1]
print ps_min
print ps_max

SetScale/I x ps_min, ps_max, "", wave1
wave1=wave1*10^9 //convert to nanoAmpere
Display wave1
Label bottom "Time delay (ps)"
Label left "Current (nA)"

FFT/OUT=3/DEST=W_FFT1 wave1
//FFT/OUT=3/RP=[pcsr(A),pcsr(B)]/DEST=W_FFT_C wave1
Display W_FFT1
ModifyGraph log(left)=1
SetAxis bottom 0,6
Label bottom "Frequency (THz)"

end
```

```
Function THz_FFT_C()  
wave wave1  
  
if (mod((pcsr(B)-pcsr(A)),2)==1)  
FFT/OUT=3/RP=[pcsr(A),pcsr(B)]/DEST=W_FFT1_C wave1  
else  
FFT/OUT=3/RP=[pcsr(A)+1,pcsr(B)]/DEST=W_FFT1_C wave1  
endif  
  
Display W_FFT1_C  
ModifyGraph log(left)=1  
SetAxis bottom 0,6  
Label bottom "Frequency (THz)"  
  
end
```

To add a menu for the Fourier transform the following code was added to our custom menus procedure.

```
Submenu "THz"  
"FFT from wave0 and wave1",THz_FFT()  
"FFT from cursors",THz_FFT_C()  
End
```

B.6 Mathematica code: Loop scans

```
(*INPUT DIRECTORY AND FILENAME*)
dir = SetDirectory["/Users/tzalex/UoC/PhD/2_Lab_data_THz/49 2D"];
dataFile = Import["scan10_0d65ps.txt", "Table"];

(*INPUT SCAN PARAMETERS*)
wait = 9; (*waiting time for each point in seconds*)

(*parameters calculated from file*)
start = IntegerPart[dataFile[[1, 1]]] (*start position in ps*)
stop = IntegerPart[dataFile[[Length[dataFile], 1]]] (*stop position in ps*)
stepps = Abs[dataFile[[1, 1]] - dataFile[[2, 1]]] (*step in ps*)
numberOfPoints = IntegerPart[(Abs[start] + Abs[stop]) / stepps] + 1 (*number of points in one scan*)
loops = IntegerPart[Length[dataFile] / numberOfPoints] (*number of loops*)
totalTimeEachLoop = numberOfPoints * wait / 60. (*scan duration for each scan in minutes*)
totalTime = totalTimeEachLoop * loops (*total scan duration for all loops in minutes*)

(*seperate the two columns*)
col1 = Table[dataFile[[i, 1]], {i, 1, Length[dataFile]}];
col2 = Table[dataFile[[i, 2]], {i, 1, Length[dataFile]}];

col1c = Range[start, stop, stepps]; (*calculate the x range (time)*)
col1d = Take[col1, numberOfPoints]; (*take the x range (time) from data file col1*)

col2part = Partition[col2, numberOfPoints];
col2partAverage = Sum[col2part[[i]], {i, 1, loops}] / loops;

graph = Table[{col1d[[i]], col2partAverage[[i]] * 1000}, {i, 1, numberOfPoints}];
graphp = ListPlot[graph, Joined -> True, Frame -> True,
  FrameLabel -> {"Time (ps)", "Voltage (mV)"},
  PlotLabel -> "graph"]
Export["graph.pdf", graphp];
Export["graph.txt", graph, "Table"];
```

Figure B.5: Mathematica code for averaging a loop scan.

B.7 Mathematica code: 2D plot

```

dir = SetDirectory["/Users/tzalex/Desktop/data/2/data/"];
fn = FileNames["*.txt"];
dataFiles = Table[ReadList[fn[[i]], Number, RecordLists -> True], {i, 1, Length[fn]}];

Do[scans[i] = ListPlot[dataFiles[[i]], PlotRange -> {All, All}, Frame -> True,
    PlotLabel -> fn[[i]], FrameLabel -> {"Time (ps)", "Voltage (mV)", Joined -> True},
    {i, 1, Length[fn]}];

col1 = Table[dataFiles[[i, j, 1]], {i, 1, Length[fn]}, {j, 1, Length[dataFiles[[i]]]}];
col2 = Table[dataFiles[[i, j, 2]], {i, 1, Length[fn]}, {j, 1, Length[dataFiles[[i]]]}];
probeDelays2 = {-3, -1.2, -0.7, -0.45, -0.3, -0.2, 0, 0.2, 0.35, 0.65};
probeDelays = {-4, -2, -1.4, -1, -0.6, -0.4, -0.3, -0.2, 0, 0.2, 0.3, 0.4, 0.6, 0.8};

data = Flatten[Table[{col1[[1, i]], probeDelays[[j]], col2[[j, i]] * 1000},
    {j, 1, Length[probeDelays]}, {i, 1, Length[col1[[1]]}], 1];

graphp1 = ListContourPlot[data, ColorFunction -> "GrayTones",
    FrameLabel -> {"Pump delay time (ps)", "Probe delay time (ps)"},
    PlotLegends -> Automatic, PlotRange -> All];

graphp2 = ListPlot3D[data, ColorFunction -> "GrayTones", PlotRange -> All,
    AxesLabel -> {"Pump delay time (ps)", "Probe delay time (ps)", "Voltage (mV)"}];

Export["graph1.pdf", graphp1];
Export["graph2.pdf", graphp2];

```

Figure B.6: Mathematica code for plotting 2D graphs.

BIBLIOGRAPHY

- [1] Peter Y. Yu and Manuel Cardona. *Fundamentals of Semiconductors*. Graduate Texts in Physics. Springer Berlin Heidelberg, Berlin, Heidelberg, 2010. [14](#), [15](#)
- [2] Y. P. Varshni. Temperature dependence of the energy gap in semiconductors. *Physica*, 34:149–154, 1967. [14](#)
- [3] Claus F. Klingshirn. *Semiconductor Optics*. Graduate Texts in Physics. Springer Berlin Heidelberg, Berlin, Heidelberg, 2012. [15](#)
- [4] J. Frenkel. On the transformation of light into heat in solids. *Physical Review*, 37(1):17–44, 1931. [16](#)
- [5] Gregory H. Wannier. The structure of electronic excitation levels in insulating crystals. *Physical Review*, 52(3):191–197, 1937. [16](#)
- [6] S. B. Nam, D. C. Reynolds, C. W. Litton, R. J. Almassy, T. C. Collins, and C. M. Wolfe. Free-exciton energy spectrum in GaAs. *Physical Review B*, 13(2):761–767, 1976. [17](#)
- [7] Alexey V. Kavokin, Jeremy J. Baumberg, Guillaume Malpuech, and Fabrice P. Laussy. *Microcavities*. Oxford University Press, 2017. [18](#), [22](#)
- [8] M. S. Skolnick, T. A. Fisher, and D. M. Whittaker. Strong coupling phenomena in quantum microcavity structures. *Semiconductor Science and Technology*, 13(7):645–669, 1998. [18](#), [20](#)
- [9] V. Savona, L. C. Andreani, P. Schwendimann, and A. Quattropani. Quantum well excitons in semiconductor microcavities: Unified treatment of weak and strong coupling regimes. *Solid State Communications*, 93(9):733–739, 1995. [21](#)
- [10] Vincenzo Savona, Carlo Piermarocchi, Antonio Quattropani, Paolo Schwendimann, and Francesco Tassone. Optical properties of microcavity polaritons. *Phase Transitions*, 68:169–279, 1999. [22](#), [23](#), [24](#)

- [11] J. J. Hopfield. Theory of the contribution of excitons to the complex dielectric constant of crystals. *Physical Review*, 112(5):1555–1567, 1958. [22](#), [23](#)
- [12] Albert Einstein. Quantentheorie des einatomigen idealen Gases. In *Albert Einstein: Akademie-Vorträge*, pages 237–244. Wiley-VCH Verlag GmbH & Co. KGaA, Weinheim, FRG, sep 2006. [25](#)
- [13] Mike H Anderson, Jason R Ensher, Michael R Matthews, Carl E Wieman, and Eric A Cornell. Observation of Bose-Einstein condensation in a dilute atomic vapor. *Science*, 269(ii):198–201, 1995. [26](#)
- [14] C. C. Bradley, C. A. Sackett, J. J. Tollett, and R. G. Hulet. Evidence of Bose-Einstein condensation in an atomic gas with attractive interactions. *Physical Review Letters*, 75(9):1687–1690, 1995. [26](#)
- [15] K. B. Davis, M. O. Mewes, M. R. Andrews, N. J. Van Druten, D. S. Durfee, D. M. Kurn, and W. Ketterle. Bose-Einstein condensation in a gas of sodium atoms. *Physical Review Letters*, 75(22):3969–3973, 1995. [26](#)
- [16] Hui Deng, Hartmut Haug, and Yoshihisa Yamamoto. Exciton-polariton Bose-Einstein condensation. *Reviews of Modern Physics*, 82(2):1489–1537, 2010. [26](#)
- [17] Tim Byrnes, Na Young Kim, and Yoshihisa Yamamoto. Exciton-polariton condensates. *Nature Physics*, 10(11):803–813, 2014. [27](#)
- [18] Hui Deng, Gregor Weihs, Charles Santori, Jacqueline Bloch, and Yoshihisa Yamamoto. Condensation of semiconductor microcavity exciton polaritons. *Science*, 298(5591):199–202, 2002. [27](#)
- [19] J. Kasprzak, M. Richard, S. Kundermann, A. Baas, P. Jeambrun, J. M. J. Keeling, F. M. Marchetti, M. H. Szymńska, R. André, J. L. Staehli, V. Savona, P. B. Littlewood, B. Deveaud, and Le Si Dang. Bose-Einstein condensation of exciton polaritons. *Nature*, 443(7110):409–414, 2006. [27](#)
- [20] G. Tosi, G. Christmann, N. G. Berloff, P. Tsotsis, T. Gao, Z. Hatzopoulos, P. G. Savvidis, and J. J. Baumberg. Sculpting oscillators with light within a nonlinear quantum fluid. *Nature Physics*, 8(3):190–194, 2012. [27](#)

-
- [21] P. Cristofolini, A. Dreismann, G. Christmann, G. Franchetti, N. G. Berloff, P. Tsotsis, Z. Hatzopoulos, P. G. Savvidis, and J. J. Baumberg. Optical superfluid phase transitions and trapping of polariton condensates. *Physical Review Letters*, 110(18):1–5, 2013. [27](#)
- [22] A. Imamoglu, R. J. Ram, S. Pau, and Y. Yamamoto. Nonequilibrium condensates and lasers without inversion: Exciton-polariton lasers. *Physical Review A*, 53(6):4250–4253, jun 1996. [27](#)
- [23] A. A. Khalifa, A. P D Love, D. N. Krizhanovskii, M. S. Skolnick, and J. S. Roberts. Electroluminescence emission from polariton states in GaAs-based semiconductor microcavities. *Applied Physics Letters*, 92(6):1–4, 2008. [28](#)
- [24] Daniele Bajoni, Elizaveta Semenova, Aristide Lemaître, Sophie Bouchoule, Esther Wertz, Pascale Senellart, and Jacqueline Bloch. Polariton light-emitting diode in a GaAs-based microcavity. *Physical Review B*, 77(11):1–4, 2008. [28](#)
- [25] S. I. Tsintzos, N. T. Pelekanos, G. Konstantinidis, Z. Hatzopoulos, and P. G. Savvidis. A GaAs polariton light-emitting diode operating near room temperature. *Nature*, 453(7193):372–375, 2008. [28](#)
- [26] S. I. Tsintzos, P. G. Savvidis, G. Deligeorgis, Z. Hatzopoulos, and N. T. Pelekanos. Room temperature GaAs exciton-polariton light emitting diode. *Applied Physics Letters*, 94(7):7–9, 2009. [28](#)
- [27] H. Deng, G. Weihs, D. Snoke, J. Bloch, and Y. Yamamoto. Polariton lasing vs. photon lasing in a semiconductor microcavity. *Proceedings of the National Academy of Sciences*, 100(26):15318–15323, 2003. [28](#)
- [28] Daniele Bajoni, Pascale Senellart, Aristide Lemaître, and Jacqueline Bloch. Photon lasing in GaAs microcavity: Similarities with a polariton condensate. *Physical Review B*, 76(20):1–4, 2007. [28](#)
- [29] S. Christopoulos, G. Baldassarri Höger Von Högersthal, A. J D Grundy, P. G. Lagoudakis, A. V. Kavokin, J. J. Baumberg, G. Christmann, R. Butté, E. Feltin, J. F. Carlin, and N. Grandjean. Room-temperature polariton lasing in semiconductor microcavities. *Physical Review Letters*, 98(12):1–4, 2007. [28](#)
- [30] Pavlos G. Savvidis. Optoelectronics: A practical polariton laser. *Nature Photonics*, 8(8):588–589, 2014. [29](#)

- [31] Pallab Bhattacharya, Thomas Frost, Saniya Deshpande, Md Zunaid Baten, Arnab Hazari, and Ayan Das. Room temperature electrically injected polariton laser. *Physical Review Letters*, 112(23):29–31, 2014. [29](#)
- [32] Benjamin S. Williams. Terahertz quantum-cascade lasers. *Nature Photonics*, 1:517–525, 2007. [30](#), [33](#), [34](#), [37](#)
- [33] Greg Sun. The Intersubband Approach to Si-based Lasers. In *Advances in Lasers and Electro Optics*. InTech, 2010. [30](#)
- [34] X. C. Zhang and Jingzhou Xu. *Introduction to THz Wave Photonics*. Springer US, Boston, MA, 2010. [30](#), [31](#), [32](#), [60](#)
- [35] ESA / AOES Medialab. The Electromagnetic Spectrum. <http://sci.esa.int/education/50368-the-electromagnetic-spectrum/>, 2012. [31](#)
- [36] Martin van Exter, Ch. Fattinger, and D. Grischkowsky. Terahertz time-domain spectroscopy of water vapor. *Optics Letters*, 14(20):1128, 1989. [32](#), [59](#)
- [37] P. Uhd. Jepsen, R. H. Jacobsen, and S. R. Keiding. Generation and detection of terahertz pulses from biased semiconductor antennas. *Journal of the Optical Society of America B*, 13(11):2424, 1996. [32](#)
- [38] Masahiko Tani, M Herrmann, and Kiyomi Sakai. Generation and detection of THz pulsed radiation with photoconductive antennas. *Measurement Science and Technology*, 13:1739–1745, 2002. [32](#)
- [39] P. Uhd. Jepsen, D. G. Cooke, and M. Koch. Terahertz spectroscopy and imaging - Modern techniques and applications. *Laser and Photonics Reviews*, 5(1):124–166, 2011. [32](#)
- [40] G. Gallot and D. Grischkowsky. Electro-optic detection of terahertz radiation. *Journal of the Optical Society of America B*, 16(8):1204, 1999. [32](#)
- [41] R. F. Kazarinov and R. A. Suris. Possibility of the amplification of electromagnetic waves in a semiconductor with a superlattice. *Soviet Physics - Semiconductors*, 5(4):707–709, 1971. [33](#)
- [42] Jerome Faist, Federico Capasso, DL Sivco, C. Sirtori, A.L. Hutchinson, and A.Y. Cho. Quantum cascade laser. *Science*, 264(5158):553–556, 1994. [33](#), [37](#)

-
- [43] MenloSystems. The TERA8-1 photoconductive antenna. <http://www.menlosystems.com/>. 33
- [44] Rüdiger Köhler, Alessandro Tredicucci, Fabio Beltram, Harvey E. Beere, Edmund H. Linfield, A. Giles Davies, David A. Ritchie, Rita C. Iotti, and Fausto Rossi. Terahertz semiconductor-heterostructure laser. *Nature*, 417(6885):156–159, 2002. 34
- [45] Giacomo Scalari, Christoph Walther, Jerome Faist, Harvey Beere, and David Ritchie. Electrically switchable, two-color quantum cascade laser emitting at 1.39 and 2.3 THz. *Applied Physics Letters*, 88(14):3–6, 2006. 34, 37
- [46] Alan W. M. Lee, Qi Qin, Sushil Kumar, Benjamin S. Williams, Qing Hu, and John L. Reno. Real-time terahertz imaging over a standoff distance (>25 meters). *Applied Physics Letters*, 89(14):1–4, 2006. 34, 37
- [47] Benjamin S. Williams, Sushil Kumar, Qing Hu, and John Reno. Operation of terahertz quantum-cascade lasers at 164 K in pulsed mode and at 117 K in continuous-wave mode. *Optics express*, 13(9):3331–9, 2005. 34
- [48] Benjamin S. Williams, Sushil Kumar, Qing Hu, and John L. Reno. High-power terahertz quantum cascade lasers. In *2006 Conference on Lasers and Electro-Optics and 2006 Quantum Electronics and Laser Science Conference*, pages 1–2. IEEE, 2006. 34
- [49] Mikhail A. Belkin, Federico Capasso, Feng Xie, Alexey Belyanin, Milan Fischer, Andreas Wittmann, and Jerome Faist. Room temperature terahertz quantum cascade laser source based on intracavity difference-frequency generation. *Applied Physics Letters*, 92(20):1–3, 2008. 34
- [50] A. V. Nalitov, S. De Liberato, P. Lagoudakis, P. G. Savvidis, and A. V. Kavokin. Bosonic cascades of indirect excitons. *Superlattices and Microstructures*, 108:27–31, 2017. 34, 78
- [51] T. C. H. Liew, M. M. Glazov, K. V. Kavokin, I. A. Shelykh, M. A. Kaliteevski, and A. V. Kavokin. Proposal for a bosonic cascade laser. *Physical Review Letters*, 110(4):1–5, 2013. 34, 35, 37, 38, 40, 43, 51, 52, 57, 77

- [52] T. C. H. Liew and A. V. Kavokin. Optically induced transparency in bosonic cascade lasers. *Opt. Lett.*, 43(2):259–262, 2018. [34](#), [35](#), [78](#)
- [53] C. Weisbuch, M. Nishioka, A. Ishikawa, and Y. Arakawa. Observation of the coupled exciton-photon mode splitting in a semiconductor quantum microcavity. *Physical Review Letters*, 69(23):3314–3317, 1992. [37](#)
- [54] A Wallraff, D Schuster, A Blais, L Frunzio, R Huang, J Majer, S Kumar, S Girvin, and R Schoelkopf. Strong coupling of a single photon to a superconducting qubit using circuit quantum electrodynamics. *Nature*, 431(7005):162–167, 2004. [37](#)
- [55] E. Peter, P. Senellart, D. Martrou, A. Lemaître, J. Hours, J. M. Gérard, and J. Bloch. Exciton-photon strong-coupling regime for a single quantum dot embedded in a microcavity. *Physical Review Letters*, 95(6):1–4, 2005. [37](#)
- [56] K. Hennessy, A. Badolato, M. Winger, D. Gerace, M. Atatüre, S. Gulde, S. Fält, E. L. Hu, and A. Imamoglu. Quantum nature of a strongly coupled single quantum dot-cavity system. *Nature*, 445(7130):896–899, 2007. [37](#)
- [57] Dimitri Dini, Rüdiger Köhler, Alessandro Tredicucci, Giorgio Biasiol, and Lucia Sorba. Microcavity Polariton Splitting of Intersubband Transitions. *Physical Review Letters*, 90(11):4, 2003. [37](#)
- [58] Markus Geiser, Christoph Walther, Giacomo Scalari, Mattias Beck, Milan Fischer, Laurent Nevou, and Jerome Faist. Strong light-matter coupling at terahertz frequencies at room temperature in electronic LC resonators. *Applied Physics Letters*, 97(19), 2010. [37](#)
- [59] Y. Todorov, A. M. Andrews, I. Sagnes, R. Colombelli, P. Klang, G. Strasser, and C. Sirtori. Strong light-matter coupling in subwavelength metal-dielectric microcavities at terahertz frequencies. *Physical Review Letters*, 102(18):1–4, 2009. [37](#)
- [60] K. V. Kavokin, M. A. Kaliteevski, R. A. Abram, A. V. Kavokin, S. Sharkova, and I. A. Shelykh. Stimulated emission of terahertz radiation by exciton-polariton lasers. *Applied Physics Letters*, 97(20):2008–2011, 2010. [37](#), [38](#), [57](#)

-
- [61] O. Kyriienko, A. V. Kavokin, and I. A. Shelykh. Superradiant terahertz emission by dipolaritons. *Physical Review Letters*, 111(17):1–5, 2013. [37](#)
- [62] R. Colombelli, C. Ciuti, Y. Chassagneux, and C. Sirtori. Quantum cascade intersubband polariton light emitters. *Semiconductor Science and Technology*, 20(10):985–990, 2005. [38](#)
- [63] Markus Geiser, Fabrizio Castellano, Giacomo Scalari, Mattias Beck, Laurent Nevou, and Jérôme Faist. Ultrastrong coupling regime and plasmon polaritons in parabolic semiconductor quantum wells. *Physical Review Letters*, 108(10):1–5, 2012. [38](#)
- [64] M. Sundaram, A. C. Gossard, J. H. English, and R. M. Westervelt. Remotely-doped graded potential well structures. *Superlattices and Microstructures*, 4(6):683–691, 1988. [38](#)
- [65] R. C. Miller, A. C. Gossard, D. A. Kleinman, and O. Munteanu. Parabolic quantum wells with the GaAs-Al_xGa_{1-x}As system. *Physical Review B*, 29(6):3740–3743, 1984. [38](#)
- [66] David A. B. Miller, D. Chemla, T. Damen, A. Gossard, W. Wiegmann, T. Wood, and C. Burrus. Electric field dependence of optical absorption near the band gap of quantum-well structures. *Physical Review B*, 32(2):1043–1060, 1985. [40](#)
- [67] Alexey V. Kavokin, Jeremy J. Baumberg, Guillaume Malpuech, and Fabrice P. Laussy. *Microcavities*. Oxford University Press, 2008. [40](#)
- [68] A. V. Trifonov, S. N. Korotan, A. S. Kurdyubov, I. Ya Gerlovina, I. V. Ignatiev, Yu P. Efimov, S. A. Eliseev, V. V. Petrov, Yu K. Dolgikh, V. V. Ovsyankin, and A. V. Kavokin. Nontrivial relaxation dynamics of excitons in high-quality InGaAs/GaAs quantum wells. *Physical Review B*, 91(11):1–12, 2015. [42](#)
- [69] J. Bellessa, C. Symonds, C. Meynaud, J. C. Plenet, E. Cambril, A. Miard, L. Ferlazzo, and A. Lemaître. Exciton/plasmon polaritons in GaAs/Al_{0.93}Ga_{0.07}As heterostructures near a metallic layer. *Physical Review B*, 78(20):2–5, 2008. [42](#)
- [70] B. Sermage, S. Long, I. Abram, J. Marzin, J. Bloch, R. Planel, and V. Thierry-Mieg. Time-resolved spontaneous emission of excitons in a microcavity: Behavior of the individual exciton-photon mixed states. *Physical Review B*, 53(24):16516–16523, 1996. [42](#)

- [71] A. V. Trifonov, E. D. Cherotchenko, J. L. Carthy, I. V. Ignatiev, A. Tzimis, S. Tsintzos, Z. Hatzopoulos, P. G. Savvidis, and A. V. Kavokin. Dynamics of the energy relaxation in a parabolic quantum well laser. *Physical Review B*, 93(12):1–8, 2016. [43](#), [51](#), [55](#), [77](#), [78](#)
- [72] J. Bloch, B. Sermage, M. Perrin, P. Senellart, R. André, and Le Si Dang. Monitoring the dynamics of a coherent cavity polariton population. *Phys. Rev. B*, 71:155311, Apr 2005. [49](#)
- [73] I. G. Savenko, I. A. Shelykh, and M. A. Kaliteevski. Nonlinear terahertz emission in semiconductor microcavities. *Physical Review Letters*, 107(2):8–11, 2011. [57](#)
- [74] A. V. Kavokin, I. A. Shelykh, T. Taylor, and M. M. Glazov. Vertical cavity surface emitting terahertz laser. *Physical Review Letters*, 108(19):1–4, 2012. [57](#)
- [75] Hannah J. Joyce, Jessica L. Boland, Christopher L. Davies, Sarwat A. Baig, and Michael B. Johnston. A review of the electrical properties of semiconductor nanowires: Insights gained from terahertz conductivity spectroscopy. *Semiconductor Science and Technology*, 31(10), 2016. [57](#), [62](#), [74](#)
- [76] M Johnston and J Lloyd-Hughes. Pump-Probe Spectroscopy at Terahertz Frequencies. In *Terahertz Spectroscopy and Imaging*, pages 251–271. Springer-Verlag Berlin Heidelberg, 2013. [58](#)
- [77] VK Mag-usara, S Funker, G Niehues, EA Prieto, MH Balgos, A Somintac, E Estacio, A Salvador, K Yamamoto, M Hase, M Uneaki H Tani, MAse, and M Asahiko T Ani. Low temperature-grown GaAs carrier lifetime evaluation by double optical pump terahertz time-domain emission spectroscopy. *Optics Express*, 24(23):1465–1469, 2016. [59](#), [62](#), [65](#)
- [78] Withawat Withayachumnankul, Bernd M Fischer, and Derek Abbott. Numerical removal of water vapour effects from terahertz time-domain spectroscopy measurements. *Proceedings of the Royal Society of London A: Mathematical, Physical and Engineering Sciences*, 464(2097):2435–2456, 2008. [61](#)
- [79] Matthew C. Beard, Gordon M. Turner, and Charles A. Schmuttenmaer. Transient photoconductivity in gaas as measured by time-resolved terahertz spectroscopy. *Physical Review B*, 62:15764–15777, 2000. [62](#)

-
- [80] Withawat Withayachumnankul and Mira Naftaly. Fundamentals of measurement in terahertz time-domain spectroscopy. *Journal of Infrared, Millimeter, and Terahertz Waves*, 35(8):610–637, 2014. [64](#)
- [81] Bernd M. Fischer, Matthias Hoffmann, and Peter U. Jepsen. Dynamic range and numerical error propagation in terahertz time-domain spectroscopy. In *Optical Terahertz Science and Technology*. Optical Society of America, 2005. [64](#)
- [82] I. S. Gregory, C. M. Tey, A. G. Cullis, M. J. Evans, H. E. Beere, and I. Farrer. Two-trap model for carrier lifetime and resistivity behavior in partially annealed GaAs grown at low temperature. *Physical Review B - Condensed Matter and Materials Physics*, 73(19):1–8, 2006. [65](#)
- [83] A. Tzimis, A. V. Trifonov, G. Christmann, S. I. Tsintzos, Z. Hatzopoulos, I. V. Ignatiev, A. V. Kavokin, and P. G. Savvidis. Strong coupling and stimulated emission in single parabolic quantum well microcavity for terahertz cascade. *Applied Physics Letters*, 107(10), 2015. [77](#)
- [84] T. C.H. Liew, H. Flayac, D. Poletti, I. G. Savenko, and F. P. Laussy. Kinetic Monte Carlo approach to nonequilibrium bosonic systems. *Physical Review B*, 96(12):1–8, 2017. [77](#), [78](#)
- [85] Gaofang Li, Zuanming Jin, Xin Xue, Xian Lin, Guohong Ma, Shuhong Hu, and Ning Dai. Terahertz coherent control of surface plasmon polariton propagation in subwavelength metallic hole arrays. *Applied Physics Letters*, 100(19), 2012. [78](#)
- [86] K. B. Arnardottir and T. C. H. Liew. Terahertz cascades from nanoparticles. *Physical Review B*, 97(19):195446, may 2018. [78](#)
- [87] T. C.H. Liew, Y. G. Rubo, A. S. Sheremet, S. De Liberato, I. A. Shelykh, F. P. Laussy, and A. V. Kavokin. Quantum statistics of bosonic cascades. *New Journal of Physics*, 18(2):23041, 2016. [78](#)
- [88] Manuel Cardona. *Modulation spectroscopy of semiconductors*. Springer Berlin Heidelberg, Berlin, Heidelberg, 1970. [92](#)
- [89] Paul Harrison. *Quantum Wells, Wires and Dots*. John Wiley & Sons, Ltd, Chichester, UK, 2005. [95](#)
- [90] David Ferry. *Quantum Mechanics: An Introduction for Device Physicists and Electrical Engineers, Second Edition*. IOP Publishing Ltd, 2001. [95](#)